CHALMERS

Barge Stern Optimization

Analysis on a straight shaped stern using CFD

Master of Science Thesis in the Master Degree Programme, Naval Architecture

SOFIA ELIASSON
DANIEL OLSSON

Department of Shipping and Marine Technology
Division of Sustainable Ship Propulsion
CHALMERS UNIVERSITY OF TECHNOLOGY
Gothenburg, Sweden, 2011
Report No. X-11/266

A THESIS FOR THE DEGREE OF MASTER OF SCIENCE

Barge Stern Optimization

Analysis on a straight shaped stern using CFD

Sofia Eliasson
Daniel Olsson

CHALMERS

Department of Shipping and Marine Technology
CHALMERS UNIVERSITY OF TECHNOLOGY
Gothenburg, Sweden 2011

Barge Stern Optimization
Analysis on a straight shaped stern using CFD

SOFIA ELIASSON
DANIEL OLSSON

Report No. X-11/266

Department of Shipping and Marine Technology
Chalmers University of Technology
SE-412-96 Göteborg
Sweden

Telephone: +46(0)31 772 10 00

Cover photo: © Fartygskonstruktioner AB
Printed by Chalmers Reproservice
Gothenburgh, Sweden 2011

Barge Stern Optimization
Analysis on a straight shaped stern using CFD

SOFIA ELIASSON
DANIEL OLSSON
Department of Shipping and Marine Technology
Chalmers University of Technology

Abstract

A barge is a vessel which is designed to transport very heavy loads. Barge sterns therefore have steep inclination angles which will yield a large displacement and hence maximize the cargo capacity. In this thesis the barge stern of the split hopper barge D14 design made by Fartygskonstruktioner AB has been analysed using SHIPFLOW, a CFD software. It is of interest to investigate how the inclination angle affects the resistance of the barge. Since this analysis will focus on the stern, the flow right behind the hull is of importance. Considering that, a zonal approach was chosen for the CFD computations. This approach uses viscous flow computations (or RANS computations) to solve the wake flow at the stern.

Two different conditions of the barge have been analysed, a fully loaded condition and a ballast condition. When the barge is fully loaded there is no trim while at ballast condition there is a large trim. As a first step in the analysis computations were run on the initial hull design and the results where then verified with existing results from a resistance test made on a model of the full scale barge. When accurate results had been achieved for the initial stern the analysis continued with computations run on modified sterns where the inclination angle was systematically changed. Unfortunately the analysis could not be completed for ballast condition since a bug in SHIPFLOW was revealed and it turned out that largely trimmed conditions could not be handled by the software.

For the analysis of modified sterns, computations were run on two sterns with a steeper inclination than for the initial stern and two sterns with lesser inclination. The outcome of the computations was that in the speed interval from 9 to 12 knots the initial hull has the lowest total resistance when comparing to the modified sterns, but at speeds lower than 9 knots the steepest inclination resulted in the lowest total resistance.

Keywords: Dredger, Barge sterns, Optimization, CFD, RANS, SHIPFLOW

Preface

This thesis is the final part of our master degree program in Naval Architecture at Chalmers University of Technology. The thesis has been carried out at Fartygskontruktioner AB at their office in Gothenburg.

We would like to thank a few people which have helped us greatly in our work during the last six months. Associate Professor Rickard E. Bensow, our supervisor and examiner at Chalmers, for his great knowledge in hydrodynamics and CFD. On FKAB we would like to thank our supervisor M.Sc. Magnus Wikander and M.Sc. Stefan Johnson for background information and help throughout the thesis. At Chalmers we would like to thank Ph.D. Florian Vesting for great help in learning the CFD software and general help throughout the entire thesis. We would also like to thank Nicholas Bathfield at SSPA, Christian Veldhuis at MARIN and Lotta Olsson at Chalmers.

Göteborg, August 2011

Sofia Eliasson
Daniel Olsson

Abbreviations

AP	Aft Perpendicular
A_T	Transverse projected area
B	Breadth
C_A	Model-Ship correlation allowance
C_{AA}	Air resistance coefficient
CAD	Computer Aided Design
CAE	Computer Aided Engineering
C_B	Block coefficient
C_E	Admiralty coefficient
C_F	Specific frictional resistance coefficient
CFD	Computational Fluid Dynamics
C_M	Midship-section coefficient
C_P	Prismatic coefficient
C_{PV}	Viscous pressure resistance coefficient
C_R	Specific residual resistance coefficient
C_T	Total resistance coefficient
C_V	Specific viscous resistance coefficient
C_W	Wave resistance coefficient
C_{WTWC}	Wave resistance coefficient wave cut
CXPI	Basic model resistance coefficient in x-direction
DISV	Displacement volume moulded
F_D	Friction correction force
FKAB	Fartygskonstruktioner AB
F_n	Froude number
FP	Forward Perpendicular
g	Acceleration of gravity
GCI	Grid Convergence Index
ITTC	International Towing Tank Conference
k	Form factor
k_S	Hull roughness
L_{CB}	Longitudinal Centre of Buoyancy
L_{CG}	Longitudinal Centre of Gravity
L_M	Length of model
L_{OS}	Length overall submerged
L_{PP}	Length between perpendiculars
L_S	Length of ship
LSR	Least Square Root
L_{WL}	Length of waterline
MARIN	Maritime Research Institute Netherlands
P_E	Effective power
RANS	Reynolds Averaged Navier-Stokes
R_F	Frictional resistance
R_n	Reynolds number
R_R	Residuary resistance
R_S	Ship resistance

R_T	Total resistance
R_V	Viscous resistance
R_W	Wave resistance
S	Ship wetted area
S_{BK}	Wetted surface of bilge keels
T_A	Draught at aft perpendicular
T_F	Draught at forward perpendicular
T_M	Mean draught
V_M	Speed of model
V_S	Speed of ship
WL	Waterline
ΔC_F	Surface roughness allowance
ν	Kinematic viscosity
ρ	Mass density

TABLE OF CONTENTS

1 Introduction

1.1 Background

Barges and dredgers are vessels which are built to transport very heavy loads and they can be either self-propelled or non-propelled. For these vessels it is important to maximize the buoyancy in order to maximize the cargo capacity. By using a steep inclination angle on the stern a greater displacement can be yielded while keeping the overall dimensions, such as the length, as low as possible. Since the production cost is based on the length of the vessel it is desirable to keep the length low. Barges and dredgers are built with an as high block coefficient as possible to minimize the dimensions. On these types of vessels so called “barge sterns” are used since they are typically easy to build, they provide a big body without affecting the resistance too much and they are suitable for thrusters. Barge sterns are divided into three main shapes: straight, bent and S-shaped. Split hopper barge is a type of barge which is split longitudinally along the bottom of the hull. When offloading the cargo it carries the hull is opened in the bottom and the barge is divided into two parts. This results in a very quick offloading.

In 2007 Maritime Research Institute Netherlands (MARIN) performed a calm water model test programme and a hull form optimization program on the split hopper barge D14 design on request from Fartygskonstruktioner AB (FKAB). The D14 design is made by FKAB and it is designed to transport both dredged and other bulk material. It is self-propelled and has a hopper capacity of 2800 m^3 and deadweight of 5100 tonnes. The model test, performed by MARIN, was run in a deep water towing tank and included resistance and propulsion tests on both the fully loaded condition and the ballast condition. In the hull form optimization program the shape of the hull was optimized and a check for flow separation was made using Computational Fluid Dynamics (CFD).

1.2 Purpose

The aim of this thesis is to investigate the influence of the inclination angle on a straight barge stern using the D14 design and see how steep the inclination angle can be made and how the inclination angle affects the resistance. It will be investigated how steep the angle can be made for different velocities until the resistance loss is unacceptable. The aim is also to find an optimum angle for a given Froude number and find a relationship between the inclination angle and the resistance.

1.3 Scope

The scope of this thesis was to analyse how the resistance of a barge will change when the angle of the stern was changed. Even though it was only the stern that was modified the entire hull had to be included in the CFD computations. The hull of the split hopper barge has been analysed using SHIPFLOW. No other CFD software has been used for the analysis. During the computations the hull was free in sinkage and trim.

The only parameter that was modified on the hull was the inclination angle of the barge stern. No other dimensions have been changed and no other shapes of the stern have been analysed in this thesis. However, when the inclination angle of the stern was modified the displacement and wetted surface of the hull was changed as well.

The limitations for this thesis have been:

- Only SHIPFLOW was used for the computations in CFD.
- Only the hull of the D14 split hopper barge with a straight shaped stern was analysed.
- Only loaded and ballast condition were analysed.
- Only the inclination angle of the stern was modified.
- Computations were only run on speeds in the same speed range as in the model test.

1.4 Work Procedure

To begin with some literature on the topic was studied as well as the results from the model test performed by MARIN. Some tutorials in SHIPFLOW were done to get an understanding on how the software works.

Computations were run using an offset-file that was created based on line drawings of the existing barge hull and the results for both conditions were verified with the results from the model test. When the results received were accurate enough the angle inclination was systematically changed on the stern by modifying the offset-file. Computations were then run on the modified hulls and the results could be compared to the existing barge hull and a conclusion could be made.

2 Theory

This chapter will present the theory behind the work carried out in the project. The used software will be described and some theory behind the calculations that are done in the software. Apart from the software mentioned in the following chapters, MathWorks MATLAB® has been used for some calculations and presentation of data.

2.1 Resistance and Flow

When a ship is moving through water there will be forces opposing the motion. The total resistance, R_T, of a ship is defined as the force needed to tow the ship at a constant speed and it can be divided into subcomponents in different ways (Figure 2.1). One way is to divide it into frictional resistance, R_F, and residuary resistance, R_R, which includes all components related to the three-dimensional form of the ship and wave-making resistance. It can also be divided according to physical phenomena into viscous resistance, R_V, and wave resistance, R_W. The viscous effects are excluded from the wave resistance and it is therefore considered as an inviscid phenomenon (Larsson & Raven, 2004).

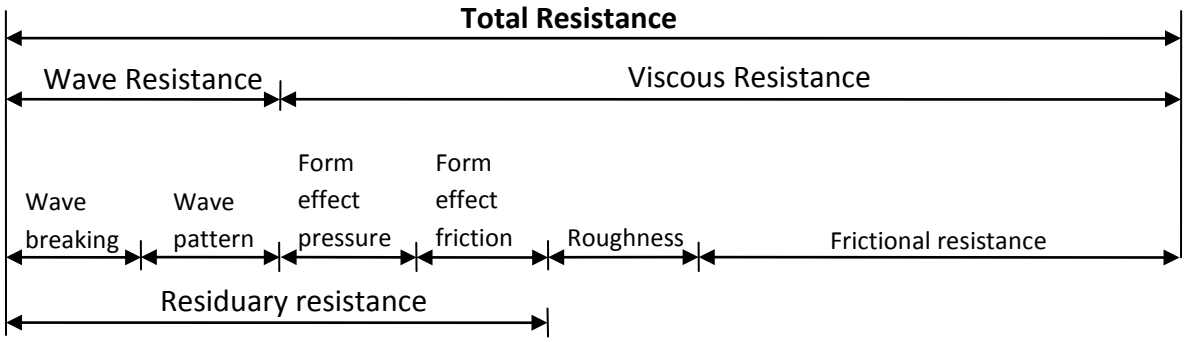

Figure 2.1: Resistance components

The relative velocity at the interface between the hull surface and the water is zero and increases with distance out from the hull surface. This is because of skin friction, which is the force due to the interaction between the hull surface and water. A boundary layer is created along the entire hull which grows downstream. The flow in the most forward part of the boundary layer is laminar, without fluctuations, and eventually the flow will get unstable and become turbulent, containing eddies (vortices) (Figure 2.2). The thickness of the boundary layer is defined as the distance from the hull surface to the point where the velocity is 99% of the undisturbed flow velocity. The rapid variation of velocity in the normal direction causes higher shear stresses in the boundary layer. The *frictional resistance*, or flat plate friction, is generated by the integral of the shear stresses over the wetted surface of the hull (Bertram, 2000).

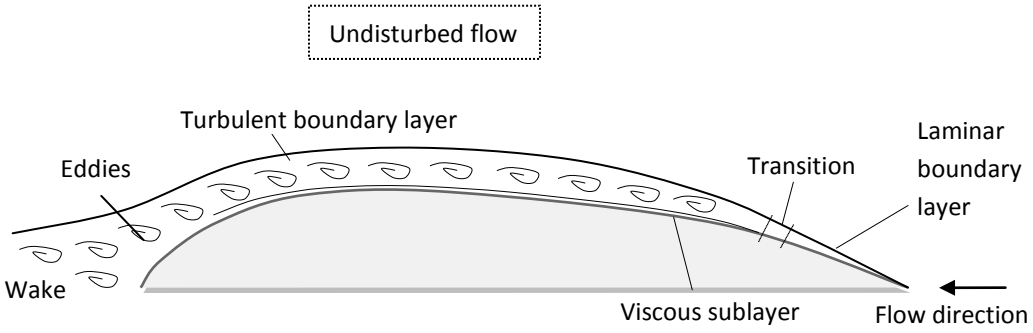

Figure 2.2: Boundary layer along the hull

If the surface *roughness* on the hull exceeds a certain limit it will affect the skin friction and cause a resistance increase (Larsson & Raven, 2004).

When moving through the water surface the ship produces a wave system. Waves are created due to water particles being removed from their equilibrium positions. If the waves become steep enough they might break down into eddies and foam. Wave breaking converts wave energy to turbulent energy and other kinetic energy contributions. The energy removed from the wave system is found in the wake of the ship and the corresponding resistance component is the *wave breaking resistance*. The remaining wave energy is contained in the generated wave pattern. It radiates out from the ship and gives rise to *wave pattern resistance* (Larsson & Raven, 2004).

As mentioned earlier there are resistance components due to the three-dimensional form of a ship. When the flow has to go around the hull the local velocity of the water just outside the boundary layer will be different from the undisturbed flow ahead of the vessel. Over the main part of the hull the velocity will increase causing an increase in friction compared to a flat plate parallel to the flow where the velocity would be almost undisturbed. This is the *form effect on friction* (Larsson & Raven, 2004).

Another form effect is due to a pressure difference between the forebody and the afterbody. In an inviscid fluid without any free surface the pressure forces acting on a hull will cancel each other exactly and the resistance will be zero, this is known as d'Alemberts paradox. In a viscous fluid the boundary layer is causing a displacement outwards of the streamlines at the stern which will reduce the high pressure at the aft end. This means that the integrated pressure forces over the hull will not cancel each other leading to the *form effect on pressure*, or viscous pressure resistance, caused by viscous forces (Larsson & Raven, 2004).

Apart from previously described resistance components there are additional components to consider such as the *wind resistance*. If the frontal area of the ship, which is facing the relative wind, is large and also if there are objects on-board that do not have an aerodynamic shape then the forces generated in strong winds may be large. Even for still air there is a small resistance component, the *air resistance* (Larsson & Raven, 2004).

2.1.1 Potential Flow

A flow that is irrotational, inviscid and incompressible is called potential flow. If irrotational flow is assumed, $\nabla \times \mathrm{V} = 0$, the components of the velocity vector are no longer independent of each other and a velocity potential ϕ exist as described by Eq. 2.1. (Larsson & Raven, 2004)

$$\nabla\phi \equiv \left(\frac{\partial\phi}{\partial x}, \frac{\partial\phi}{\partial y}, \frac{\partial\phi}{\partial z}\right) = V \equiv (u, v, w) \qquad \textbf{2.1}$$

$$\nabla \cdot \mathrm{V} \equiv \frac{\partial u}{\partial x} + \frac{\partial v}{\partial y} + \frac{\partial w}{\partial z} = 0 \qquad \textbf{2.2}$$

Equation 2.1 together with the continuity equation, Eq. 2.2, yields Laplace's equation for the potential, Eq. 2.3, which is the equation that potential flow methods are based upon. (Larsson & Raven, 2004)

$$\frac{\partial u}{\partial x} + \frac{\partial v}{\partial y} + \frac{\partial w}{\partial z} = 0 \Rightarrow \frac{\partial^2\phi}{\partial x^2} + \frac{\partial^2\phi}{\partial y^2} + \frac{\partial^2\phi}{\partial z^2} \equiv \nabla^2\phi = 0 \qquad \textbf{2.3}$$

When the flow involves a free surface, the Bernoulli equation, Eq. 2.4, provides a relation between the flow velocity, V, and the elevation of the free surface, z, according to Eq. 2.5. (White, 2008)

$$\frac{\partial\phi}{\partial t} + \frac{p}{\rho} + \frac{1}{2}\mathrm{V}^2 + gz = constant \qquad \textbf{2.4}$$

$$\mathrm{V}^2 = |\nabla\phi|^2 = constant - 2gz \qquad \textbf{2.5}$$

One advantage with potential flow methods compared to methods based on Navier-Stokes equations, Eq. 2.6, is that Laplace's equation is linear. Elementary solutions of the equation may thus be added together to complex solutions. Complex flows can be solved by using a large number of simple solutions called singularities that together yields a solution for the flow. The singularities may be sources (inflow of fluid), sinks (outflow of fluid) dipoles or vortices.

The potential flow is solved with a panel method. The surface of the ship and the water surface are divided into flat, ideally square, panels commonly with a constant source strength (referred to as meshing). This means that the only unknown parameter for each panel is the source strength. An equation corresponding to the boundary condition is applied to one point on each panel, the collocation point, which gives N points with N equations and N unknown source strengths. From this system of equations it is then possible to calculate the velocity at every point in the flow and get the potential flow around the hull.

Potential flow methods can be either linear or nonlinear for the free surface. Linear methods apply the boundary conditions on an undisturbed free surface and the nonlinear terms for the unknowns are dismissed. For nonlinear methods the boundary conditions are applied to a free surface with waves using waves generated from the previous solution in the next iteration. Nonlinear methods are considered more accurate but are also more time consuming.

Since potential flow is an irrotational flow and viscosity is neglected some disadvantages follow. In regions with high vorticity, for example wakes and boundary layers, potential flow methods will not give reasonable results. Unfortunately this also means that the solution provided by potential flow methods is erroneous even outside the boundary layer. This error is usually small for the forebody and middle section but can be significant for the stern flow where viscous effects strongly influence the flow. This results in that the calculated wave heights and pressures will be too large. (Larsson & Raven, 2004), (White, 2008) and (Bertram, 2000)

2.1.2 Viscous Flow, RANS

The Navier-Stokes equations, Eq. 2.6 together with the continuity equation, Eq. 2.2, would be enough to solve all flow physics for ship flows. Unfortunately it requires immense computational power. That is why a number of methods exist today that deal with simplifications of the Navier-Stokes equations. (Larsson & Raven, 2004)

$$\begin{cases} \frac{\partial u}{\partial t} + u\frac{\partial u}{\partial x} + v\frac{\partial u}{\partial y} + w\frac{\partial u}{\partial z} = -\frac{1}{\rho}\frac{\partial p}{\partial x} + \nu\left(\frac{\partial^2 u}{\partial x^2} + \frac{\partial^2 u}{\partial y^2} + \frac{\partial^2 u}{\partial z^2}\right) \\ \frac{\partial v}{\partial t} + u\frac{\partial v}{\partial x} + v\frac{\partial v}{\partial y} + w\frac{\partial v}{\partial z} = -\frac{1}{\rho}\frac{\partial p}{\partial y} + \nu\left(\frac{\partial^2 v}{\partial x^2} + \frac{\partial^2 v}{\partial y^2} + \frac{\partial^2 v}{\partial z^2}\right) \\ \frac{\partial w}{\partial t} + u\frac{\partial w}{\partial x} + v\frac{\partial w}{\partial y} + w\frac{\partial w}{\partial z} = -\frac{1}{\rho}\frac{\partial p}{\partial z} - g + \nu\left(\frac{\partial^2 w}{\partial x^2} + \frac{\partial^2 w}{\partial y^2} + \frac{\partial^2 w}{\partial z^2}\right) \end{cases} \quad \textbf{2.6}$$

By dividing the velocities and pressure into a time average and a fluctuating part it is possible to bring the Navier-Stokes equations into a form which is possible to solve numerically with the computational power of today. This time averaged method is called Reynolds Averaged Navier-Stokes, RANS, and is the viscous method used in this thesis, Eq. 2.7. The time averaged velocities is denoted according to $u_i = \overline{u_i} + u_i'$ where $\overline{u_i}$ is the average and u_i' the fluctuating component in the x-, y- and z-direction. Time averaging Navier-Stokes equations eliminate the turbulent fluctuations in all terms except the Reynolds stresses, $-\rho\overline{u_i'u_j'}$, see the last terms in Eq. 2.7. The Reynold stresses introduce six additional unknowns into the equation system consisting off four equations. This is solved by using a turbulence model together with RANS to couple the Reynold stresses with the average velocities. (Flowtech Int., 2010) and (Bertram, 2000)

$$\begin{cases} \rho\left(\frac{\partial u}{\partial t} + u\frac{\partial u}{\partial x} + v\frac{\partial u}{\partial y} + w\frac{\partial u}{\partial z}\right) = -\frac{\partial p}{\partial x} + \mu\left(\frac{\partial^2 u}{\partial x^2} + \frac{\partial^2 u}{\partial y^2} + \frac{\partial^2 u}{\partial z^2}\right) - \rho\left(\frac{\partial \overline{u'^2}}{\partial x} + \frac{\partial \overline{v'u'}}{\partial y} + \frac{\partial \overline{w'u'}}{\partial z}\right) \\ \rho\left(\frac{\partial v}{\partial t} + u\frac{\partial v}{\partial x} + v\frac{\partial v}{\partial y} + w\frac{\partial v}{\partial z}\right) = -\frac{\partial p}{\partial y} + \mu\left(\frac{\partial^2 v}{\partial x^2} + \frac{\partial^2 v}{\partial y^2} + \frac{\partial^2 v}{\partial z^2}\right) - \rho\left(\frac{\partial \overline{u'v'}}{\partial x} + \frac{\partial \overline{v'^2}}{\partial y} + \frac{\partial \overline{w'v'}}{\partial z}\right) \\ \rho\left(\frac{\partial w}{\partial t} + u\frac{\partial w}{\partial x} + v\frac{\partial w}{\partial y} + w\frac{\partial w}{\partial z}\right) = -\frac{\partial p}{\partial z} - \rho g + \mu\left(\frac{\partial^2 w}{\partial x^2} + \frac{\partial^2 w}{\partial y^2} + \frac{\partial^2 w}{\partial z^2}\right) - \rho\left(\frac{\partial \overline{u'w'}}{\partial x} + \frac{\partial \overline{v'w'}}{\partial y} + \frac{\partial \overline{w'^2}}{\partial z}\right) \end{cases}$$

2.7

The RANS solver uses a finite volume method where the computational domain is divided into a number of cells. Governing equations are integrated over each cell before the investigated variable is approximated with a value at the centroid of each cell. The finite volume method ensures that the quantity of variables such as mass, momentum and energy is conserved since errors at the cell faces cancel with the errors of neighboring cells.

2.2 SHIPFLOW CFD Software

The CFD software used for the investigation in this thesis is called SHIPFLOW which is a powerful suite of CFD tools by FLOWTECH International AB. The software can be used for both global and zonal approach, both of which are described more in chapter 2.2.6.

SHIPFLOW is built up from a number of modules each briefly described in chapters 2.2.1 to 2.2.5 below. (Flowtech Int., 2010)

2.2.1 XMESH

XMESH is the mesh generator that creates panels for the hull and free surface for the potential flow solver, XPAN. This module can be run as a separate program to check the panel distribution before the time consuming calculations are made. If non-linear calculations are made XMESH will be called upon during the potential flow calculations to update the mesh between each iteration. XMESH is also executed when sinkage and trim is considered.

2.2.2 XPAN

XPAN is the potential flow solver. It solves the potential flow around three dimensional bodies based on a panel method and using the mesh generated by XMESH. XPAN can solve the potential flow using either linear or non-linear free surface boundary conditions. Some of the features that it is possible to compute using XPAN is the wave resistance, wave pattern, pressure contours and sinkage/trim. The result from XPAN is stored in a database file required to execute XBOUND.

2.2.3 XBOUND

XBOUND is the module that deals with the thin turbulent boundary layer but is also capable of computing the laminar boundary layer. The calculations are solved along streamlines traced from the potential flow calculation. For simple cases with a clearly defined stagnation point, which is a point in the flow where the local velocity is zero, it is possible to compute the transition to the turbulent boundary layer. XBOUND creates a database file required to execute XCHAP.

2.2.4 XGRID

XGRID creates the grid used for viscous computations in XCHAP. With XGRID it is possible to create grids for ship or submarine hulls and the module is capable of handling twin skeg hulls and bulbous bows. Appendages however are not possible to handle with XGRID.

2.2.5 XCHAP

XCHAP is a module that solves Reynolds Averaged Navier-Stokes equations using one of several available turbulence models (EASM, k-ω BSL, k-ω SST). With XCHAP it is possible to use overlapping grids and the module can be used for both zonal and global approaches. XCHAP uses the grid generated by XGRID but it is also possible to import grids created by other software. By using this solver it is possible to get the time-averaged velocity, pressure and turbulent quantities. The total resistance can be computed by combining the results from XPAN, XBOUND and XCHAP.

2.2.6 Global and Zonal Approach

There are two different approaches available when using RANS in SHIPFLOW; Global and Zonal. With RANS it is possible to predict all quantities if a free surface is included. However, RANS is very time consuming and SHIPFLOW treats the free surface as a symmetry plane which limits what quantities can be calculated. By using a global approach RANS equations are applied to the entire computational domain. The drawback of using a global approach is the increase in computational time. Using zonal approach utilize the fact that potential flow computations are accurate enough for the forebody flow. The stern flow is solved with a RANS method and the transition is solved with a boundary layer method, see Figure 2.3. The potential flow computation is done for the entire computational domain in order to include the wave resistance which SHIPFLOW is unable to solve with RANS.

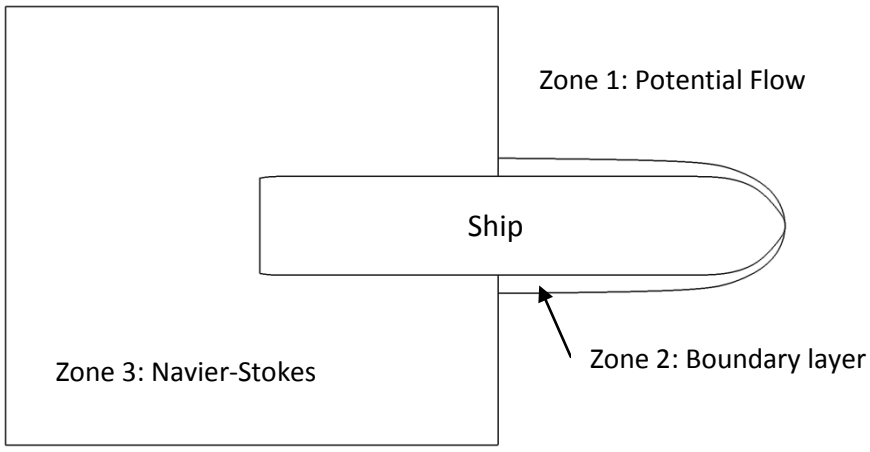

Figure 2.3: Zonal approach

2.2.7 Offset creation

Offset files are the hull geometry files that SHIPFLOW uses to generate a mesh. The offset files consist of groups of stations with points representing the geometry of the vessel. Normally the offset file contains separate offset groups for the bulb, stern, stern bulb/skeg and stern overhang depending on the geometry of the vessel.

2.3 FRIENDSHIP-Framework

FRIENDSHIP-Framework is a CAE (Computer Aided Engineering) software with integrated CAD (Computer Aided Design) functionality. The software is used as a platform to combine CAD and CFD functionality for optimization purposes and is also used as a framework for various commercially available CFD solvers. (Framework, 2011)

In this thesis FRIENDSHIP-Framework is used as a graphical user interface for SHIPFLOW as well as a CAD tool to create the geometry files from 3D drawings of the investigated vessel. This is done because SHIPFLOW only supports a specific format of geometry input, referred to as offsets.

2.4 Resistance Test

A resistance test is a model test which is carried out to provide data from which the resistance of a model is determined at certain speeds which is then converted to full scale values (ITTC, 2008).

For a resistance test there should be geometric similarity between the full scale ship and the model. Being geometrically similar means having the same shape. There are two other types of similarity; kinematic and dynamic. Kinematic similarity means that the streamlines around the hull are geometrically similar and dynamic similarity means that the force vectors are scaled by the same factor and will have the same direction at model and full scale. During a resistance test these similarities should be fulfilled as well, but it is not possible. There are some non-dimensional parameters which characterize the flow and the forces. These are obtained after introducing non-dimensional quantities into the governing equations and their boundary conditions. If kinematic and dynamic similarity is to be achieved between model and full scale then all non-dimensional parameters would have to be kept equal between the scales and this is not possible. The main non-dimensional parameters in the flow around the hull are the Froude number, F_n, (Eq. 2.8) and the Reynolds number, R_n, (Eq. 2.9) (Larsson & Raven, 2004),

$$F_n = \frac{V}{\sqrt{gL}} \qquad \textbf{2.8}$$

$$R_n = \frac{VL}{\nu} \qquad \textbf{2.9}$$

where,

V = speed, in m/s
L = length of waterline, in m
g = acceleration of gravity, in m/s^2
v = kinematic viscosity of tank water or sea water, in m^2/s

The physical properties g and v are assumed constant. For a constant Froude number the speed of the model will then be (Eq. 2.10):

$$V_m = V_s \sqrt{\frac{L_m}{L_s}} \qquad \textbf{2.10}$$

Index m stands for model and index s stands for full scale.

Since the length of the ship, L_s, is significantly larger than the length of the model, L_m it means that the speed of the model, V_m, will have to be much lower than the speed of the ship, V_s. For a constant Reynolds number it will instead have to be much higher (Eq. 2.11):

$$V_m = V_s \frac{L_s}{L_m} \qquad \textbf{2.11}$$

Since it is impossible to keep the model speed higher and lower than the ship speed at the same time it is impossible to keep the non-dimensional parameters equal between the scales and that is the reason why dynamic and kinematic similarity is not possible (Larsson & Raven, 2004).

When running a resistance test this problem is solved by performing the resistance test at equal Froude number and then correct for the errors introduced by the incorrect Reynolds number (Larsson & Raven, 2004).

A resistance test is often run in a towing tank where the model is towed by a carriage and the following quantities are measured:

- Model speed
- Towing force
- Rise/sinkage fore and aft
- Water temperature

Observations of the wave patterns are also made during the test(Larsson & Raven, 2004).

When performing a resistance test it is important that the flow over the model is fully turbulent since this is the case for a full-scale ship. To create a turbulent flow the laminar flow is disturbed by for example trip-wires placed around the hull at a station 5 percent of the forward perpendicular (Larsson & Raven, 2004).

The measured towing force is used to determine the total resistance of the model and the measured water temperature is used for calculation of viscosity and density of the water (ITTC, 2008).

Several runs are performed and the measured values are recorded continuously throughout the test and are then presented as mean values (ITTC, 2008).

When the total resistance of the model has been obtained it is converted from model scale to full scale which further will give the total effective power, P_E, needed to drive the full scale ship through the water without propulsive losses. There are two methods that are mainly used for this extrapolation from model to full scale: Froude's method and the 1978 ITTC-method. The latter method is the most common method and will be further explained in the next section (Larsson & Raven, 2004).

2.4.1 1978 ITTC Performance Prediction Method

ITTC is short for International Towing Tank Conference which is a voluntary association responsible for, as described on their webpage, "the prediction of hydrodynamic performance of ships and marine installations based on the results of physical and numerical modelling." (ITTC, 2011). The procedure of their 1978 Extrapolation Method is described next.

Force coefficients are non-dimensional values of the total resistance and its subcomponents. They are defined by dividing the resistance by the dynamic head, $\frac{1}{2}\rho V^2$, times the wetted surface area, S (Larsson & Raven, 2004). The first step in the ITTC-78 extrapolation method is to calculate the total resistance coefficient, C_T, for the model using the resulted R_T from the resistance test (Eq. 2.12) (SSPA, 2009).

$$C_{Tm} = \frac{R_{Tm}}{\frac{1}{2}\rho_m V_m^2 S_m} \qquad \textbf{2.12}$$

where,

R_{Tm} = total resistance, in N
ρ_m = mass density of tank water, in Ns^2/m^4
V_m = speed, in m/s
S_m = wetted surface, in m^2

The speed of the model is calculated keeping the Froude number constant between the scales (Eq. 2.10).

The frictional resistance coefficient, C_F, is calculated from the ITTC-57 model-ship correlation line which gives the relation between C_F and the Reynolds number (Eq. 2.9) according to Eq. 2.13, also referred to as the ITTC-57 formula (SSPA, 2009):

$$C_F = \frac{0.075}{(log_{10}R_n - 2)^2} \qquad \textbf{2.13}$$

The frictional resistance coefficient is calculated for a flat plate, it does not account for the effect of the three-dimensional hull form. The next step is therefore to determine a form factor, 1 + *k*, which corrects for the three-dimensional effects. The form factor represents the ratio of the viscous to the frictional resistance. It is determined from resistance measurements at low speed, where the wave resistance is negligible, and is verified with statistical data. (Veldhuis & Pouw, 2008).

The residuary resistance coefficient, C_R, can now be computed which at the same Froude number can be assumed to be the same for both model and full scale (Eq. 2.14).

$$C_{Rm} = C_{Tm} - (1 + k)C_{Fm} = C_{Rs} \quad \textbf{2.14}$$

The surface roughness allowance, ΔC_F, is assumed to be (Eq. 2.15):

$$\Delta C_F = [105(\frac{k_s}{L})^{1/3} - 0.64]10^{-3} \quad \textbf{2.15}$$

Where the standard value of hull roughness k_s = 150 µm can be used.

The air resistance coefficient, C_{AA}, is assumed to be (Eq 2.16):

$$C_{AA} = 0.001\frac{A_T}{S_s} \quad \textbf{2.16}$$

where,

A_T = transverse projected area above the water of the ship including superstructures, in m^2.

The total resistance coefficient of the ship can now be computed (Eq. 2.17):

$$C_{TS} = \frac{S_s + S_{BK}}{S_s}[(1 + k)C_{FS} + \Delta C_F] + C_{RS} + C_{AA} \quad \textbf{2.17}$$

where,

S_m and S_s = wetted surface, in m^2
S_{BK} = wetted surface of bilge keels, in m^2

The total ship resistance is calculated from Eq. 2.18:

$$R_{TS} = C_{TS}\frac{1}{2}\rho_s(0.5144V_s)^2 S_s 10^{-3} \quad \textbf{2.18}$$

where,

ρ_s = mass density of sea water, in Ns^2/m^4
S_s = wetted surface, in m^2

Finally, the full scale ship's effective power is calculated in megawatt [MW] according to Eq. 2.19 (SSPA, 2009):

$$P_E = 0.5144 V_s R_{TS} 10^{-3} \quad \textbf{2.19}$$

2.4.2 MARIN Form Factor Method

The method used at MARIN for the extrapolation of model test results, MARIN Form Factor Method, is based on the form factor concept and it follows Froude's hypothesis and similarity law. According to Froude's hypothesis the resistance can be divided into two independent components, the viscous component being proportional to the frictional resistance of a flat plate of the same length and wetted surface area when towed at the same speed and the wave-making resistance, R_W, which follows Froude's similarity law (Eq. 2.20) (Veldhuis & Pouw, 2008):

$$R_{Ws} = R_{Wm}\lambda^3 \frac{\rho_s}{\rho_m} \quad \textbf{2.20}$$

provided (Eq. 2.21):

$$V_s = V_m\sqrt{\lambda} \quad \textbf{2.21}$$

The flat plate resistance, R_F, is determined by Eq. 2.22:

$$R_F = ½\rho V^2 S C_F \quad \textbf{2.22}$$

The frictional resistance coefficient is determined by either the ITTC-57 formula (Eq. 2.13) or Schoenerr's meanline (Eq. 2.23 and Figure 2.4):

$$\frac{0.242}{\sqrt{C_F}} = \log(R_n C_F) \quad \textbf{2.23}$$

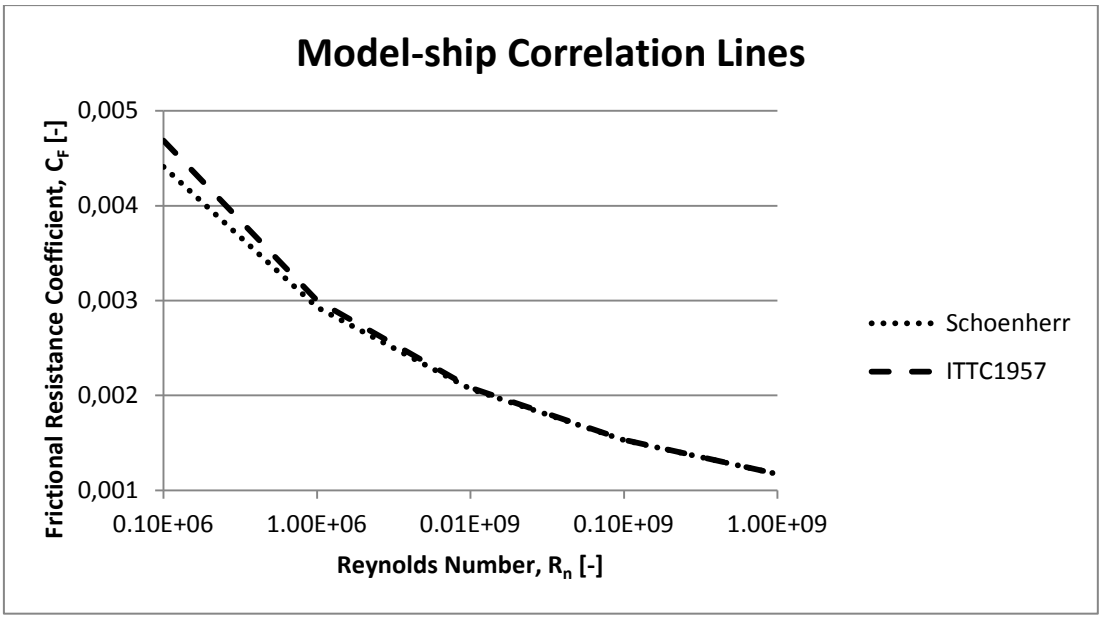

Figure 2.4: Shoenerr's meanline and ITTC-1957 line

The resistance is then scaled according to Eq. 2.24:

$$R_s = \left(R_m - R_{Fm}(1+k)\right)\lambda^3 \frac{\rho_s}{\rho_m} + R_{Fs}(1+k) + R_{allowance} = (R_m - F_D)\lambda^3 \frac{\rho_s}{\rho_m}$$

2.24

The scale effect on the resistance of the hull and appendages, F_D, also called the friction correction force or the resistance unloading force is determined either from Eq. 2.25 or 2.26:

$$F_D = 0.5\rho_m V_m^2 S_m (1+k)(C_{Fm} - C_{Fs}) - \frac{\rho_m}{\rho_s} R_{allowance}/\lambda^3$$

2.25

$$F_D = 0.5\rho_m V_m^2 S_m \left((1+k)(C_{Fm} - C_{Fs}) - C_A\right) \qquad \textbf{2.26}$$

and $R_{allowance}$ is the resistance component to allow for hull roughness, appendages on the ship but not included on the model, still air drag of the ship or any other additional resistance component acting on the ship but not on the model (Veldhuis & Pouw, 2008).

The effective power is then defined as Eq. 2.27 (Veldhuis & Pouw, 2008):

$$P_E = R_s V_s \qquad \textbf{2.27}$$

This method is quite similar to the ITTC 1978 method but there are some differences. In the ITTC method the flat plate frictional resistance coefficient is determined by the ITTC-57 equation. In the MARIN method it is either decided by the ITTC-57 equation or by Schoenerr's meanline. If the latter is chosen then there will be differences in C_F between the two methods. The values in Shoenherr's meanline are slightly lower at

lower Reynolds numbers. Another difference is that the ITTC-78 method includes both an air resistance coefficient and a surface roughness allowance. In the MARIN method, if the friction correction force, F_D, is calculated by using Equation 2.26 then the hull roughness will not be included since C_A only includes the effect of the still-air drag. In that case there will be differences in the final results.

2.5 Uncertainty estimation

The used method for grid convergence study is based on the Grid Convergence Index, GCI, suggested by Roache (Roache, 1998). Roache suggested GCI to provide a consistent way of reporting grid convergence studies and GCI is stated as an error percentage within which a converged solution is likely to be found.

To perform an uncertainty analysis several different grids are set up and computed. The error e of a numerical solution is calculated according to Eq. 2.28. This error is often denoted as δ_{RE} and is an important part in determining the uncertainty of a solution.

$$e_{\phi_i} = \delta_{RE} = \phi_i - \phi_0 = \alpha h_i^p \qquad \textbf{2.28}$$

Where ϕ_i is the computed numerically solution of a scalar variable, ϕ_0 is the estimated true solution (at zero grid size), α is a constant, h_i represent the cell size and p is the order of accuracy. The subscript $i = [1 : ng\ ]$ stands for any given grid and ng is the total number of grids on which the estimation is done.(Zou, Larsson, & Orych, 2010)

At least three different grids need to be examined to be able to solve the unknowns (ϕ_0, α, p) in Eq. 2.28. If more than 3 grids are available for the estimation then the Least Square Root, LSR, method can be used to find the unknowns by minimizing Eq. 2.29. By evaluating more grids than required using the LSR method it is possible to reduce the influence from the scatter in the solutions.

$$S(\phi_0, \alpha, p) = \sqrt{\sum_{i=1}^{ng} \left(\phi_i - \left(\phi_0 + \alpha h_i^p\right)\right)^2} \qquad \textbf{2.29}$$

The standard deviation U_s of the result from Eq. 2.29 is obtained by Eq. 2.30.

$$U_s = \frac{\sqrt{\sum_{i=1}^{ng} \left(\phi_i - \left(\phi_0 + \alpha h_i^p\right)\right)^2}}{ng - 3} \qquad \textbf{2.30}$$

The grid size variable h_i is calculated according to Eq. 2.31. The examined grids are ordered from finest to coarsest which means that the grid which contains most cells will have a h_i value of one.

$$\frac{h_i}{h_1} = \sqrt[3]{\frac{(Number\ of\ cells)_1}{(Number\ of\ cells)_i}} \qquad \textbf{2.31}$$

To be able to use the LSR method with acceptable accuracy the iterative error for the computations should be negligible to the discretization error, Eq. 2.28. The iterative error should preferable be two to three orders of magnitudes smaller than the discretization error. The iterative error of a computation can be estimated by taking the standard deviation of the last 1000 iterations. When these variables have been computed it is possible to estimate the uncertainty of a solution U_ϕ according to the following criteria. (Eça & Hoekstra, 2006)

A. If Monotonic convergence (p > 0) is observed:

1) For $0.95 \leq p < 2.05$
   $U_\phi = 1.25\delta_{RE} + U_s$

2) For $0 < p < 0.95$
   $U_\phi = \min(1.25\delta_{RE} + U_s, 1.25\Delta_M)$
   Where Δ_M is defined as the maximum difference between all the solutions:
   $\Delta_M = \max(|\phi_i - \phi_j|) \qquad 1 \leq i \leq n_g, 1 \leq j \leq n_g$

3) For $p \geq 2.05$
   $U_\phi = \max(1.25\delta^*_{RE} + U_s, 1.25\Delta_M)$
   Where δ^*_{RE} is obtained from the Least Squares Root method given $p = 2$:
   $\delta^*_{RE} = \phi_i - \phi_0 = \alpha h_i^2$

B. If Monotonic convergence is not observed $(p < 0)$:
   $U_\phi = 3\Delta_M$

3 Method

A literature study on the flow and resistance of a ship and CFD cases that deal with similar examinations has been performed. Tutorials in SHIPFLOW were made to get to know the software better in advance of the investigation. Useful information has been collected from previous course materials and also from searching the internet and the library at Chalmers. Further information and answers regarding the investigation has been provided in correspondence with engineers at Chalmers, SSPA, MARIN and FlowTech.

Existing results from model tests in towing tanks for the investigated vessel has been studied of which all results have been provided by the company, FKAB.

The analysis of the after body has been made mainly by CFD-calculations using SHIPFLOW. A reference CFD-offset model was created based on line drawings received from FKAB. This model was first evaluated using double model computations and grid uncertainty analysis to evaluate the reliability. Computations were then made on the reference hull shape. Loaded and unloaded condition were analyzed for a range of different Froude numbers and compared to model test results.

After the analysis of the reference hull had been made the shape of the after body was changed. The afterbody of the reference hull is slightly curved so a mean angle for the inclination was defined for the hull. Four different CFD offsets were developed for investigation, two with less and two with larger inclination. Computations for these new models were made using the same loading conditions and Froude numbers as for the analysis of the reference hull. The results were then compared with the results for the reference hull.

All results were continuously recorded in this final report and were presented at an oral presentation by the end of the project.

4 Test Case

In 2007 MARIN performed a calm water model test programme and a hull form optimization programme on the split hopper barge D14 design, on request from FKAB. The model test programme was performed in a deep water towing tank following the procedure described in chapter 2.4. The hull form optimization programme was performed using CFD softwares, RAPID and PARNASSOS.

4.1 Description of barge

The FKAB D14 design split hopper barge is a self-propelled unit with a hopper capacity of 2800m^3. The barge is propelled by two thrusters and has and deadweight of 5100 tonnes. The hull has a split longitudinally along the keel which is opened when offloading cargo. Figure 4.1 shows a photo of the bulb seen from above, taken on-board the split hopper barge. In the photo the split in the middle of the bulb is seen which continues along the entire hull.

Figure 4.1: The bulb seen from above

There are two conditions being analysed; loaded and ballast condition. For the loaded condition the barge is at even keel and for the ballast condition the barge will be trimmed. The ship particulars are presented in Table 4.1.

	Loaded condition	Ballast condition
Length between perpendiculars, L_{PP}	88.45 m	88.45 m
Length on waterline, L_{WL}	92.105 m	89.511 m
Length overall submerged, L_{OS}	94.91 m	89.51 m
Breadth molded on waterline (WL), B	18.00 m	18.00 m
Draught molded on FP, T_F	4.8 m	0.7 m
Draught molded on AP, T_A	4.8 m	2.6 m
Displacement volume molded, ∇	6809.1 m^3	2165.6 m^3
Displacement mass in seawater, Δ_1	6979.3 t	2219.7 t
Wetted surface area bare hull, S	2326.7 m^2	1649.3 m^2
Longitudinal centre of buoyancy (LCB) position aft of FP, L_{CB}	48.96 m	46.91 m
Block coefficient, C_B	0.891	0.824
Midship section coefficient, C_M	0.996	0.988
Prismatic coefficient, C_P	0.895	0.834
Breadth-Draught ratio, B/T	3.750	10.909

Table 4.1: Ship particulars for loaded and ballast condition (Veldhuis & Pouw, 2008)

4.2 MARIN CFD Optimization

Before the model test programme was run a CFD hull form optimization was carried out. Potential flow computations were made to optimize the initial hull lines which were then checked for flow separations with viscous flow calculations. During the hull form optimization the displacement was fixed and the longitudinal centre of gravity, LCG, could be moved slightly forward. The hull lines were optimized for a speed of 10 knots and a water depth of 15 meters for the loaded condition. The hull form was then checked at ballast condition for possible flow problems (Veldhuis & Pouw, 2008).

RAPID is a CFD-software which calculates the steady inviscid flow around a ship hull, the wave pattern and the wave resistance. Its primary purpose is the minimization of wave-making and wave resistance. A first analysis of the results indicates how to modify the hull form to reduce the wave making. RAPID is then used again to verify the new hull lines (Veldhuis & Pouw, 2008).

PARNASSOS is a CFD-software which calculates the steady incompressible viscous flow around a ship hull. Information on the velocity and pressure field around the hull, the wake field in the propeller plane, the possible occurrence of flow separation and the viscous resistance can be received. The hull form can then be optimized for viscous resistance or propeller inflow for both model and full scale (Veldhuis & Pouw, 2008).

The hull lines were optimized by moving the fore shoulder aft, smoothen the waterlines and transitions of the section into the bottom. To compensate for displacement losses the bulb was slightly increased below the waterline. The outcome was a significantly decreased wave pattern and a smoother pressure distribution on the hull. Also no flow separations were shown on either model or full scale (Veldhuis & Pouw, 2008).

RAPID and PARNASSOS can be compared to XPAN and XCHAP in SHIPFLOW. Both RAPID and XPAN are potential flow solvers and PARNASSOS and XCHAP are RANS-solvers calculating the viscous flow. The main difference between these softwares is how the boundary layer is solved. In SHIPFLOW there is XBOUND which computes the boundary layer using inputs from XPAN and then creates a database file required to execute XCHAP. In RAPID there is no boundary layer assumption. PARNASSOS resolves the boundary layer without using wall functions by creating a small cell near the hull (Veldhuis C. , E-mail, 2011).

4.3 MARIN Towing Tank Tests

The full scale barge has a speed range of 7-12 knots for the loaded condition and 8-12 knots for the ballast condition. The speeds that the model was to be run at during the test were decided according to Eq. 2.10. The model that was used had a linear scale ratio of 11.062. Stock propeller models were first selected for the tests and then the scale ratio was chosen according to the size of the propellers. A photo of the model use in the model test is shown in Figure 4.2. As can be seen in the photo, the split was included in the model.

Figure 4.2: Model seen from the front

The model was towed by a carriage in tank water with a temperature of 13.7°C and the total longitudinal force acting on the model was measured for respective speed in the speed range. Turbulence of the flow over the hull was induced by studs near the bow. When running the test the model was free to heave, which is the vertical motion of a ship, and pitch, which is the motion of a ship about the transverse axis.
The Froude and Reynolds numbers were based on the length overall submerged, L_{OS}, and the frictional resistance R_F, is determined according to the ITTC-57 formula (Eq.2.11). The results received from the model test, presented in Appendix A, were used to verify the results from the CFD computations described in chapter 5.5.

5 Verification

5.1 Offset creation

An offset file for the reference hull was created using FRIENDSHIP-Framework. To ensure good geometry representations in the CFD software the hull was split into five groups, one group each for the bulb, hull, stern, skeg and one for the flat area under the skeg. The reason why the skeg was split into two groups was to ensure a good geometry representation of the mesh and to prevent SHIPFLOW XMESH from rounding the transition between the side of the skeg and the bottom.

5.2 Double Model Calculation

Double model calculation is a good way of evaluating the discretization error introduced by the hull in a panel method. It is based upon d'Alemberts paradox that the resistance should be zero for a hull where waves are not treated in the calculation. The calculated resistance for a hull without a free surface can thus be treated as the discretization error. This resistance can be used as a correction factor when using linear potential flow methods but this is not the case for non-linear methods. Since non-linear methods will be used, calculating and comparing the hull resistance will only be used as an indication on how good the mesh is and a base for the selection of meshes. Even though the resistance cannot be used as a correction factor, it is preferable to have a double model resistance of at least one order of magnitude lower than the wave resistance. (Larsson & Raven, 2004)

Double model calculations have been performed both for the ballast condition and the loaded, zero-trim, condition. One way of keeping the number of nodes down while maintaining sufficiently small panels is by utilizing stretch functions. SHIPFLOW supports 5 types of stretching modes in addition to uniform spacing. The stretching modes are described in Table 5.1 below.(Flowtech Int., 2010)

Mode	Description	Mesh
0	Uniform Distribution	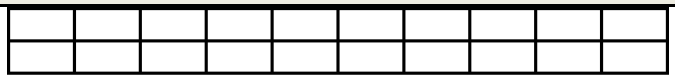
1	Hyperbolic tangent	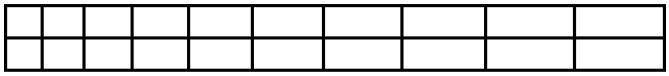
2	Exponential	
3	Hyperbolic sine	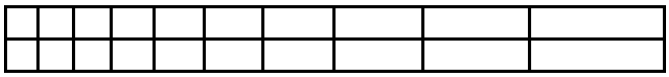
4	Geometric	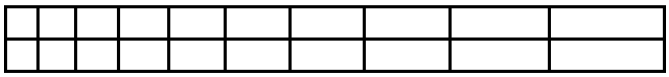
5	Hyperbolic tangent (Specified at two ends)	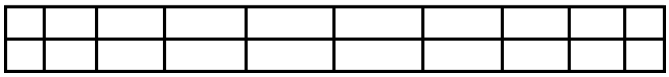

Table 5.1: SHIPFLOW mesh stretch modes

5.2.1 Trimmed, ballast condition

When the hull mesh was created the settings were to begin with randomly chosen. The number of stations and points and the extent of stretching were then varied to get a hull mesh suitable for this case. Double model computations were run on four different hull meshes in ballast condition to be evaluated (Figure 5.1-Figure 5.4). The settings for the different meshes are presented in Appendix B. During the evaluation each mesh was refined two or three times by multiplying the number of points and stations with a refinement factor of $\sqrt{2}$.

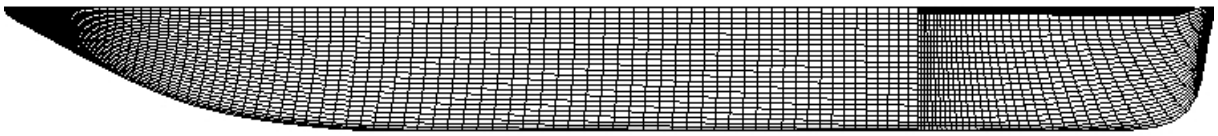

Figure 5.1: Mesh 1 seen from below

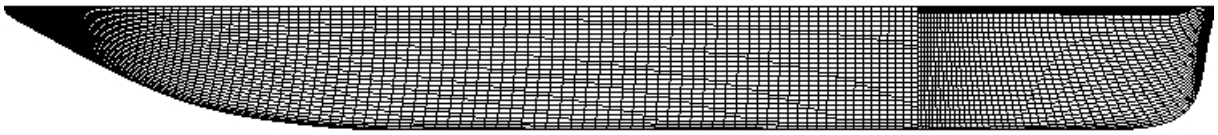

Figure 5.2: Mesh 2 seen from below

Figure 5.3: Mesh 3 seen from below

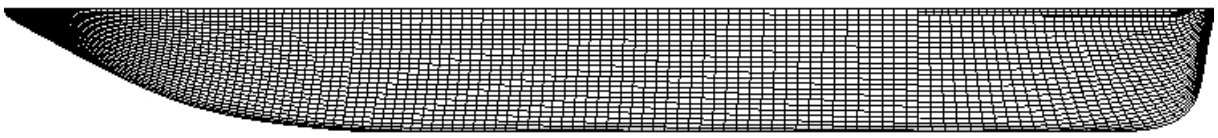

Figure 5.4: Mesh 4 seen from below

There are some rules of thumb to follow for the grid settings. One of the rules is that the panels on the hull mesh should be as square as possible (Bathfield, E-mail, 2011). If looking at the hull meshes in the figures above Mesh 4 consists of the most squared panels and it has a stretching mode which makes a smooth transition between the different hull groups. For example, in contrast to Mesh 4, it is clearly seen in the first three meshes where the division between the hull and stern group is. Because of this Mesh 4 is assumed to be the most suitable hull mesh.

Since each mesh has been refined two or three times in the double model computations there will be three of four different settings for each mesh where the number of panels have been systematically doubled for each setting. Table 5.2 shows the refinement factor and the number of panels for each mesh and their different settings.

		Number of Panels			
Setting no.	**Refinement factor**	**Mesh 1**	**Mesh 2**	**Mesh 3**	**Mesh 4**
1	1	3 786	5 661	5 971	4 577
2	$\sqrt{2}$	7 766	11 426	12 086	9 340
3	$\sqrt{2}^2$	15 719	23 365	24 625	18 949
4	$\sqrt{2}^3$	31 662	-	-	38 129

Table 5.2: Resulted CXPI-values from double model computation

The reason why setting number four is not included for either Mesh 2 or Mesh 3 is because of computational memory shortage. The panelization became too refined for the computer to handle. In total 14 different mesh settings were evaluated in the double model computations.

When running a linear double model computation, as explained in the introduction of this chapter, the resistance of the hull should be zero. From the computations in SHIPFLOW a coefficient called the CXPI-value will be received which is the integration of the pressure in x-direction. This value, which will not be zero, is considered as the discretization error. The aim is to get as low CXPI-value as possible for the hull mesh. The assumption that Mesh 4 would be the most suitable mesh turned out to be wrong when comparing the CXPI-values from the double model computations. Mesh 4 resulted in the highest value except from Mesh 1. In Table 5.3 the results from the double model computations are presented and Figure 5.5 shows a diagram where the CXPI-values for the different meshes have been plotted. The x-axis represents the different settings for each hull mesh.

	CXPI			
Setting no.	**Mesh 1**	**Mesh 2**	**Mesh 3**	**Mesh 4**
1	8.01E-05	4.76E-05	3.25E-05	5.80E-05
2	6.89E-05	3.45E-05	2.94E-05	5.45E-05
3	5.93E-05	3.67E-05	3.31E-05	5.63E-05
4	5.68E-05	-	-	6.13E-05

Table 5.3: CXPI-values from double model computation

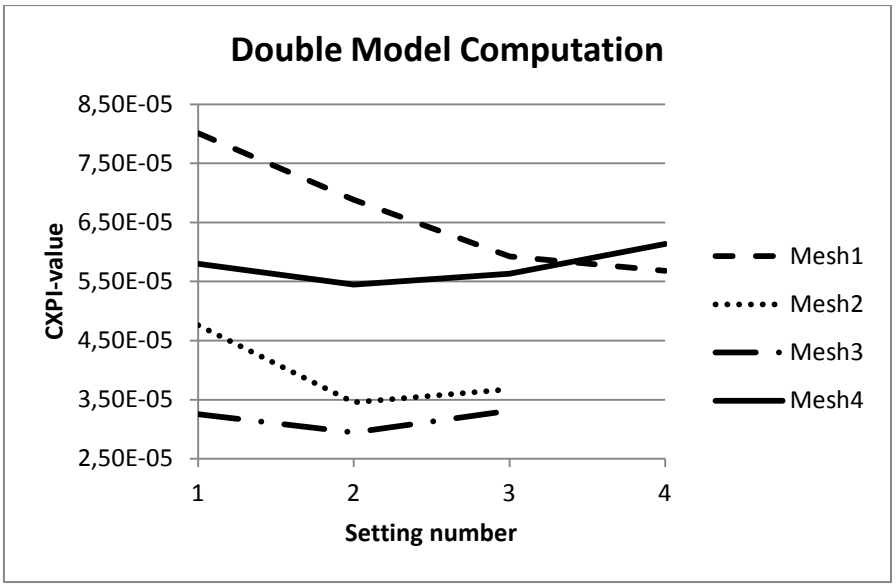

Figure 5.5: CXPI-value for the different meshes in the double model computation

When systematically doubling the number of panels, the CXPI-value should in general first be decreasing and then increasing which will create a downward peak where the optimum number of panels is found (Bathfield, E-mail, 2011). For all meshes in the evaluation, except for Mesh 1, the lowest CXPI-value is received at setting number two. For Mesh 1 the CXPI-value is just decreasing when the number of nodes is systematically doubled and the optimum number panels is not found in this interval.

According to the double model computations the mesh with the lowest discretization error, lowest CXPI-value, is Mesh 3 with setting number two. However, this hull mesh was not chosen for the final computations due to the number of panels. Only the hull mesh consists of 12086 panels and since there will be several meshes included, on for example the free surface, in later computations the number of panels on the hull mesh alone should therefore not be too high. It was decided on beforehand to use a hull mesh with approximately 4000 panels in the analysis so instead any of the meshes with setting number one should be chosen where the numbers of panels are between 3500-6000.

Since Mesh 4 had the most squared panels, the smoothest transition between the different hull groups and the lowest number of panels it was chosen as the final mesh to be used in the analysis. In chapter 5.5.1.1 there will be diagrams showing results from potential flow computations run on each mesh. These clearly show that there was no big difference in the results between Mesh 3, with the lowest CXPI-value, and Mesh 4, the chosen mesh. When looking at the computed values for Mesh 4 it can also be seen that the wave resistance coefficient is lower than the CXPI-value, as it should. At 10 knots the value of C_W is 7.58E-04 and the value of CXPI is 5.80E-05, thus showing that CXPI << C_W.

5.2.2 Zero trim, loaded condition

Before doing double model calculations for refined meshes a good starting mesh had to be selected. This was done by trying out different panel distributions while maintaining around 4 000 panels in total. Different stretch modes were also tried to place densely packed panels where they may be needed most, primarily at the bow/bulb, stern and skeg. This was done to keep a good representation of the hull geometry and to create smooth transitions between the different hull groups in the offset file.

The hull mesh that yielded the best CXPI value together with a good representation of the hull geometry can be seen in Figure 5.6 and is denoted as Mesh 1 in the following tables. This is the coarsest hull mesh used in the double model comparison. The meshes were refined by taking the stations and points and multiply them with a refinement factor of $\sqrt{2}, \sqrt{2}^2$ and $\sqrt{2}^3$ to create a total of four meshes where the finest one had 8 times as many panels as the coarsest one.

The settings used for the calculations can be seen in Table 5.4 below and Mesh 1 can be seen in Figure 5.6.

Group	Parameter	Mesh 1	Mesh 2	Mesh 3	Mesh 4
Hull	**station**	80	113	160	226
Hull	**point**	28	40	56	79
Stern	**station**	36	51	72	102
Stern	**point**	27	38	54	76
Bulb	**station**	18	25	36	51
Bulb	**point**	20	28	40	57
Skeg	**station**	36	51	72	102
Skeg	**point**	10	14	20	28
FlatSkeg	**station**	36	51	72	102
FlatSkeg	**point**	3	4	6	8
Refinement Factor		1	$\sqrt{2}$	$\sqrt{2}^2$	$\sqrt{2}^3$

Table 5.4: Settings for double model calculations, loaded case

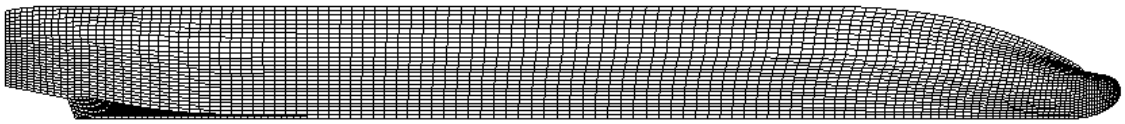

Figure 5.6: Mesh 1 for double model computations, loaded case

	Mesh 1	Mesh 2	Mesh 3	Mesh 4
CXPI	5.84E-04	5.16E-04	4.71E-04	4.47E-04
Number of Panels	3 751	7 666	15 577	31 359
Number of Nodes	4 040	8 076	16 160	32 185

Table 5.5: Results of double model calculation for loaded case

The results of the double model computations can be seen in Table 5.5 and Figure 5.7. The CXPI Value was slightly reduced for every refinement and at Mesh 4 the value had been reduced by 23 percent compared to Mesh 1. This shows that the computational model is quite insensitive to mesh changes since the number of panels was increased by 8 times between Mesh 1 and Mesh 4. Unfortunately the CXPI value is a lot higher than anticipated. Currently it is of the same order as the computed wave resistance in chapter 5.5.2.1. As previously mentioned in chapter 5.2 it is advisable to have a CXPI value of at least one order of magnitude lower than the expected wave resistance coefficient. Mesh 1 is used for all further computations done.

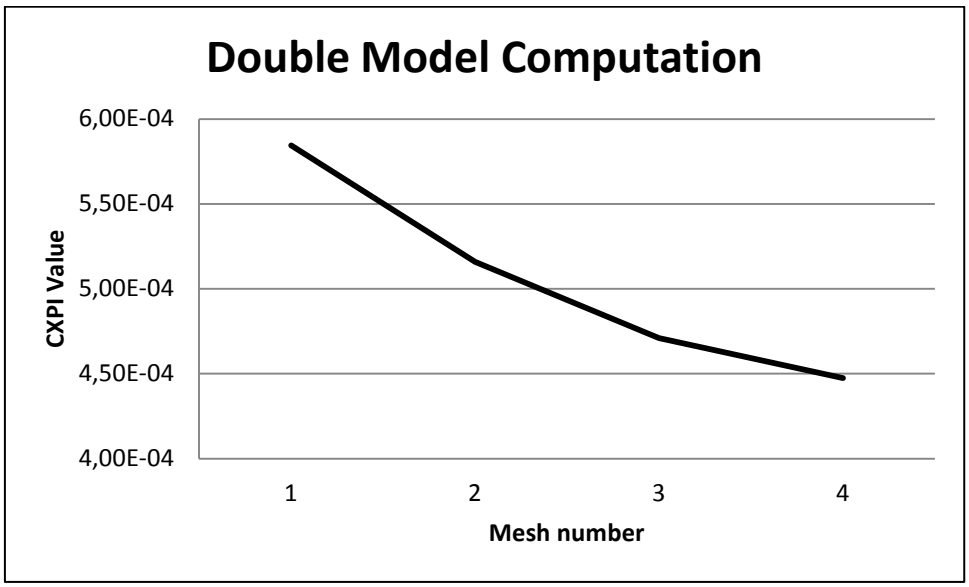

Figure 5.7: CXPI Value from double model computations

5.3 Uncertainty analysis

For the grid convergence study the LSR method described in chapter 2.5 has been used. Five different sized grids according to Table 5.6 were examined starting with Grid 1 and then refining this grid with a factor $\sqrt[4]{2}$ in every direction for each new grid. This refinement should result in Grid 5 having $2^3 = 8$ times more cells than Grid 1 but due to the grid generator in SHIPFLOW the result is about 6.3 times more cells.

Grid	Refinement factor	No. Cells	hi/h1
Grid 5	1.000	2 932 800	1.000000
Grid 4	1.189	1 876 970	1.160402
Grid 3	1.414	1 171 728	1.357746
Grid 2	1.682	737 673	1.584186
Grid 1	2.000	464 202	1.848666

Table 5.6: Grids used for uncertainty analysis

The computational variables used for the investigation are the friction and pressure force components in x- and y-direction as well as the total force in x- and y-direction. The Iterative error was small enough to be neglected for all examined grids when the frictional force was investigated. For the pressure force the iterative error varied between zero and three orders of magnitude lower than the discretization error. This is generally not small enough to be neglected and also affect the reliability of the total force result.

The observed order of accuracy, p, the constant α and the estimated exact solution ϕ_0 were obtained using the LSR method to solve Eq. 2.29. The results for each computational variable can be found in Table 5.7 and curve fittings for the variables $F_{x,f}$ and $F_{y,f}$ can be seen in Figure 5.8 and Figure 5.9 where the circles represent the computational results for the different grids. The starting values for the LSR solver was set to $(\phi_0, \alpha, p) = (0,0,2)$. As can be seen in Table 5.7 the computed value for the order of accuracy, p, did not change for this input. However, slightly different input values resulted in changed p values as well.

	Fx_p	Fy_p	Fx_f	Fy_f	FX	FY
$\boldsymbol{\phi_0}$	9.18E-05	-9.85E-04	6.12E-05	1.28E-06	1.53E-04	-9.84E-04
$\boldsymbol{\alpha}$	-5.39E-06	-3.38E-06	-6.16E-07	1.29E-07	-6.15E-06	-3.32E-06
$\boldsymbol{p}$	2	2	2	2	2	2

Table 5.7: Solution from Least Square Root fit

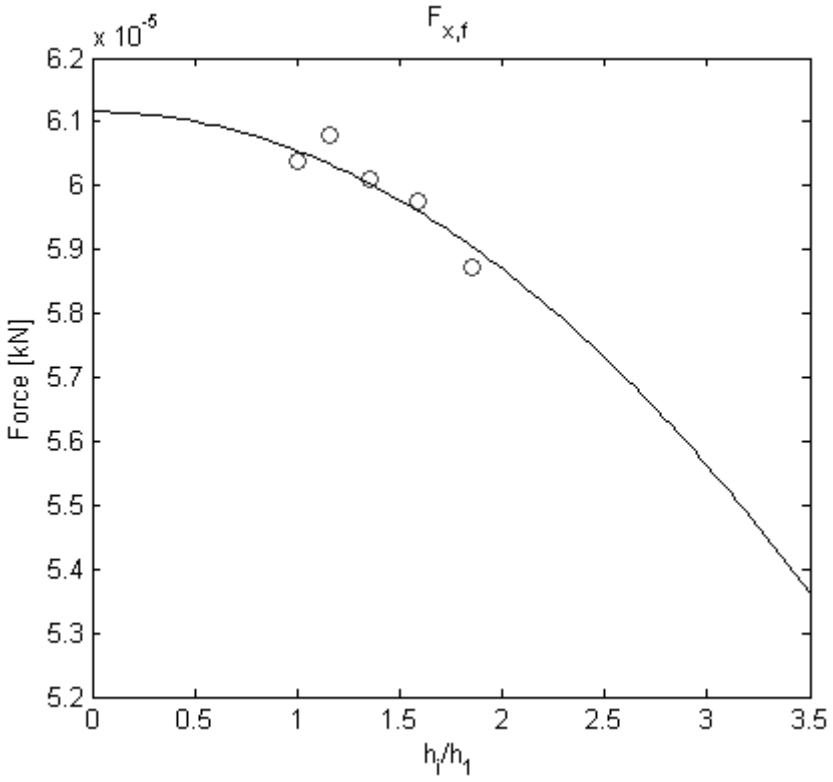

Figure 5.8: Grid convergence of Fx,f

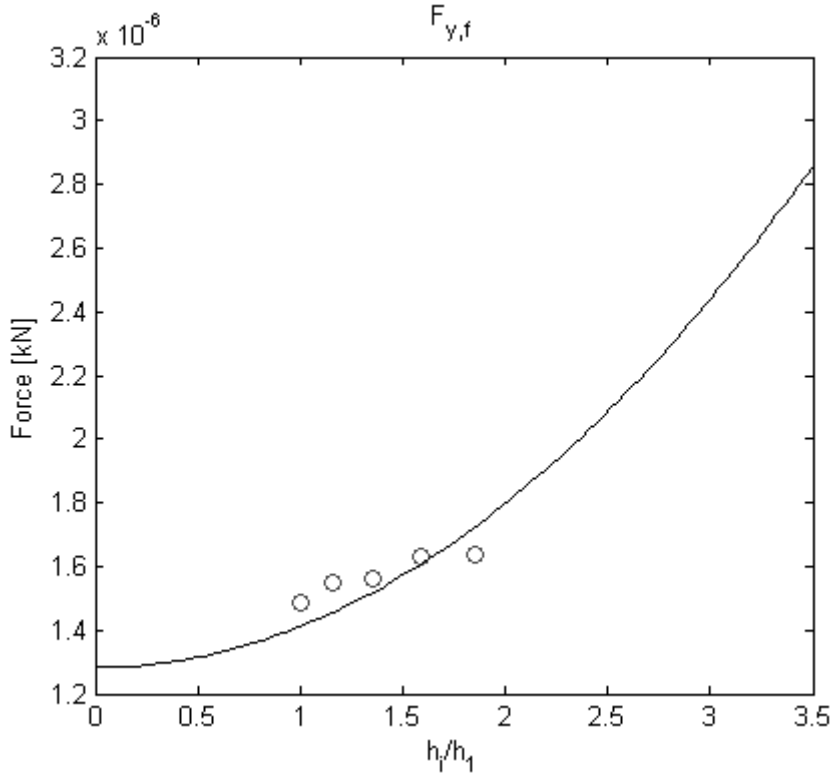

Figure 5.9: Grid convergence of Fy,f

The obtained values in Table 5.7 together with equations 2.28 and 2.30 make it possible to determine the uncertainty of the computed solution using the criteria described in chapter 2.5. The uncertainties for the different grids are presented as a percentage of the computed variable and can be found in Table 5.8. The complete numerical results can be found in Appendix L.

Uncertainty in percentage of computed values						
	Fx_p	**Fy_p**	**Fx_f**	**Fy_f**	**FX**	**FY**
Grid 5	-7.81%	0.43%	-1.27%	10.81%	-5.24%	0.42%
Grid 4	-10.72%	0.57%	-1.71%	14.01%	-7.12%	0.56%
Grid 3	-14.69%	0.79%	-2.36%	19.03%	-9.79%	0.77%
Grid 2	-22.50%	1.06%	-3.23%	24.81%	-14.29%	1.05%
Grid 1	-30.96%	1.45%	-4.48%	33.61%	-19.73%	1.43%

Table 5.8: Uncertainty due to grid spacing

When evaluating the results in Table 5.8 focus on the results for $F_{x,f}$ and $F_{y,f}$ where the iterative error is negligible. The uncertainty varies a lot between the different variables. This may be caused by the scatter in the computations which can be observed in Figure 5.8 and Figure 5.9 which made the curve fitting using LSR difficult and instable. For example, the curve in Figure 5.9 is a very poor representation of the computed values. With a more accurate least squares solution for $F_{y,f}$ the uncertainty could be in the same range as for $F_{x,f}$. The result from the uncertainty analysis is not completely reliable and should therefore only be used as a rough estimate. Grid 3 with approximately 1 200 000 cells will be used for all RANS computations performed.

5.4 Extrapolation from model test

As mentioned in chapter 4.3 the results from the CFD computations were to be verified with the model test results, but first the results had to be extrapolated from model to full scale. In chapter 2.4 the procedure of two different extrapolations methods were described. The model test results for this case have been extrapolated using both methods and will be presented next.

5.4.1 MARIN Form Factor Method

The model tests results were extrapolated by MARIN using their Form Factor Method, explained in chapter 2.4.2. The form factor, *1+k*, and a model-ship correlation allowance, C_A, presented in Table 5.9 were used in the extrapolation.

T_F/T_A	1+k	C_A
4.80/4.80	1.3	0.0010
0.70/2.60	1.2	0.00120

Table 5.9: Form factor and model-ship correlation allowance

The effects of the still-air drag of normal wind exposed ship and superstructure size are included in C_A.

In this case the friction resistance coefficient was determined using the ITTC-57 equation, Eq. 2.13 and the friction correction force, F_D, was determined using Eq. 2.26.

The extrapolated results are valid for unrestricted deep water of 15°C and a mass density of 1025 kg/m^3. Included in the results, which are presented in Appendix C, is the admiralty coefficient, C_E, which is calculated according to Eq. 5.1 where the displacement volume (DISV) is 6809.1 m^3 for loaded draught and 2165.6 m^3 for the ballast draught. V_S and P_E are in unit knots and kW respectively.

$$C_E = DISV^{2/3} * \frac{V_S^3}{P_E} \qquad \textbf{5.1}$$

5.4.2 ITTC-78 Method

For the verification of the CFD computations only the results from the MARIN Form Factor Method were used. The model test results were extrapolated using the ITTC-78 Method, explained in chapter 2.4.1, since this is the most common method used and also to compare and see how big difference it will be between the two different methods.

When calculating the air resistance coefficient, C_{AA}, the transverse projected area, A_T, is needed (Eq. 2.16) but since it has not been specified for this case C_{AA} was assumed to be the same as the model-ship correlation allowance, C_A, used in the MARIN Form Factor Method. The same form factor was also assumed and ΔC_F (Eq. 2.15) was calculated using the standard value of the hull roughness, k_s, and length at the waterline, L_{WL}. The results from the ITTC-78 Method for both conditions are listed in Appendix D.

Since both methods use the ITTC-57 to determine the friction resistance coefficient these values will be the same. However, there will be differences in the final results since the MARIN method does not include hull roughness in this case.

5.5 CFD Calculations for Full Scale

For symmetry reasons, only half the ship and flow is modeled and computed in SHIPFLOW where the xz-plane is treated as the symmetry plane. RANS calculations are required since this thesis mainly concerns stern variations and because the given case deals with a highly submerged transom.

5.5.1 Trimmed, ballast condition

When performing CFD-computations on the ballast condition the trim angle, θ, needs to be specified in the command-file as the initial position of the ship. It can be solved geometrically (Figure 5.7) with the length between perpendiculars, L_{PP}, the draft at aft perpendicular, T_a, and the draft at forward perpendicular, T_f (Eq. 5.2).

$$tan\theta = \frac{t}{L_{pp}} = \frac{T_a - T_f}{L_{pp}} \qquad \textbf{5.2}$$

Where,

t = trim, difference in draft at forward and aft perpendicular

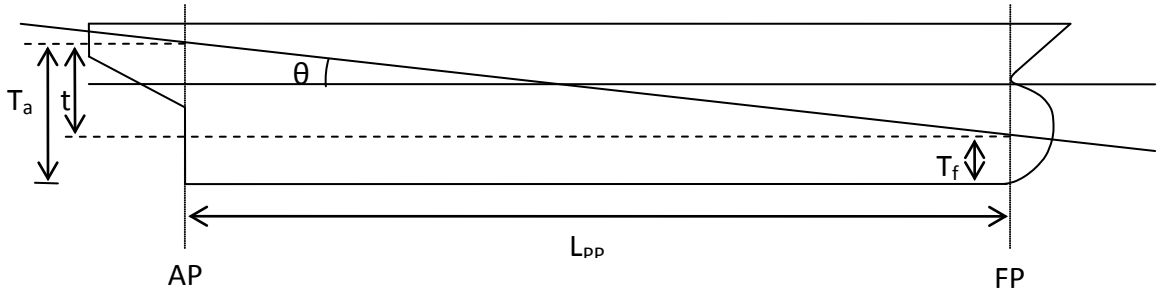

Figure 5.10: Trim angle

In the command-file also the computational coordinate system has to be specified. For a trimmed condition, like the ballast condition in this analysis, the z-origin is specified as the mean draft, T_m, which is defined as the mean value of T_a and T_f (Eq. 5.3).

$$\frac{T_a + T_f}{2} = T_m \qquad \textbf{5.3}$$

Inputs needed to solve above equations for the split hopper barge are found in Table 4.1 and the results will then be;

- Trim, t = 0.90m
- Mean draft, T_m = 1.65m
- Trim angle, θ = 1.23°

Figure 5.11 shows a sketch of the ballast condition and where the waterline is situated. Almost the entire bulb is situated above water for this condition due to low drafts and a large trim angle. This is not a very common for a ship but it is a necessary condition for a hopper barge where the load will be very heavy. There are special rules applied to hopper barges since their conditions are not very common. For example they have special regulations on the freeboard, which is the distance between the water level and the top of the deck. Since these barges are heavily loaded they will have a very small freeboard.

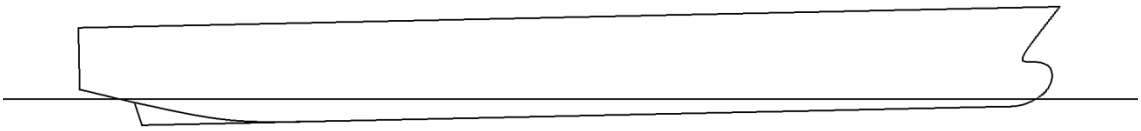

Figure 5.11: Location of waterplane in ballast condition

The Froude and Reynolds numbers (Eq. 2.8 and 2.9) will be different for respective speed in the speed range, which is 8-12 knots for the ballast condition. Since they have to be specified in the command-file they need to be calculated for each speed. In the model test the Froude and Reynolds numbers were based on the length overall submerged, L_{OS}, and therefore this length has been used also for the CFD-computations. The values of the Froude and Reynolds numbers (based on L_{OS} from Table 4.1) that have been used in the CFD computations are listed in Table 5.10.

Froude and Reynolds number						
V_s [kn]	8.00	9.00	10.00	11.00	12.00	13.00
F_n [-]	0.1389	0.1562	0.1736	0.1910	0.2087	0.2257
R_n [-]	3.1013E+08	3.4890E+08	3.8766E+08	4.2643E+08	4.6520E+08	5.0396E+08

Table 5.10: Froude and Reynolds number for ballast condition

The value of water viscosity, ν, is also needed as input in the command-file. Since it is specified in the report from MARIN that the extrapolated values from the model test are valid for unrestricted deep water of 15°C this temperature of sea water is assumed in the CFD-computations. According to tables from ITTC the viscosity will then be $1.18431*10^{6}$ m^2/s (ITTC, 2006).

As can be seen in Figure 5.11, when the split hopper barge is operating in ballast condition the transom will not be submerged into water. When running potential flow computations on a hull with a so called dry transom not only a hull and a free surface mesh is needed but there should also be a mesh for the transom flow at the free surface aft of the ship included (Figure 5.12). For the loaded condition the transom will be submerged, a so called wet transom, and a transom mesh is therefore not needed in this case. This is further explained in chapter 5.5.2 and was also confirmed by Christian Veldhuis at MARIN (Veldhuis C. , 2011).

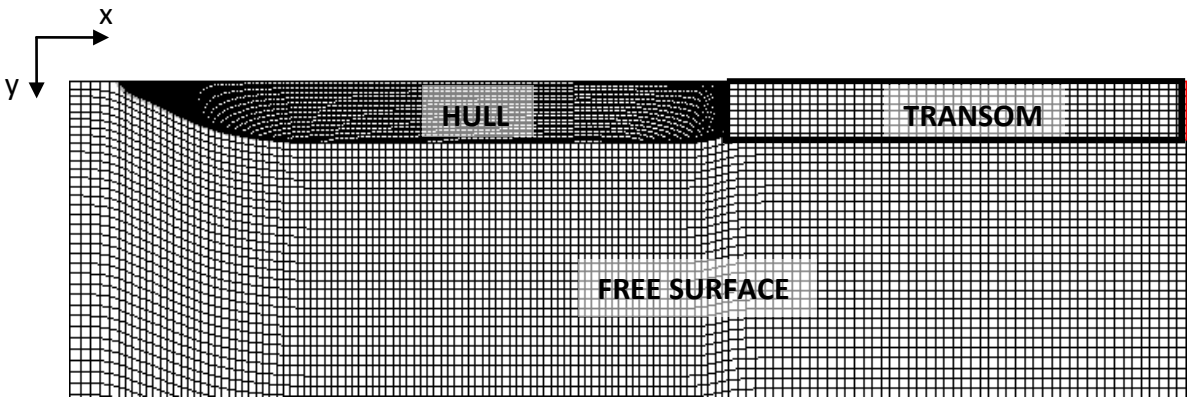

Figure 5.12: Meshes included in potential flow calculations, ballast condition

5.5.1.1 Potential Flow Computations

In the beginning of the analysis several potential flow computations were run on single speeds to make sure that all settings were correct. When the right settings had been achieved some series of potential flow computations, including all speeds in the speed range, were run and some of them will now be presented.

For the free surface mesh the FLOWTECH recommended free surface panelization was to begin with used. The settings for this recommended panelization are listed in Appendix E for each speed in the speed range.

For the first series, called Series 1, the computations were run using Mesh 1 described in chapter 5.2.1. For the second series, called Series 2, Mesh 2 described in the same chapter was instead used. Also mentioned in this chapter is that Mesh 4 was chosen as the final hull. However these series, using Mesh 1 and Mesh 2 instead, were run before the different meshes had been compared in the double model computations.

For both Series 1 and Series 2 the number of points in the transom mesh were set to five for all speeds in the speed range and the number of stations was set to be equal to the number of stations aft of the hull for the free surface panelization so that the panel size on the x-axis would be equal for both the transom and the free surface mesh.

As mentioned in chapter 2.2, from the potential flow solver in SHIPFLOW, XPAN, the wave resistance and wave pattern can be received. In Figure 5.13 the resulted values of the wave resistance coefficient, C_W, from XPAN for Series 1 and Series 2 are plotted together with the values of the specific residual resistance coefficient, C_R, from the model test. The resulted values are also listed in Appendix F. These two resistance coefficients, C_W and C_R, cannot be directly compared because CFD often predicts the wrong level of resistance and also the value of C_R is determined by the form factor used during the model tests and can affect the correlation with CFD-results. However, the curves should be parallel with only a shift in y-direction. The C_W-values can then be corrected to match C_R from the model tests by applying a correction factor for all speeds (Bathfield, E-mail, 2011).

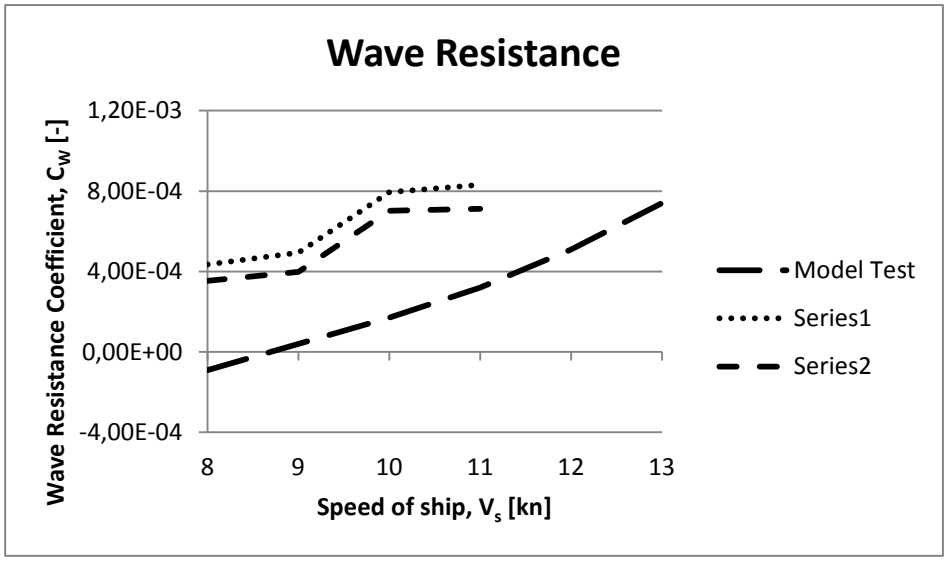

Figure 5.13: Wave resistance coefficient for Series 1, Series 2 and specific residual resistance coefficient for model test

The diagram shows that Series 2 results in slightly lower values of C_W than Series 1. The only difference between these series is the hull mesh so it is due to the panelization that we get this difference with Mesh 2 being the most preferred mesh since the wave resistance for this mesh was closer to the model test results. Both curves have the same shape but they are not parallel to the curve from the model test results. There is a distinct step between the values at 9 and 10 knots for both series. Since there is a significant difference in wave resistance between the two speeds there should also be differences in the wave patterns (Figure 5.14-Figure 5.15) At 10 knots there is a more distinct bow wave which causes high resistance.

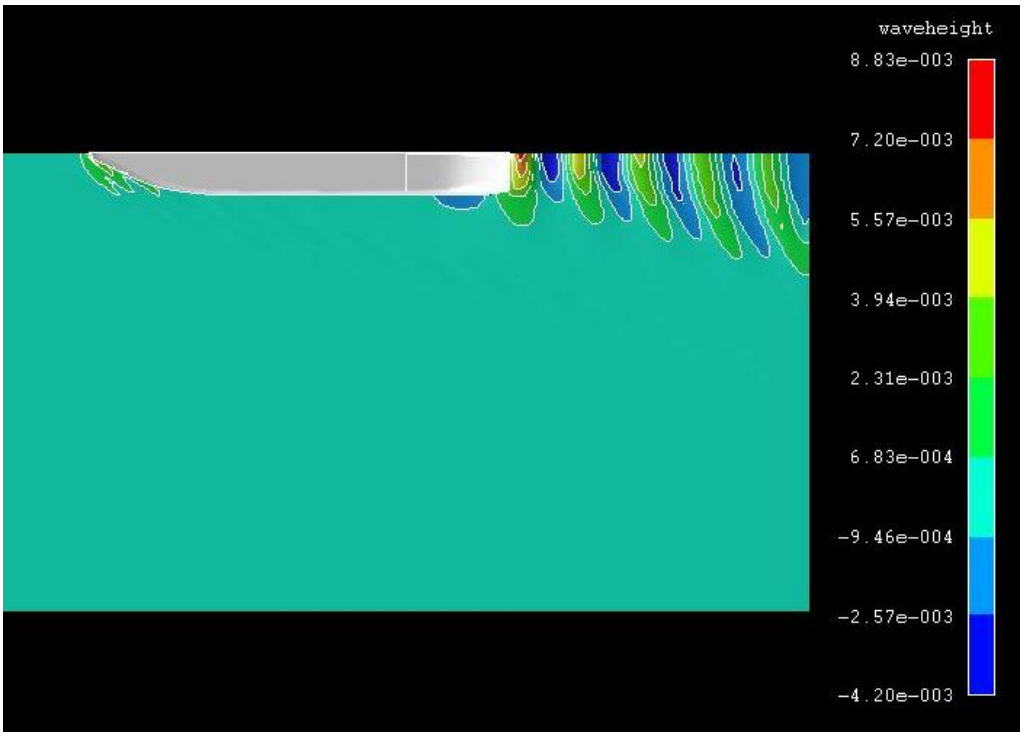

Figure 5.14: Wave pattern at 9 knots, Series 2

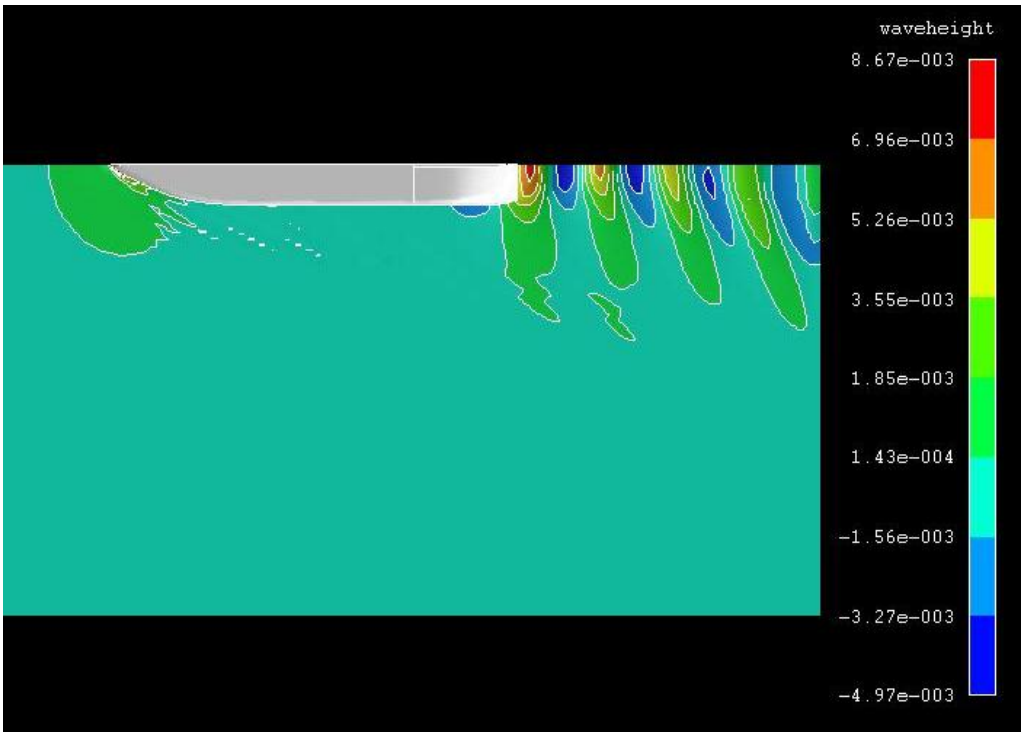

Figure 5.15: Wave pattern at 10 knots, Series 2

The reason why there are no results for 12 knots is because the computations at this speed had not yet converged after the maximum number of iterations, it was pending between two values, and therefore it was not included in the diagram. There are also no results for 13 knots from the CFD computations included in the diagram since the solutions diverged at this speed for both series. There have been difficulties in general with receiving converged solutions for 13 knots and throughout the analysis only diverged results have been received for all computations run at this speed. It can be more difficult for the higher speeds to converge and a lot of iterations are needed. One reason is because of the wave that is created by the bulb. For higher speeds this wave becomes very steep. In reality the wave would break but SHIPFLOW cannot handle wave breaking.

When looking at the free surface and transom meshes (Figure 5.16), as already mentioned, the size of the panels on the x-axis is equal for the transom and the free surface mesh aft of the hull. However on the y-axis the panel size is considerably larger for the transom than for the free surface.

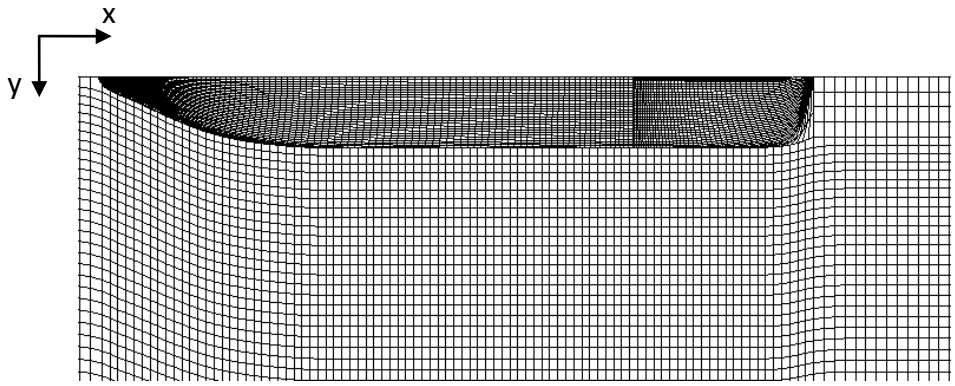

Figure 5.16: Free surface mesh for Series 1 and Series 2

For the third series of potential flow computations, Series 3, the difference in panel size on the y-axis was avoided to see if this would result in more accurate results. This was done by increasing the number of points in the transom meshes for respective speed to the following:

- 8-9 knots: 9 points
- 10-11 knots: 8 points
- 12-13 knots: 7 points

The reason why the number of points on the transom mesh is different for different speeds is because the panel size in the y-direction on the recommended free surface mesh is different for each speed and therefore the number of points at the transom is different for each speed to match the panel size of the free surface.

The change in the transom mesh resulted in more equally sized panels aft of the hull for all speeds (Figure 5.17). It also resulted in a converged solution at 12 knots.

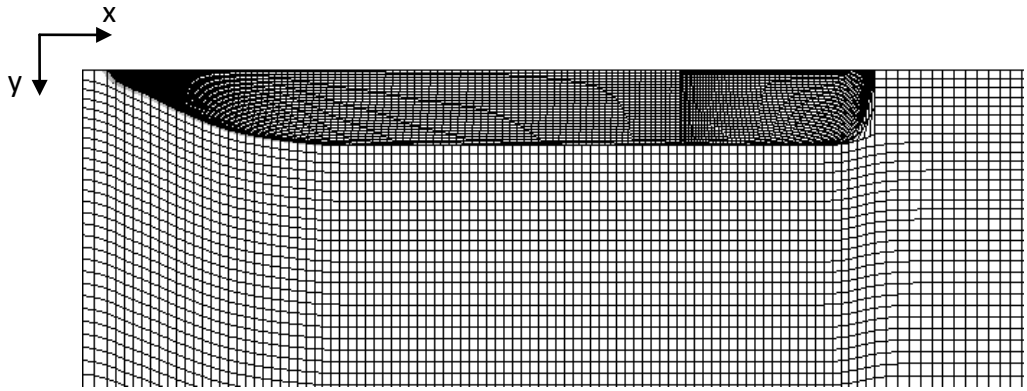

Figure 5.17: Hull and free surface mesh at 10 knots, Series 3

The resulted values of the wave resistance coefficients in Series 3 are plotted together with the results in Series 2 as comparison (Figure 5.18) since the same mesh as in Series 2, Mesh 2, was used in Series 3. The resulted values are listed in Appendix F.

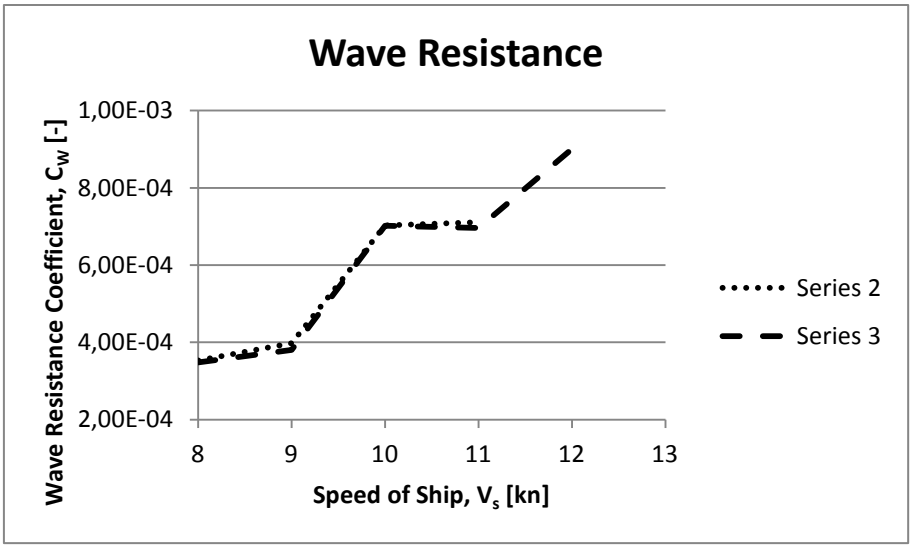

Figure 5.18: Wave resistance coefficient for Series 2 and Series 3

The shape of the curve for Series 3 ended up as the same as for Series 2. There is still a distinct step between the values at 9 and 10 knots and there is a very small difference between the values for the two series. However, as mentioned before, the solution at 12 knots converged when the number of points in the transom mesh was increased. It was decided to use the number of transom points according to Series 3 for all computations hereafter.

The next series, Series 4, was run using the final Mesh from the double model computations, Mesh 4. The results from the potential flow computations are presented in Figure 5.19. In this diagram also the results from Series 5 are included. This series was run using Mesh 3 since it resulted in the lowest CXPI-value in the double model computations. The resulted values of C_W for both series are also listed in Appendix F.

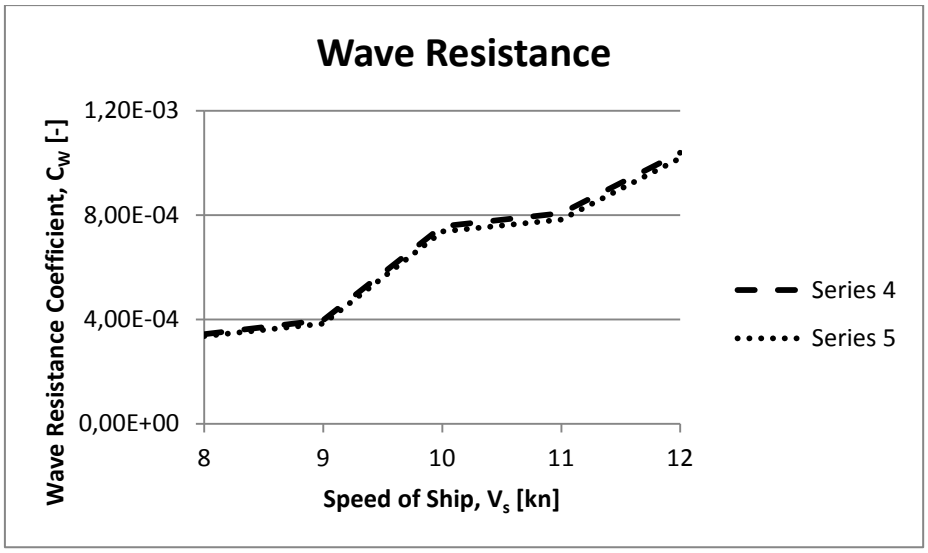

Figure 5.19: Wave resistance coefficient for Series 4 and Series 5

As mentioned in chapter 5.2.1, the difference between Mesh 3 and Mesh 4 when running potential flow computations turned out to be very small. However, as in previous series, there is still a distinct step between the values at 9 and 10 knots and the shapes of the curves are not parallel to the curve from the model test.

Another rule of thumb when it comes to grid settings is that there should be at least 25 panels per wavelength at the free surface along the hull. (Bathfield, E-mail, 2011). In the FLOWTECH recommended free surface panelization that have been used so far there are, in this speed range, only about 16-18 panels per wavelength along the hull, 11-12 panels per wavelength in front of the hull and 12-13 panels per wavelength aft of the hull. Several computations have been run for the ballast condition in SHIPFLOW where the panels per wavelength on the free surface have been increased to see if this might result in more accurate results compared to the model test. Except from increasing the number of panels per wavelength also the size of the free surface panelization has been changed in several different ways to see if this would have any impact. Since most of these computations have diverged and since only a few of them have converged no results are presented in the report.

Series 4 was extended to include also potential flow computations run at 9.2, 9.5 and 10.5 knots to see whether the high value at 10 knots is just a deviation at this speed, and if so disregard this value and proceed with the analysis. This extended series is called Series 4b. It turned out that the values at 9.5 and 10.5 knots were very close to the value at 10 knots and that a sudden increase of the wave resistance coefficient is now occurring between 9.2 and 9.5 knots instead (Figure 5.20). The resulted values of the wave resistance coefficient are listed in Table 5.11. Since the result at 10 knots was not just a deviation no further potential flow computations were run on the ballast condition.

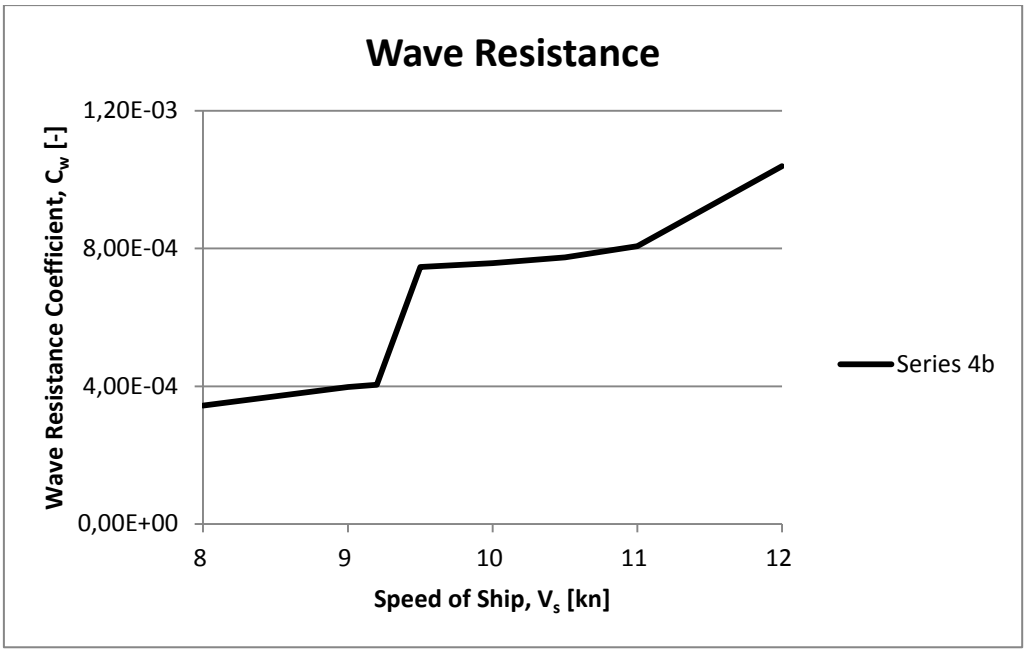

Figure 5.20: Wave resistance coefficient for Series 4b

Series 4b								
V_s [kn]	8.00	9.00	9.20	9.50	10.00	10.50	11.00	12.00
C_w [-] [$\cdot 10^{-4}$]	3.44	3.97	4.05	7.46	7.58	7.74	8.07	1.04

Table 5.11: Wave resistance coefficient for Series 4b

In the report from MARIN there is a diagram from the model test showing the change of level due to speed. This diagram includes the change of trim angle, draft at forward perpendicular and draft at aft perpendicular at respective speed (Appendix G). Although the diagram from MARIN shows results from a test including propellers a comparison was made with the outputs from SHIPFLOW without propellers. When including a propeller it will introduce a force where the vertical position can be different from the centre of buoyancy which will introduce a moment which influences the trim (Vesting, E-mail, 2011). Because of this the outputs from SHIPFLOW are not directly comparable to the model test but the comparison is made to see if there is anything noticeable. The change of level was compared by plotting the dynamic trim angle and the dynamic drafts, meaning the resulted trim angle and drafts when operating. The diagrams are shown in Figure 5.21-Figure 5.23 and the values are listed in Appendix H.

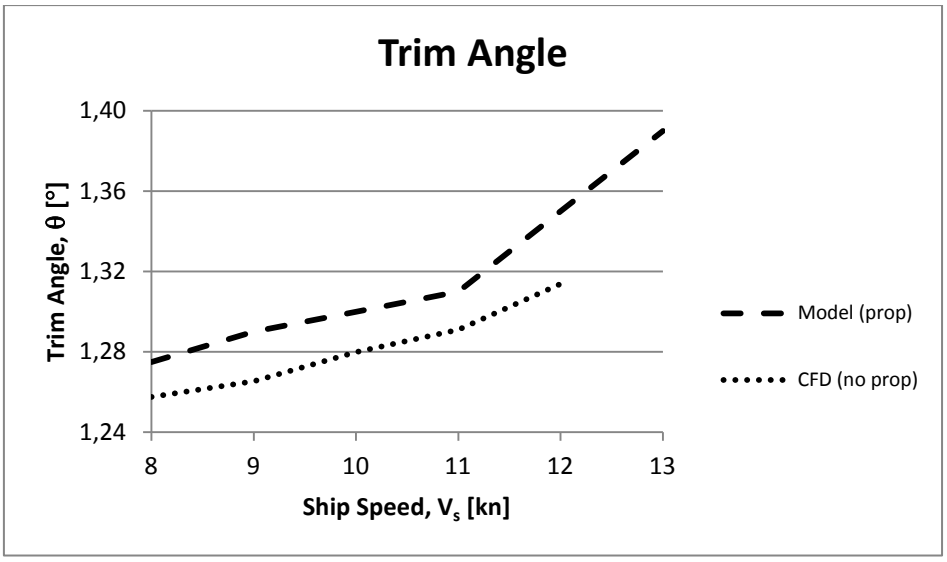

Figure 5.21: Dynamic trim angle

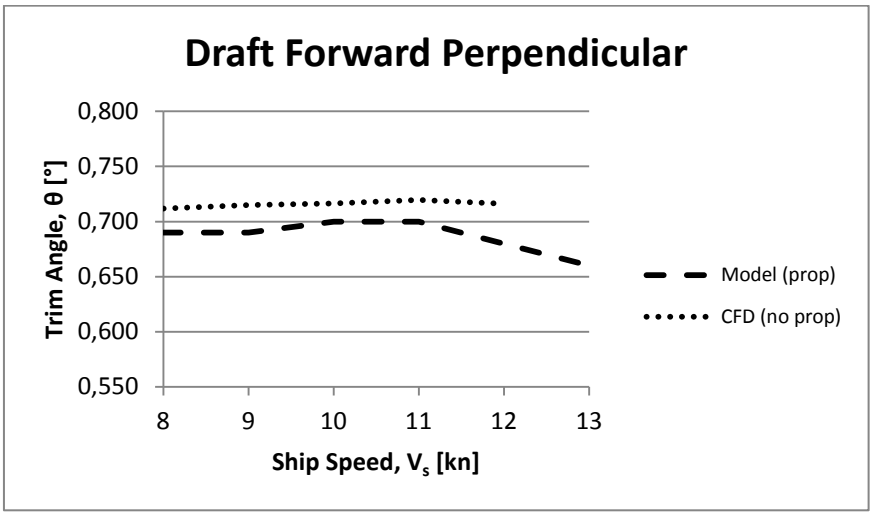

Figure 5.22: Dynamic draft at forward perpendicular

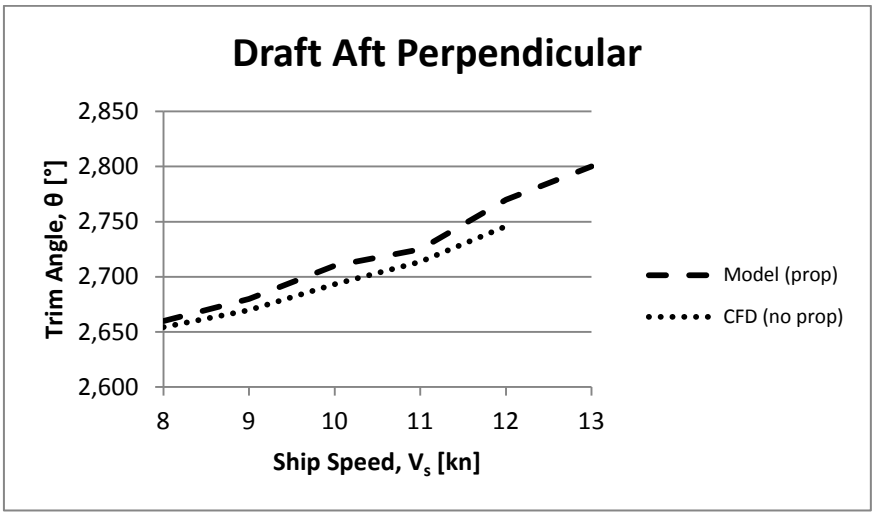

Figure 5.23: Dynamic draft at aft perpendicular

Nothing strange that could be the cause of the distinct step between 9 and 10 knots in the CFD computations can be noticed from the diagrams. The results from SHIPFLOW are close to the model test with only some minor differences due to the propellers.

Finally the hydrostatics of the barge were checked and it was then realized that the longitudinal centre of buoyancy, LCB, and the block coefficient, C_B, received from SHIPFLOW were not correct. These values and also the wetted surface area, S, and the displacement, V, are listed together with the values from the model test in Table 5.12.

	C_B [-]	LCB [m]	S [m^2]	V [m^3]
CFD	0.524	51.35	1 650.1	2 148.4
Model	0.824	46.91	1 649.3	2 165.6

Table 5.12: Hydrostatics from SHIPFLOW and model test

Since the differences between the values of LCB and C_B from SHIPFLOW compared to the values from the model test were quite big the offset-file used in the CFD computations was checked using another software. The results received were similar to the model test results and it could therefore be concluded that there is at least nothing wrong with the offset-file. This will be further discussed in chapter 7.

Due to the inaccurate value of LCB and C_B in SHIPFLOW the resulting values are not comparable to the results from the model test. Worth discussing can be whether this is the reason why there is a peak at 10 knots for the wave resistance or not. However, one of the reasons could also be that the panels per wavelength were too few or that the size of the free surface was too small. This condition is, as mentioned in the beginning of this chapter, not very common; having a very low draft and a large trim, with almost the entire bulb being above the water surface. Therefore it might be that it is a difficult case to handle in CFD. Figure 5.24 shows a picture of the ballast condition at 10 knots during the model test and it clearly shows how almost the entire bulb is situated above water.

An e-mail was sent to the support at FLOWTECH to ask about this problem. Leif Broberg, the managing director, replied and explained that there is a bug in the software which causes this problem for trimmed conditions. It is hard to detect for small trim angles but since the trim angle in this case is quite big the problem became significant. One way to get around the problem, as explained by Leif Broberg, is to rotate data in the offset-file externally in for example Frameworks (Broberg, 2011). Due to time constraints we didn't go further in the analysis on the ballast condition.

Figure 5.24: Wave profile along the hull at 10 knots during model test (Veldhuis & Pouw, 2008)

5.5.1.2 RANS Computations

When running RANS computations together with boundary layer and potential flow computations some of the outputs received in SHIPFLOW are the frictional resistance coefficient, $C_{F,}$ the viscous pressure resistance coefficient, C_{PV}, the viscous resistance coefficient, C_V, and the total resistance coefficient, C_T. The values of the frictional resistance coefficients from SHIPFLOW are, in contrast to the wave resistance coefficients, comparable to the values received from the model test. RANS computations were run on the ballast condition, before knowing about the bug, to be able to compare the frictional resistance coefficients with the corresponding values from the model test. In Figure 5.25 the frictional resistance coefficients from the model test are plotted together with the values from SHIPFLOW. The same mesh and settings as in Series 4 from the potential flow computations were used. The values of all coefficients received from the RANS computations are listed in Appendix I.

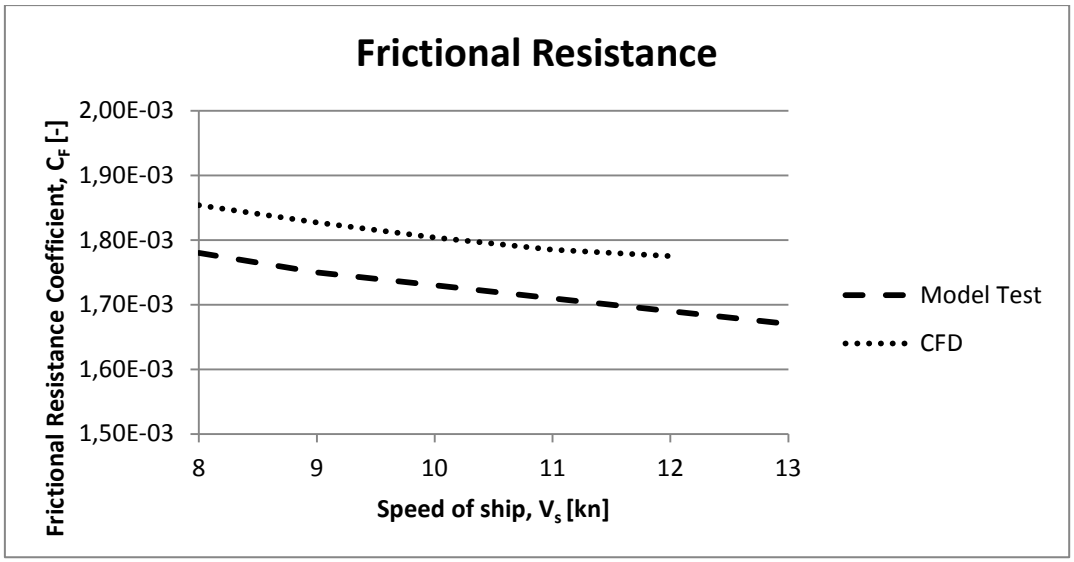

Figure 5.25: Frictional resistance coefficient, CFD and model test

The frictional resistance values from SHIPFLOW are, in contrast to the wave resistance, following the results from the model test. The CFD results are slightly higher, about 4%, than in the model test but the difference is constant for respective speed.

As mentioned in chapter 5.5.1.1 the values of C_W received from SHIPFLOW needs to be corrected before it can be compared to C_R from the model test. Since the total resistance is affected by the wave resistance it also cannot be directly compared to the corresponding values from the model test. The values of the total resistance coefficients from both SHIPFLOW and the model test are plotted together in Figure 5.26 as comparison. The results of the total resistance coefficients from SHIPFLOW are following the same patterns as the wave resistance.

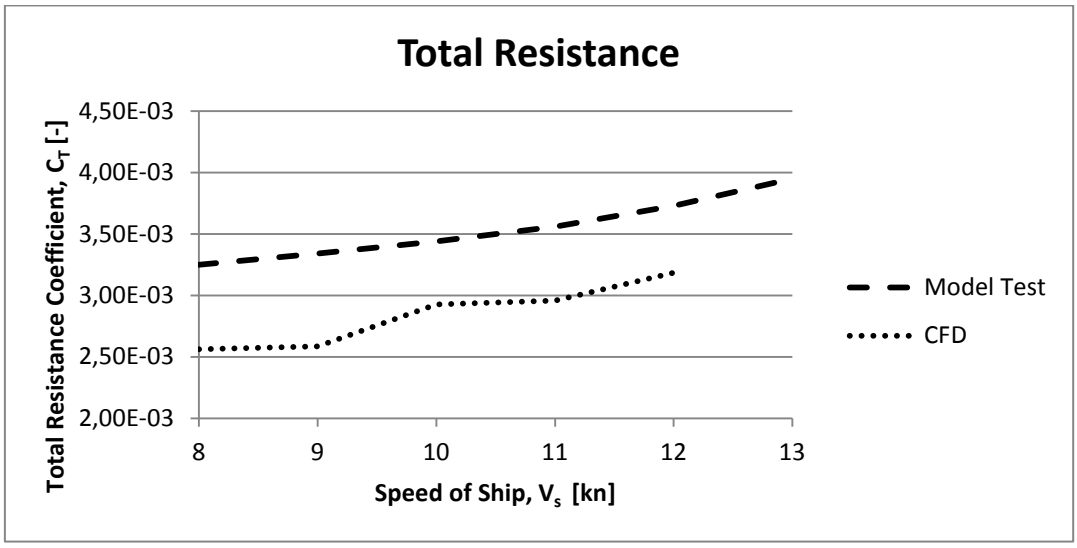

Figure 5.26: Total resistance coefficient, CFD and model test

The corrected value of C_W together with the form factor, 1+k, from SHIPFLOW can be used to obtain a corrected value of C_T which is then used to calculate the total resistance, R_T, and then further the total effective power, P_E, which can be directly

compared to the extrapolated value of the full scale effective power from the model test (Bathfield, E-mail, 2011). Due to the inaccurate values from the computations in SHIPFLOW for the ballast condition, calculating the corrected total effective power will not be useful since these values will also be inaccurate. Since the bug in SHIPFLOW was revealed no further computations have been run on the ballast condition.

5.5.2 Zero trim, loaded condition

A similar calculation has also been performed for the case of a fully loaded dredger shown in Figure 5.27. This case has a constant draught of 4.8 m throughout the ship length which means that no consideration has to be taken to trim angles when creating the input script file for SHIPFLOW.

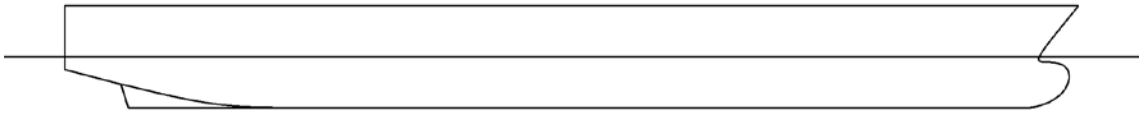

Figure 5.27: Location of waterplane in loaded condition

Since the Froude and Reynolds numbers are based on the overall submerged length they will be different from the unloaded condition. Using equations 2.8 and 2.9 together with the value of LOS for loaded condition found in Table 4.1 and the same viscosity used in the unloaded condition gives the Froude and Reynolds number in Table 5.13.

Froude and Reynolds numbers						
V_s [kn]	7	8	9	10	11	12
F_n	0.1180	0.1349	0.1517	0.1686	0.1855	0.2023
R_n	2.8774E+08	3.2884E+08	3.6995E+08	4.1105E+08	4.5216E+08	4.9326E+08

Table 5.13: Froude and Reynolds numbers for loaded condition

Figure 5.27 shows that that the transom is submerged in the loaded case. This leads to a somewhat different approach than in the previous trimmed case concerning the transom panelization in SHIPFLOW. The submerged transom results in a dead water region behind the transom and a highly viscous flow that SHIPFLOW is unable to model correctly. It is thus inappropriate to use the same transom panelization used in the unloaded case. Instead a stretched region is introduced according to Figure 5.28 where a triangular area directly behind the ship is neglected.

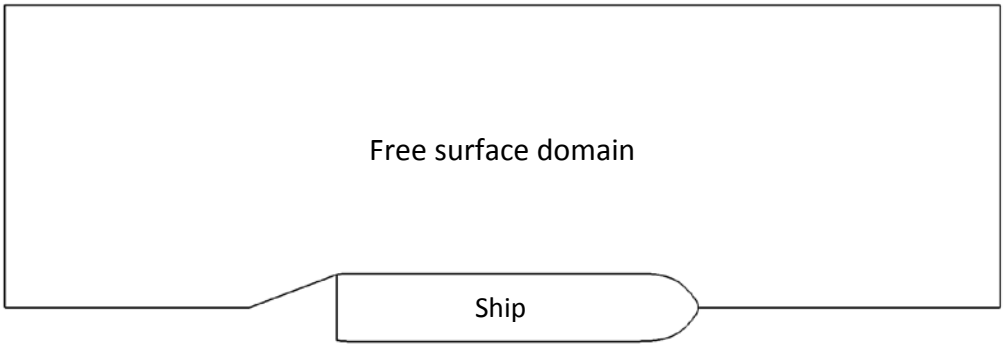

Figure 5.28: Calculational domain for potential flow

5.5.2.1 Computations for loaded condition

It took several runs to find suitable input parameters for this particular hull so a number of computational series were run to try out different settings, just as for the unloaded case. It was decided that FLOWTECHs recommended free surface panelization was not satisfactory enough so the free surface panelization was increased according to Table 5.14.

Area of application	Panels per wavelength
Ahead of the ship	14
Along the ship length	20
Behind the ship	18

Table 5.14: Free surface panelization

According to literature a rule of thumb is to use 25 panels per wavelength (Larsson & Raven, 2004). This proved to be impossible due to memory shortage on the computational resources used. However, comparative computations have been made for higher panels per wavelengths than mentioned in Table 5.14 with very minor differences. The values should therefore be good enough for the survey in this report.

Because of the submerged transom it is not reliable to calculate the wave resistance coefficient in the same way as for the unloaded case, by using pressure integration. Instead the wave resistance coefficient is calculated by analyzing the wave pattern. If the wave resistance coefficient is calculated by the transverse wave cut method it is referred to as CWTWC while it is referred to as CW if it is calculated by pressure integration. SHIPFLOW returns values for the wave resistance coefficient using both methods and a comparison between CW, CWTWC and the model test value provided by the MARIN report (Veldhuis & Pouw, 2008) can be seen in Figure 5.29.

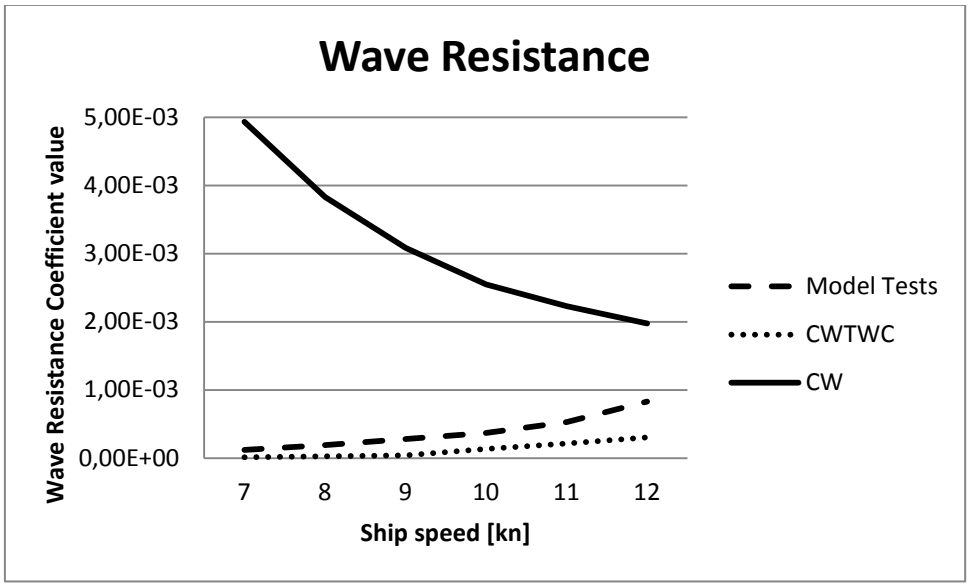

Figure 5.29: Wave resistance coefficient for loaded ship

As it appears in Figure 5.29, CW is completely unreliable for this case with a submerged transom and from now on only CWTWC will be considered when dealing with the loaded case. As mentioned in chapter 2.2.1 the values from CFD calculations regarding wave resistance cannot be compared directly with the values from model tests. Instead of comparing the values the curve shape is compared. When viewing Figure 5.29 one gets the expression that the calculated value captures the behavior less accurate for increasing ship speed. When inspecting the values closer however it is shown that the percentual difference actually decreases with increasing ship speed. The biggest difference occurs for 7 knots where the computed value is 91 percent lower than the model test value. Least difference occurs at 11 knots where the computed value is 59 percent lower than model test results.

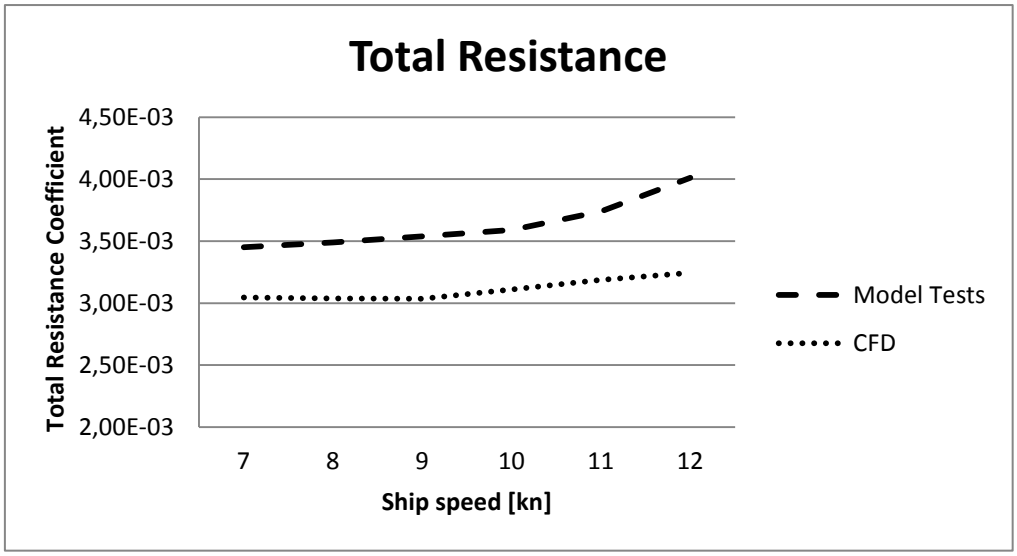

Figure 5.30: Total resistance coefficient for loaded ship

In Figure 5.30 a comparison of the total resistance between the CFD calculations and the model test can be seen. The average difference between Model tests and CFD values is 14 percent. The CFD computations seem to be within reason and only the value for 12 knots differs slightly by being 19 percent lower than the model tests. This is expected due to the difference in wave resistance seen in Figure 5.29. All in all the results is judged as satisfactory. It was expected to receive a lower resistance value from the CFD calculations due to the simplification of the CFD Ship geometry compared to the model used for towing tank tests.

The settings used allow free sinkage and trim in the CFD computations. These values are compared with the model test values provided in the MARIN report (Veldhuis & Pouw, 2008). As mentioned in the unloaded case these values cannot be compared directly since the model test values comes from a self-propelled model. The comparison is done to ensure that no odd behavior occurs in the CFD computations. The trim angle comparison can be seen in Figure 5.31 and the change of level at bow and stern can be seen in Figure 5.32.

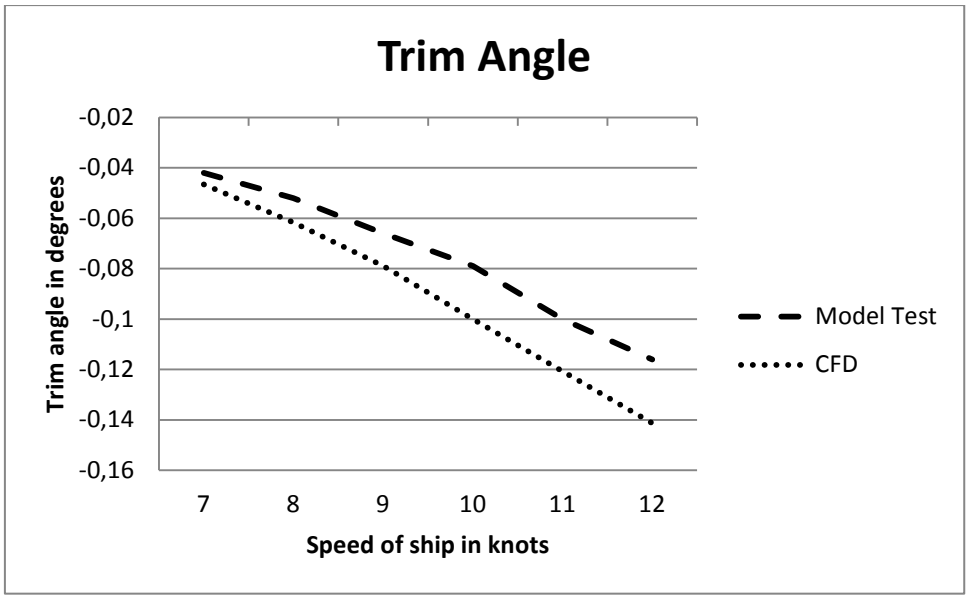

Figure 5.31: Trim angles for loaded ship

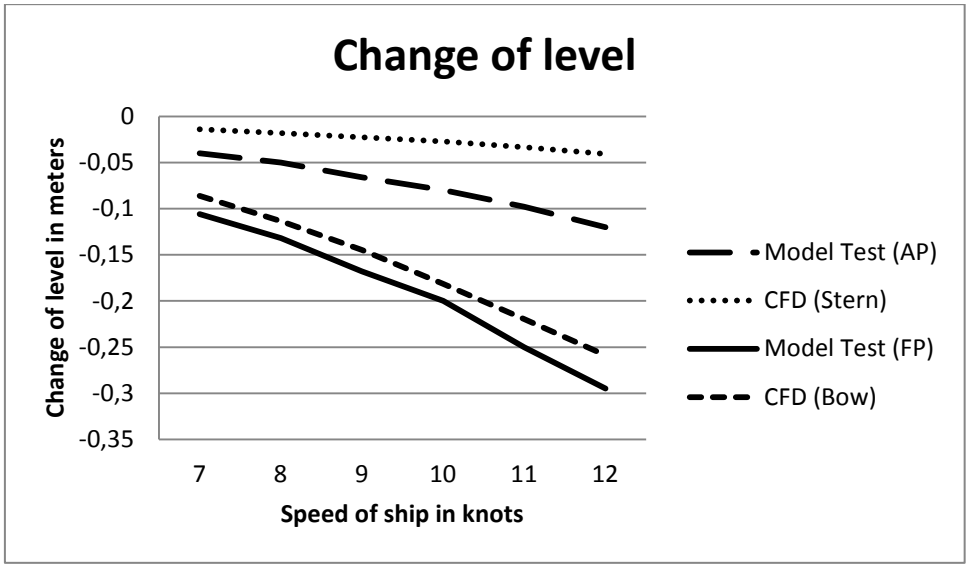

Figure 5.32: Change of level for bow and stern

No strange behavior is observed in either Figure 5.31 or Figure 5.32. The biggest difference is observed in the change of level for the stern. At higher speeds the stern is more submerged for the self-propelled model tests than the CFD computations. A reason for this could be the absence of propeller model and self-propulsion in the CFD computations.

6 Variation of stern inclination

This chapter will concern all computations where the stern inclination is changed. It will be described how the variation was done and the computational results will be presented.

6.1 Generating offsets with different stern inclinations

There is no way of manipulating the stern angle directly in SHIPFLOW, therefore a new offset file is required for each and every stern angle to be evaluated. Creating new 3D models for each angle and then converting the 3D geometry to offsets is a time consuming operation. In this case it is also a very inefficient way since the inclination easily can be changed by 1 dimensional scaling in the longitudinal direction. That is, increase the spacing between the stations on the stern and skeg part to obtain a lesser inclination and decrease the spacing for a larger inclination. Figure 6.1 shows a side view of the stations in an offset file. This offset manipulation is done with a Matlab script, see appendix N.

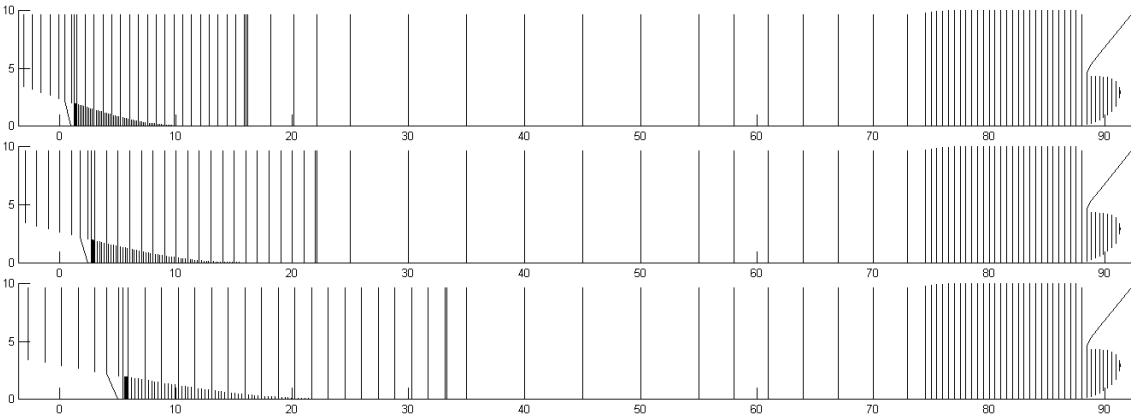

Figure 6.1: Offset-file side view. From top: +4 degrees, reference and -4 degrees of inclination

6.2 Trimmed, ballast condition

Before knowing about the bug in SHIPFLOW for trimmed conditions a series of potential flow computations was run for the ballast condition where the stern angle had been increased with two degrees while the length between perpendiculars was kept. How the barge stern was changed is explained more thoroughly in chapter 6.3. In the potential flow computations on this modified stern the exact same settings as in Series 4 from the computations on the initial hull were used.

The main reason for running this series even though there were problems with the ballast condition was to see if the wave resistance would result in the same manner as for the initial hull. From the potential flow computations run on the modified hull only converged results for 8, 9 and 10 knots were received. The solutions for 11 and 12 knots were pending between two values until the maximum number of iterations was reached. Also for this case there was a distinct step between the values of C_W but this time it occurred between 8 and 9 knots. RANS computations were run on the modified hull at 8, 9, and 10 knots but only results for 10 knots were received without any

errors. After this no further computation was made on this new stern angle or on any other stern angle because of the bug. Due to the lack of results and inaccuracy of the results received there is no use in comparing the new hull with the initial hull for the ballast condition. However the value of C_W and C_T for the new hull at 10 knots is about the same as for the initial hull at the same speed. The resulted values from the computations on the new hull are listed in Appendix J.

6.3 Zero trim, loaded condition

Once it had been established that the CFD computations were reliable enough the investigation with modified sterns started. For the investigation it was chosen that two sterns with a steeper inclination and two sterns with less inclination should be analysed. The CFD model of the existing vessel described in chapter 5.5.2 will act as a reference model. The stern of this vessel is not entirely straight but slightly curved making it hard to specify an angle of inclination. To get an estimate of the inclination and to be able to change the angle in a fair way the reference angle had to be measured. To get a good representation of the curvature, the line from which the angle is measured starts at the lowest point on the stern and ends at the baseline $7/12$ of the length of the curved part, see Figure 6.2. The reference hull angle is 13.5 degrees by measuring the inclination angle this way. The modified sterns will have ± 2 and ± 4 degrees of inclination compared to the reference hull. The two degree step was chosen to cover enough variations in just five data sets and five data sets were chosen to be able to trace and identify trends in the computational results.

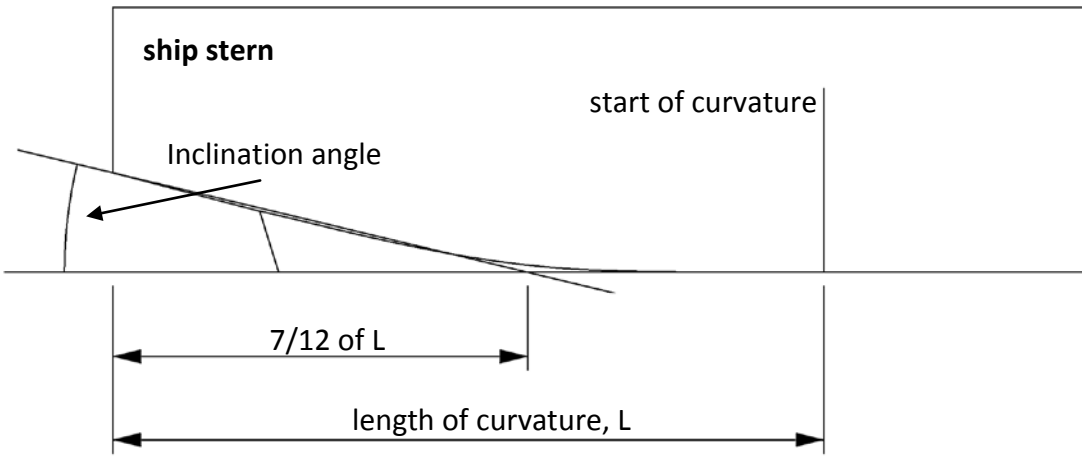

Figure 6.2: Stern inclination measurement

Test series were set up when offset files had been created for all cases to be examined. The settings used for these computations were the same as for the reference hull to be able to compare the results with as high accuracy as possible. That means that the computations were run using a zonal approach, nonlinear potential flow computations with free sinkage and trim and RANS computations for the stern part using 3000 iterations.

6.3.1 Viscous resistance

Viscous resistance is broken down into two parts, the frictional resistance and the viscous pressure resistance. The components are first compared individually and the total viscous resistance is presented in Figure 6.5.

The frictional resistance coefficient, C_F, does not vary much for the different cases. The average difference over the entire speed range compared to the reference hull and the wetted area (non-dimensionalised by LPP) can be seen in Table 6.1 and the values of C_F can be seen in Figure 6.3.

CFD Case	Average difference of C_F	Wetted area (S/LPP^2)
Stern + 4 Degrees	0.79 %	0.300
Stern + 2 Degrees	0.43 %	0.299
Reference	*0 %*	*0.298*
Stern - 2 Degrees	-0.34 %	0.296
Stern - 4 Degrees	-0.80 %	0.294

Table 6.1: Average difference of CF

The frictional resistance coefficient gets larger for increasing wetted area, just as can be seen in Figure 6.3. There is however a slight bump in the figure at 11 knots that cannot be explained by increasing wetted area. This bump seems to increase when the stern is made steeper. When the stern angle is four degrees less than the reference hull the curve is almost straight. This bump behavior does not occur in the model tests however, so this is likely an inaccuracy in the CFD software.

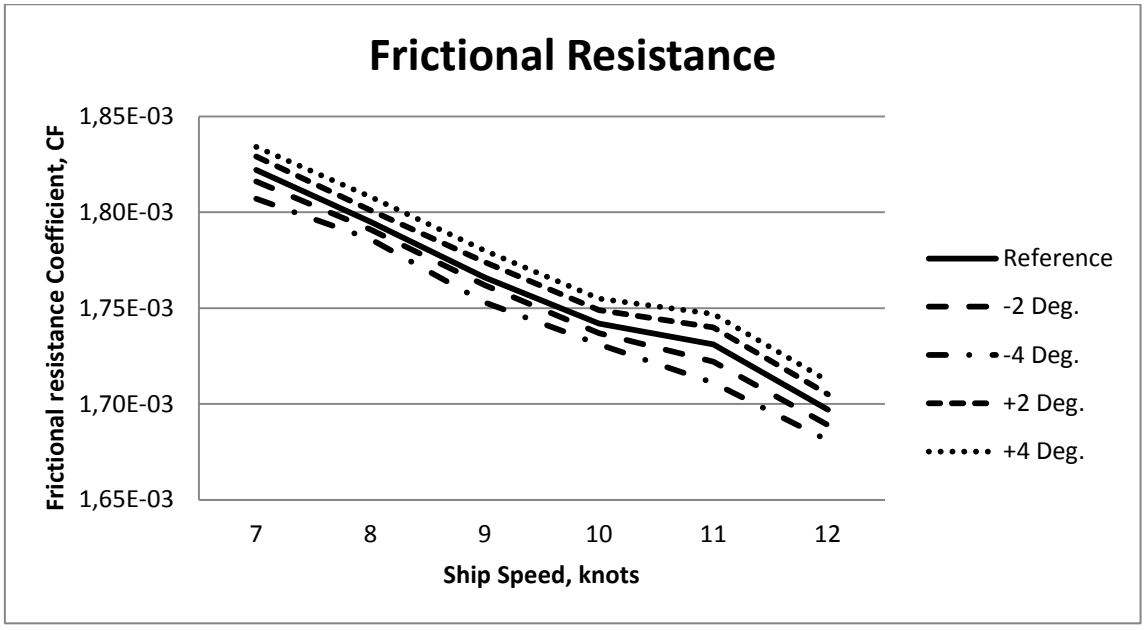

Figure 6.3: Frictional resistance coefficient

Pressure resistance is also broken down into two parts, Wave resistance and viscous pressure resistance. Viscous pressure resistance is the part of the pressure resistance that does not result in waves. Instead it consists of viscous effects like the buildup of pressure on the stern of the ship.

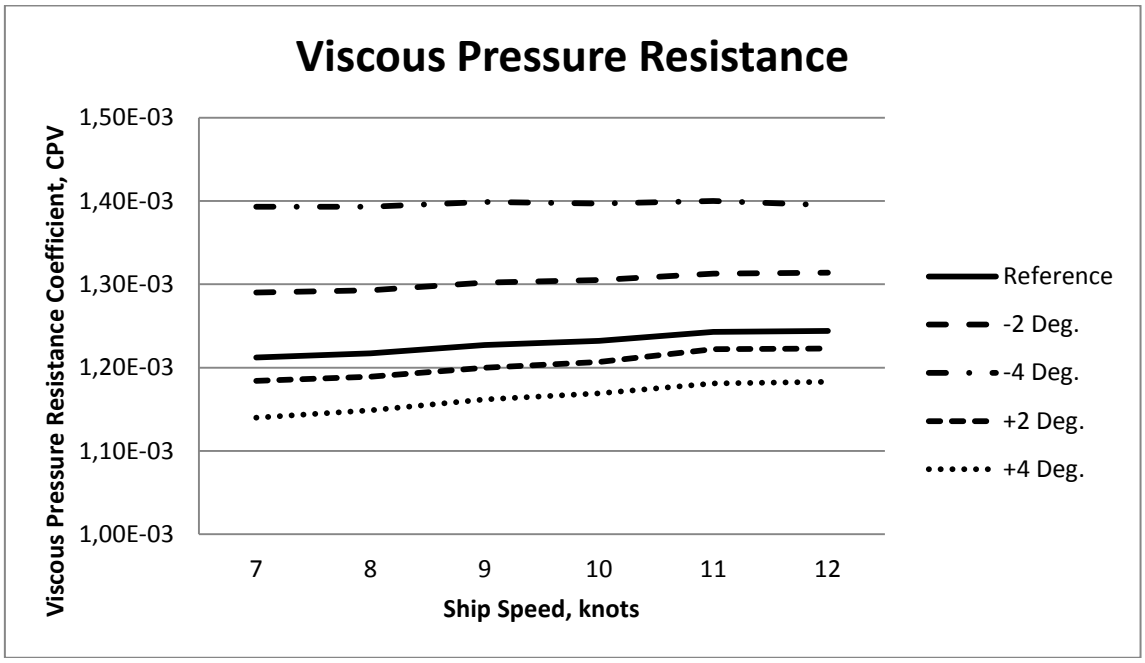

Figure 6.4: Viscous pressure resistance coefficient

As can be seen in Figure 6.4 the viscous pressure increases for decreasing inclination angle. For increasing angles the susceptibility to ship speed is increasing resulting in higher resistance for higher speeds. At -4 degrees of inclination this behavior has vanished and the resistance is almost constant for the entire speed range. The complete viscous resistance coefficient comprising of frictional and viscous pressure resistance can be seen in Figure 6.5.

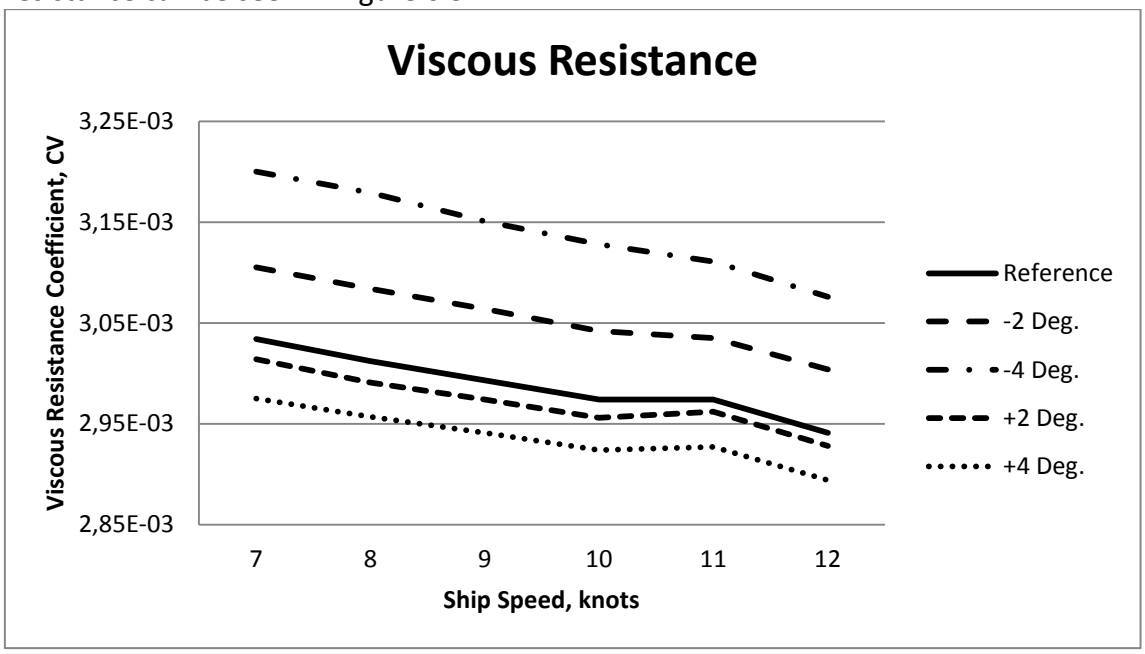

Figure 6.5: Viscous resistance coefficient

6.3.2 Wave resistance

The computed wave resistance is based on transverse wave cut method due to the submerged transom, as previously mentioned in chapter 5.5.2.1. The results of the computations can be seen in Figure 6.6.

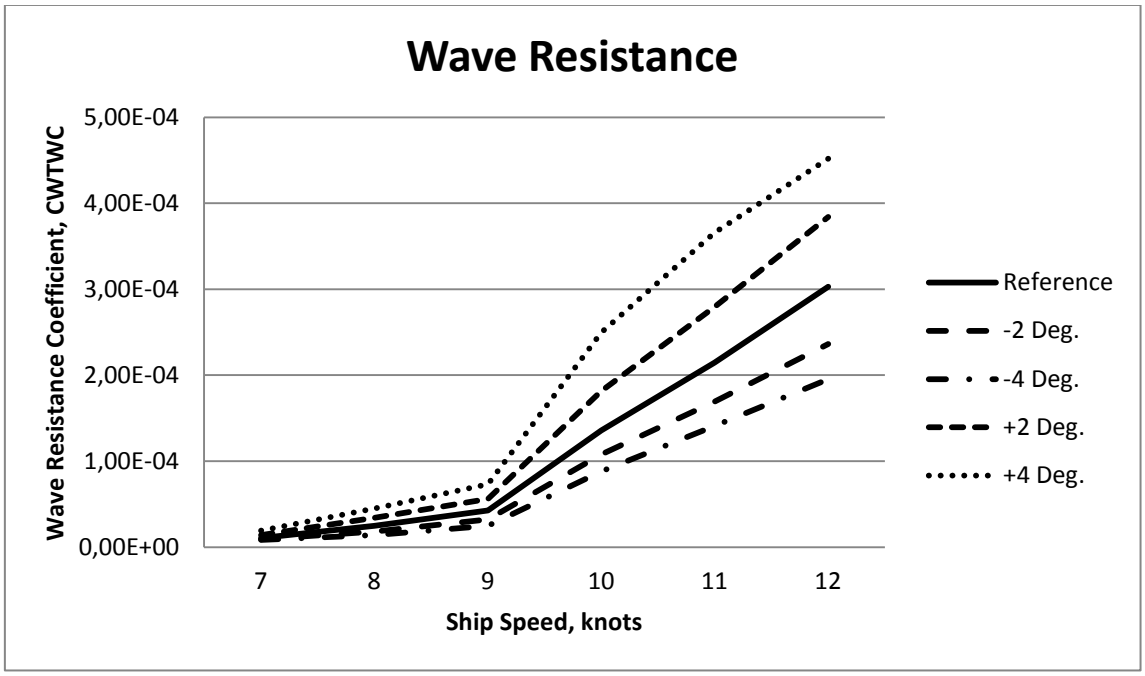

Figure 6.6: Wave resistance coefficient

As one might expect the wave resistance stays reasonable low for all the investigated hulls at low speeds. At around 9 knots this drastically changes and the wave resistance increases rapidly thereafter. The relation of the wave resistance between the modified hulls and the reference hull can be seen in Table 6.2.

CFD Case	Average difference of C_{WTWC}	Standard deviation
Stern + 4 Degrees	72.35%	12.62%
Stern + 2 Degrees	31.37%	3.66%
Stern - 2 Degrees	-21.62%	4.44%
Stern - 4 Degrees	-35.60%	7.27%

Table 6.2: Wave resistance coefficient compared to reference hull

From Table 6.2 it is clear that the inclination angle affect the wave resistance more than any other quantity examined. A four degree increase of the angle will raise the wave resistance with around 72 %.

Figure 6.7 to Figure 6.11 show the wave pattern for all the investigated hulls. The drop in wave resistance for decreasing angle can be seen in the figures by checking the wave pattern emitting from the stern. This pattern gets clearer the more the angle increases indicating larger wave peaks/troughs. Thus the smallest waves emitting from the stern can be found in Figure 6.7 where the inclination angle is smallest.

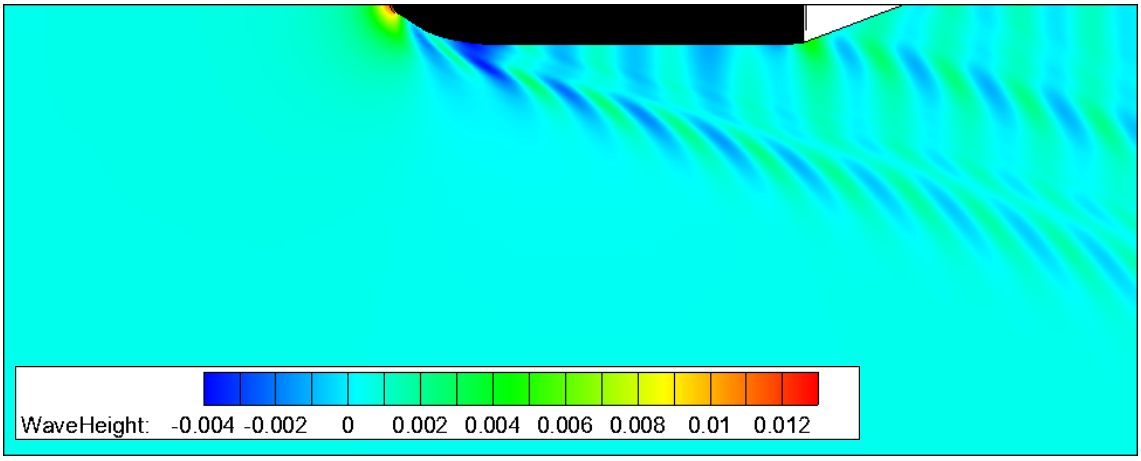

Figure 6.7: Wave pattern at 10 kn, -4 degrees inclination

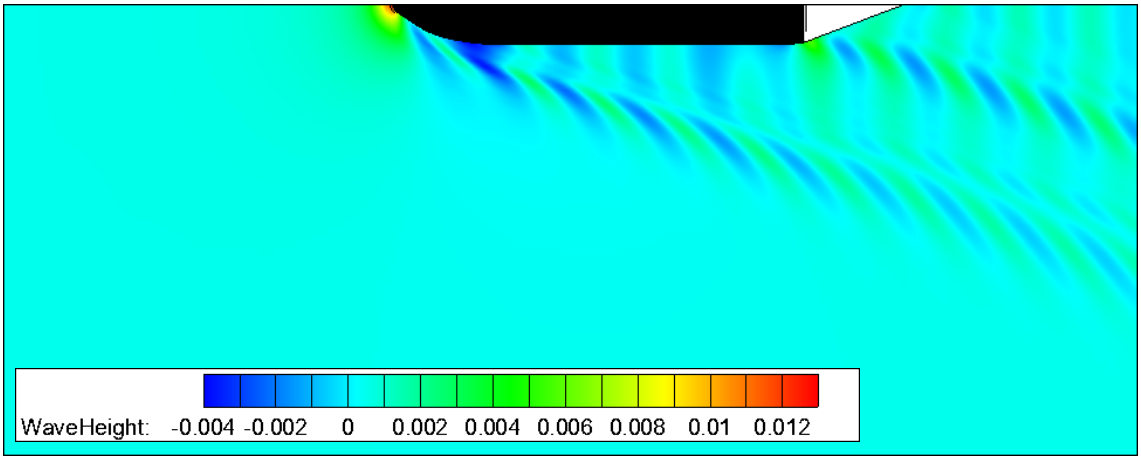

Figure 6.8: Wave pattern at 10 kn, -2 degrees inclination

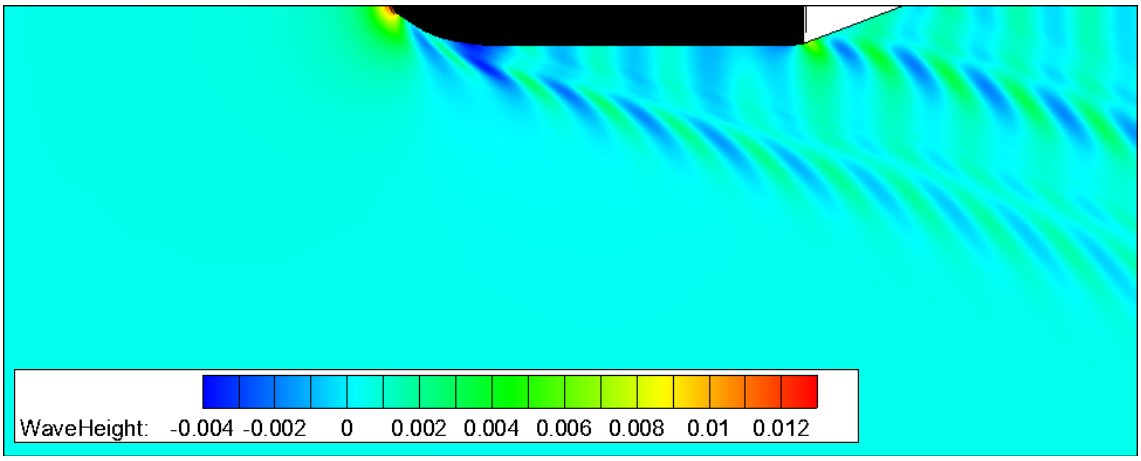

Figure 6.9: Wave pattern at 10 kn, Reference hull

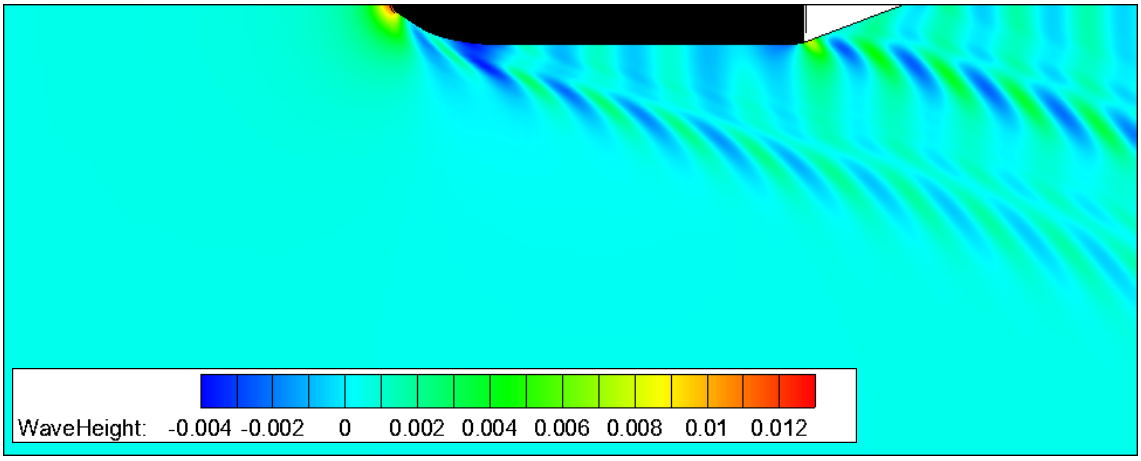

Figure 6.10: Wave pattern at 10 kn, +2 degrees of inclination

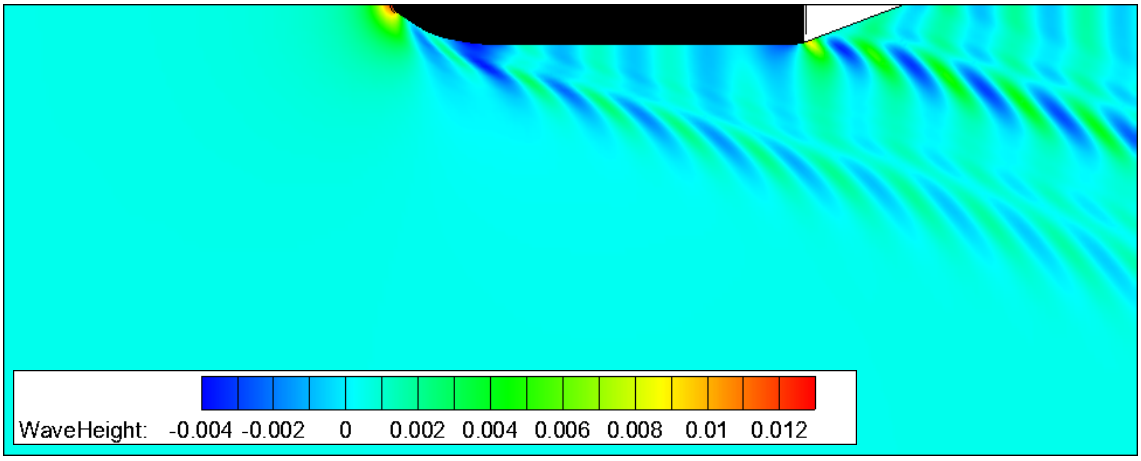

Figure 6.11: Wave pattern at 10 kn, +4 degrees of inclination

6.3.3 Total resistance

Combining the viscous resistance and the wave resistance yields the total resistance. The total resistance can be seen in Figure 6.12 and shows some interesting behavior. For the investigated type of vessel the specified service speed is 10 knots. For this speed the reference hull has the least resistance of all investigated cases but this advantage is only valid in the speed interval from 9 to 12 knots. At speeds higher than 12 knots less inclination is favorable and at speed lower than 9 knots a steeper inclination is advantageous.

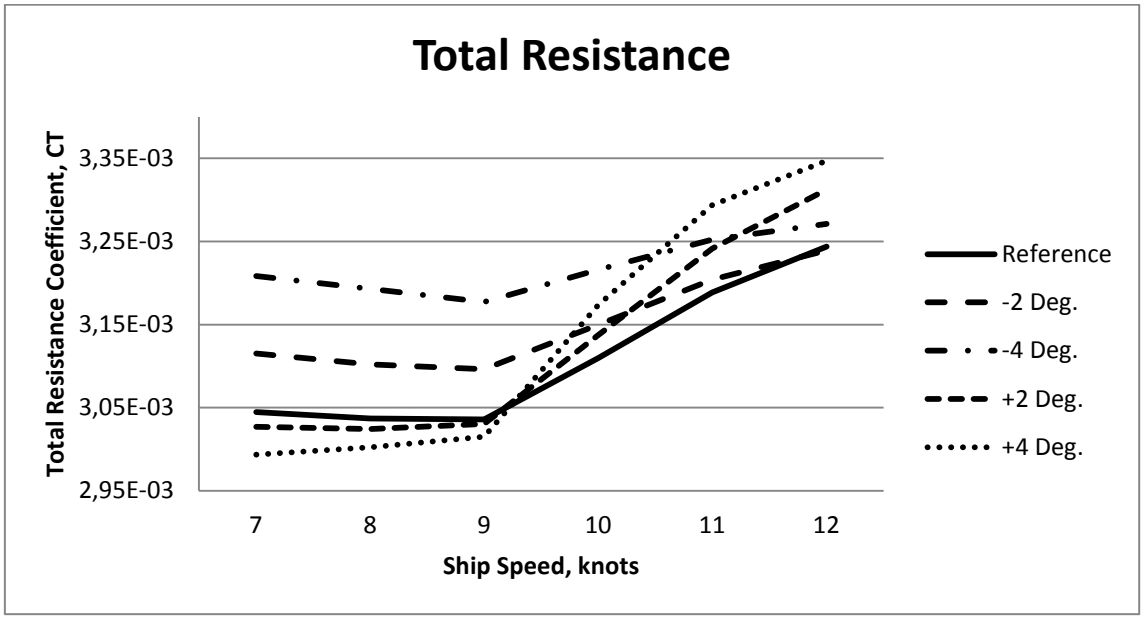

Figure 6.12: Total resistance coefficient

In Table 6.3 the total resistance is displayed as the effective power required for propelling the ship.

Effective Power [kW]					
Speed	**-4 Degrees**	**-2 Degrees**	**Reference**	**+2 Degrees**	**+4 Degrees**
7	179	173	169	168	167
8	266	258	253	252	250
9	376	366	359	358	357
10	522	511	505	509	515
11	703	693	690	701	712
12	917	909	910	929	939

Table 6.3: Effective power

6.3.4 Change of trim and displacement

Figure 6.13 shows how the trim of the ship changes when the stern angle is changed. When comparing this figure to Figure 5.31 it turns out that the case where the stern angle is changed +4 degrees matches the model test better than the reference case. A more credible representation would therefore be to shift all results in Figure 6.13 to make the reference case match the model tests. The results in Figure 6.13 can be used for comparison purposes without paying too much attention to the specified values.

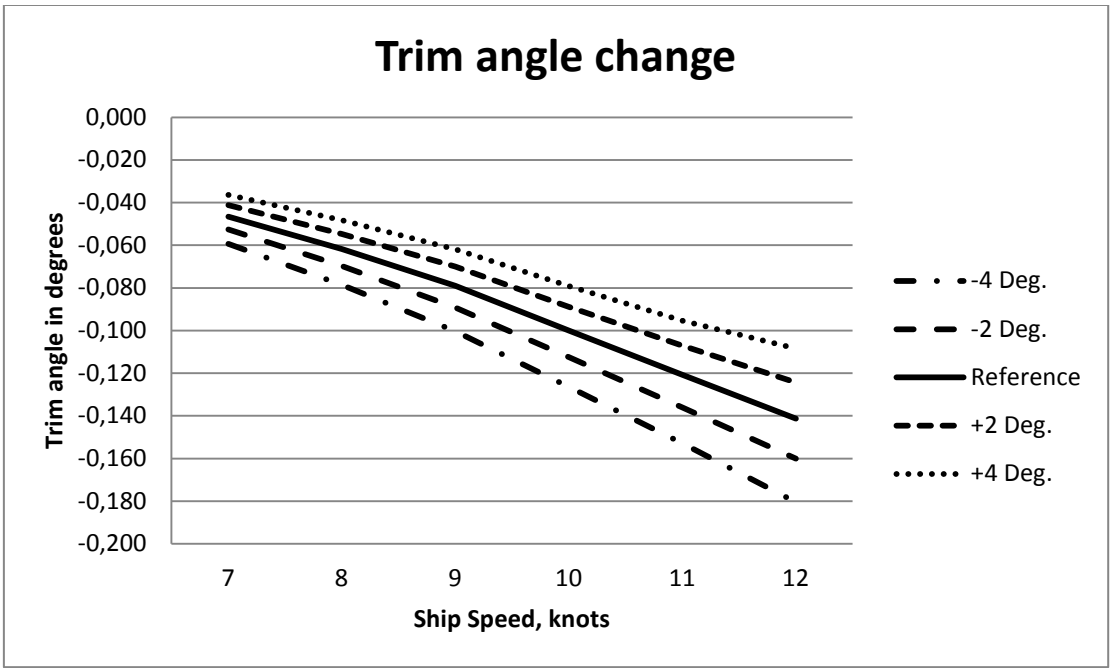

Figure 6.13: Change of trim for different stern inclination

Since the ship length is held constant for the entire investigation there will be a change in displacement when the stern angle is changed. How much the displacement is changed can be viewed in Table 4.1. The specified displacement for the ship is 6806 m^3 while the CFD model for the reference case is 6 804 m^3. That is a difference of around 0.03 % which must be considered to be a very good representation of the real ship.

Displacement change for different inclination angle [m3]					
	-4 Degrees	**-2 Degrees**	**Reference**	**+2 Degrees**	**+4 Degrees**
Total	6 570	6 707	6 804	6 877	6 933
Difference	-235	-97	0	72	129

Table 6.4: Displacement change when changing inclination angle

7 Results and Discussion

The results from double model computations run on the ballast condition were presented in chapter 5.2.1. Even though Mesh 4 did not result in the lowest CXPI-value it was chosen as the final mesh due to the look of the panelization on the hull. It could be assumed that the CXPI-value does not have too much impact on the final results in for example the potential flow computations since these are run with a non-linear surface and CXPI-value is computed using a linear method. This could in that case be confirmed by Figure 5.19 where the results from potential flow computations were almost exactly the same for Mesh 4 and Mesh 3 even though there was quite a big difference between the CXPI-values from the double model computations.

For the loaded condition Mesh 1 in Figure 5.6 was chosen. Using a finer mesh for the hull would raise the computational memory requirement. Since the memory is shared by the Hull and Free surface a finer hull mesh would result in a lowering the resolution for the free surface. The CXPI-value did not affect the computational results much, as stated above. Therefore it was better to have a low resolution hull mesh and high resolution free surface.

From the grid uncertainty analysis it was found that the uncertainty varied from around -15 % to 20 % for the grid used in the investigation, Grid 3. This may seem as a rather high uncertainty. As described in chapter 5.3 the curve fitting using the LSR was fairly instable and some of the resulting curve fittings were very poor which may be a reason for the high uncertainty. Due to the poor curve fittings to the computed scatter these results are considered quite unreliable.

As mentioned in chapter 5.4 two different extrapolation methods were applied on the model test results but only one of them, the MARIN Form Factor Method, was used for the verification of the CFD-results. However, the results from both methods were compared and Figure 7.1 shows a diagram of the total effective power for loaded condition.

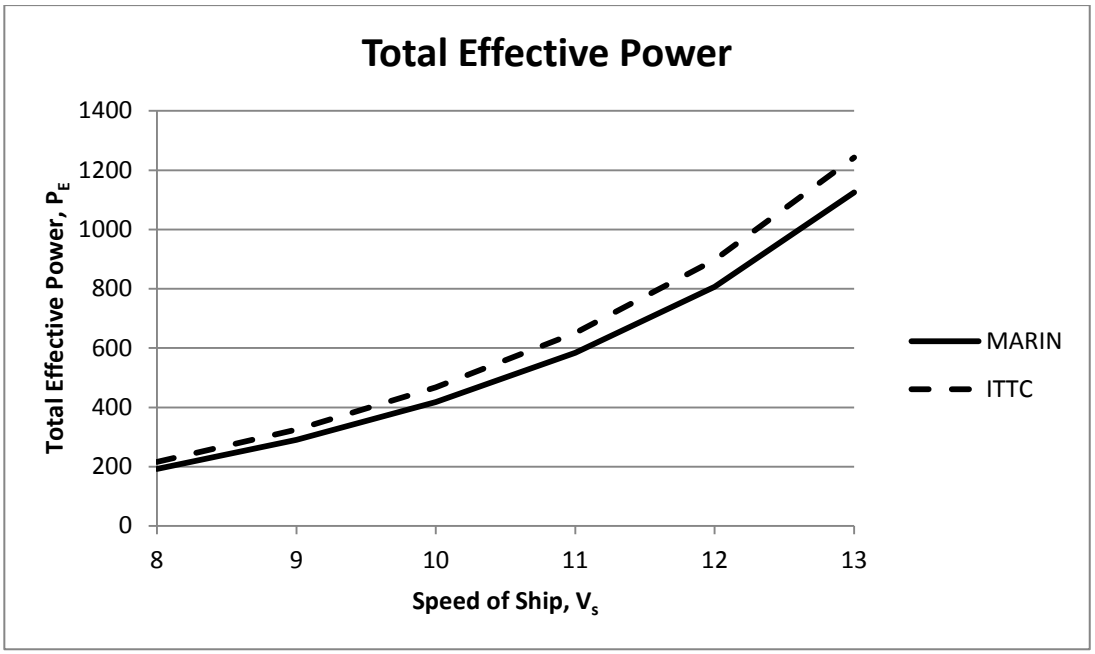

Figure 7.1: Extrapolated total effective power, loaded condition

The diagram shows that the total effective power will be slightly higher when using the ITTC method. This is probably due to that the hull roughness is included in the ITTC method but in the MARIN method it is not. When including hull roughness the resistance of the ship will be higher which will result in a higher total effective power.

In chapter 5.5.1.1 it was realized that the values of the longitudinal centre of buoyancy and the block coefficient in SHIPFLOW were incorrect for the ballast condition. The reason why the block coefficient differed is because in SHIPFLOW it is not based on the mean draft as it is in the model test. Instead the block coefficient is based on some other draft which is just specified as “draft” in the output-file in SHIPFLOW. The value of this draft for the different speeds is close to the value of the draft at aft perpendicular but slightly lower. In Figure 7.2 all drafts received from the ouput-files in SHIPFLOW are plotted. It is seen that the draft that is used to calculate the block coefficient, “Draft CB”, does not match the aft draft or any of the drafts.

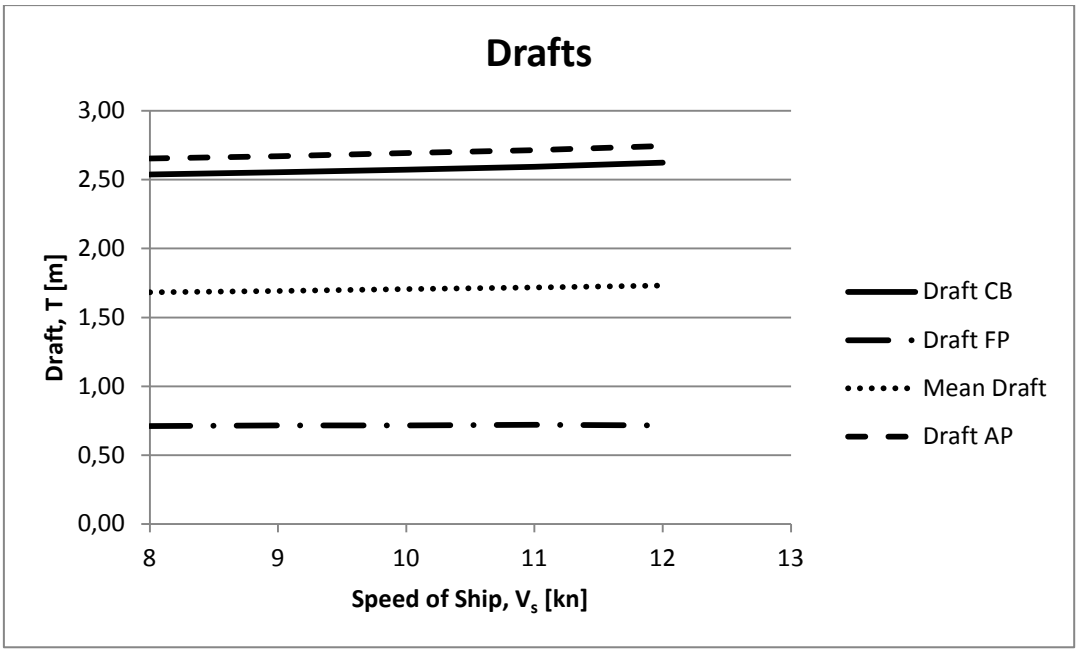

Figure 7.2: Dynamic drafts from SHIPFLOW

If recalculating the block coefficient with the dynamic mean draft instead we then get values close to the values from the model test. Figure 7.3 shows a plot of the incorrect block coefficients received from the computations in SHIPFLOW, “SHIPFLOW”, the block coefficients taken from the model test including propellers, “Model (prop)”, and the re-calculated values using the dynamic mean draft from SHIPFLOW, “Dynamic draft”. The values are also listed in Appendix K. The difference between the real block coefficient and the block coefficient that SHIPFLOW uses in the computation is too big to “see through” and therefore it was no use in continuing with the analysis on ballast condition.

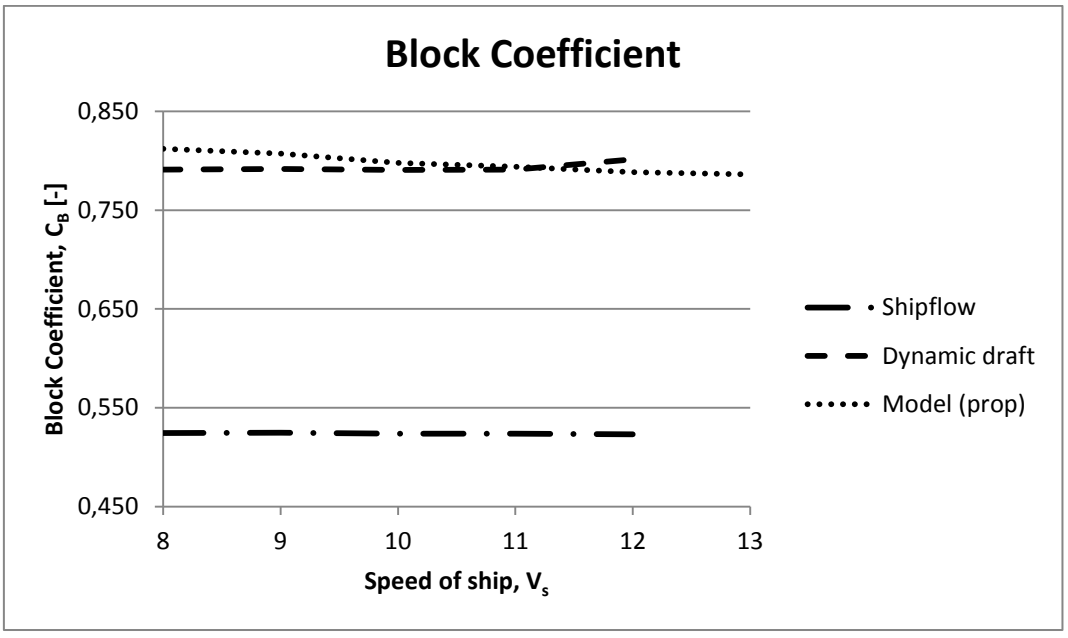

Figure 7.3: Block coefficients from SHIPFLOW and resistance tests

All series of potential flow computations in chapter 5.5.1.1 resulted in a distinct step between 9 and 10 knots. The reason why the wave resistance curve results in this manner is not known. One assumption could be that there is interference between the bow and stern wave at this which creates a hump in the wave resistance curve. However, this seems most unlikely since then it would occur in the model test as well. The answer to that would then be that SHIPFLOW makes the computations with different values of the longitudinal centre of buoyancy and the block coefficient creating a different condition than at the model test. If looking at Figure 5.20, where more speeds in the speed range were included, it is looking more like a step in the curve than a hump. The wave resistance at 11 knots is as high as it is at 10 knots. A more likely explanation might simply be due to some computational error.

The computations on the loaded reference hull proved to match the model tests within reasonable limits. The total resistance coefficient in Figure 5.30 shows that the computed resistance is around 13 % lower than the model test results. This difference is expected due to the simplifications made in the CFD model where neither the hull joint nor the bow thruster is included. The longitudinal joint of the hull halves is expected to add a significant resistance which make the 13 % difference seem reasonable. The computational curve seem to follow the model test curve well for the entire speed range though it seems like the CFD solution captures the behaviour at low speeds better than at high speeds.

The same behaviour occurs when comparing the trim angle and draught of the computations to the model tests as shown in Figure 5.31 and Figure 5.32. The difference between CFD computations and model test results increase for increasing speed. This difference may be explained by the fact that these model tests were performed using a self-propelled model. No trim/draught model tests were available for the barge without thrusters. When considering this difference the CFD computations capture the behaviour well enough.

In the investigation of different stern inclination some interesting results were found. The small change in frictional resistance coefficient for the different angles shown in Figure 6.3 can be explained by the change of wetted area that results from changing the inclination. A steeper inclination will give a higher wetted area and therefore a higher frictional resistance. The bump for steeper inclinations in Figure 6.3 is not found in the model test results and is considered to be a CFD software irregularity.

The wave resistance gets larger for steeper inclination angles just as might be expected. The interesting result from this analysis regarding the wave resistance is the transition point at around 9 knots where the wave resistance greatly increases with increasing speed. For ship speeds below 9 knots the wave resistance is very small regardless of the inclination angle. In Figure 6.7 to Figure 6.11 the wave patterns at 10 knots for all investigated inclination angles are shown and the stern diverging wave is the only wave affected by the stern inclination angle according to these wave patterns.

When all these components are summed together into the total resistance some interesting trends can be traced, see Figure 6.12. Steep inclination angles are favoured for low speeds due to the fact that wave resistance remains at a very low level up to around 9 knots. The more the speed is increased beyond 9 knots, the more favourable lesser inclination angles get. Another result from Figure 6.12 is that for the speed range 9 to 12 knots the reference hull seems to have the lowest resistance of all the investigated hulls.

The trim angle change in Figure 6.13 displays that the ship will trim less for steeper inclination angles. This is expected since the reference hull has a negative trim and steeper inclinations will put more displacement in the aft of the ship which make the ship trim less.

Perhaps the most interesting result of the investigation is when the total resistance is converted to effective power and compared to the change in displacement as in Table 7.1.

Effective Power and Displacement Difference					
	-4	**-2**	**Reference**	**+2**	**+4**
Displacement Difference [m3]	-235	-97	0	72	129
7 knots	5.6 %	2.3 %	0 %	-0.6 %	-1.2 %
8 knots	4.9 %	1.9 %	0 %	-0.4 %	-1.2 %
9 knots	4.5 %	1.9 %	0 %	-0.3 %	-0.6 %
10 knots	3.3 %	1.2 %	0 %	0.8 %	1.9 %
11 knots	1.8 %	0.4 %	0 %	1.6 %	3.1 %
12 knots	0.8 %	-0.1 %	0 %	2.0 %	3.1 %

Table 7.1: Effective power and displacement difference

Even though the reference hull has the lowest resistance for the design speed it might be interesting to consider a steeper inclination angle. Ships with four degrees steeper inclination angle will increase the displacement with 129 m^3 while only require 1.9% more power to propel, according to the computations. Another way to look at the results would be to lower the design speed to 9 knots. Then a four degree steeper inclination angle than the reference ship will actually lower the required effective power with 0.6%.

7.1 Sources of error

One source of error might be the split over the full length of the barge which is not included in the CFD computations for this analysis but on the model used in the model test it is. The model also included one bow thruster opening and one overflow opening that were not included in the CFD computations.

There could be sources of errors when the model test is run which will have influence on the final results from the model test. There could also be sources of error in the extrapolation method which will have influence on the full scale results from the model test. As was shown in chapter 7 the full scale results can be different depending on which extrapolation method that is chosen.

Different assumptions that have been taken during the analysis might lead to errors in the results.

Sources of errors that could be the cause in differences between the CFD results and the model test results could be that the meshes were to coarse, the panels per wave length were to low or that the size of the free surface mesh was too small.

For the ballast condition a bug in SHIPFLOW turned out to be a source of error in the analysis.

8 Conclusions

The final conclusion when it comes to the ballast condition is simply that this case with the large trim could not be handled by SHIPFLOW. Maybe if finer meshes would have been used, if the number of panels per wavelength would be increased and if the size of the free surface mesh would have been increased we would have received more accurate values for this case. However, the biggest issues are the incorrect values of the longitudinal centre of buoyancy and the block coefficient due to the bug in SHIPFLOW for large trim angles.

8.1 Future Work

For future work it would be interesting to run computations on the ballast condition in any other CFD-software who might be able to handle the trim so that it could be included in the analysis. It would also be interesting to try and solve the problem as recommended by Leif Broberg at FLOWTECH, by rotating data in the offset-file externally.

Due to time constraints curved and S-shaped stern bodies were not included in this analyse. For future work it is recommended to analyse these shapes as well.

It would be of interest to perform CFD-computations on the dredger with propellers included. It is also of interest to go further in the analysis and investigate the stern flow. This thesis has only compared the differences in resistance and power between the different inclination angles. For future work the stern flows should be visualized and compared and try to find the optimum shape of the stern.

References

Bathfield, N. (2011, may 2). E-mail.

Bathfield, N. (2011, may 13). E-mail.

Bertram, V. (2000). *Practical Ship Hydrodynamics.* Oxford: Butterworth-Heinemann.

Broberg, L. (2011, june 22). E-mail.

Eça, L., & Hoekstra, M. (2006). *Discretization Uncertainty Estimation based on Least Squares version of the Grid Convergency Index.* Lisbon: 2nd Workshop on CFD Uncertainty Analysis.

Flowtech Int. (2010). *SHIPFLOW Theoretical Manual.* Gothenburg: FLOWTECH International AB.

Flowtech Int. (2010). *SHIPFLOW User Manual.* Gothenburg: FLOWTECH International AB.

Framework, F. (2011). *Friendship Framework*. Retrieved August 5th, 2011, from http://www.friendship-systems.com/products/friendship-framework/friendship-framework

International Towing Tank Conference. (2011, july 29). *General Information*. Retrieved from International Towing Tank Conference webbpage: http://ittc.sname.org/introduction.htm

International Towing Tank Conference. (2006). Recommended Procedures and Guidelines. *Density and Viscosity of Water* .

International Towing Tank Conference. (2008). Recommended Procedures and Guidelines. *Testing and Data Analysis Resistance Test* .

International Towing Tank Conference. (2008). Recommended Procedures and Guidelines. *Guidelines for Uncertainty Analysis in Resistance Towing Tank Tests* .

ITTC. (2011, july 29). *General Information*. Retrieved from International Towing Tank Conference webbpage: http://ittc.sname.org/introduction.htm

ITTC. (2006). Recommended Procedures and Guidelines. *Density and Viscosity of Water* .

ITTC. (2008). Recommended Procedures and Guidelines. *Testing and Data Analysis Resistance Test* .

ITTC. (2008). Recommended Procedures and Guidelines. *Guidelines for Uncertainty Analysis in Resistance Towing Tank Tests* .

Larsson, L., & Raven, H. (2004). *Ship Resistance and Flow.* Gothenburg and Wageningen: Chalmers University of Technology.

Roache, P. J. (1998). *Verification and Validation in Computational Science and Engineering.* Albuquerque: Hermosa Publishers.

SSPA. (2009). *1978 ITTC Performance Prediction Method.*

Veldhuis, C. (2011, may 2). E-mail.

Veldhuis, C. H., & Pouw, C. P. (2008). *CFD Hull Form Optimization and Calm Water Model Tests for a Self Propelled Split Barge.* Wageningen: MARIN.

Vesting, F. (2011, june 21). E-mail.

Vesting, F. (2011, june 21). E-mail.

White, F. (2008). *Fluid Mechanics, 6th Edition.* New York: McGraw-Hill.

Zou, L., Larsson, L., & Orych, M. (2010). *Verification and validation of CFD predictions for a manoeuvring tanker.* Shanghai: 9th International Conference on Hydrodynamics.

Appendices

A. Model Test Results

Loaded Condition									
V_S [kn]	V_M [m/s]	R_M [N]	Fn	Rn_m	R_{FM} [N]	R_M/R_{FM}	C_{TM} $*10^{-5}$	C_F $*10^{-5}$	Fn^4/C_{FM}
7.01	1.084	46.78	0.118	7.83E+06	34.99	1.337	419	313	0.062
8.00	1.237	60.59	0.135	8.94E+06	44.52	1.361	416	306	0.108
9.00	1.392	77.01	0.152	1.01E+07	55.21	1.395	418	300	0.177
10.00	1.547	95.32	0.169	1.12E+07	66.99	1.423	419	294	0.275
11.01	1.702	118.30	0.186	1.23E+07	79.76	1.483	429	290	0.410
12.00	1.857	148.90	0.202	1.34E+07	93.48	1.593	454	285	0.588

Ballast Condition									
V_S [kn]	V_M [m/s]	R_M [N]	Fn	Rn_m	R_{FM} [N]	R_M/R_{FM}	C_{TM} $*10^{-5}$	C_F $*10^{-5}$	Fn^4/C_{FM}
8.00	1.237	37.34	0.139	8.43E+06	31.89	1.171	362	309	0.120
9.00	1.392	48.12	0.156	9.49E+06	39.55	1.217	368	303	0.197
10.01	1.548	60.20	0.174	1.05E+07	47.98	1.255	373	297	0.306
11.00	1.701	74.69	0.191	1.16E+07	57.05	1.309	383	292	0.455
12.01	1.857	92.03	0.208	1.27E+07	66.95	1.375	396	288	0.655
13.00	2.010	113.15	0.226	1.37E+07	77.42	1.462	415	284	0.912

B. Mesh Settings, Ballast Condition

MESH 1											
	Point				Station				str2/4	df2/4	dl2/4
Setting no.	1	2	3	4	1	2	3	4			
Hull	28	40	56	79	80	113	160	226	1	0.004	0.008
Stern	27	38	54	76	36	51	72	102	1	0.008	-
Bulb	20	28	40	57	18	25	36	51	-	-	-
Skeg	10	14	20	28	36	51	72	102	1	-	0.0035
FlatSkeg	4	6	8	11	36	51	72	102	-	-	-

MESH 2									
	Point			Station			str2/4	df2/4	dl2/4
Setting no.	1	2	3	1	2	3			
Hull	32	45	64	100	141	200	1	0.003	0.006
Stern	30	42	60	46	65	92	1	0.009	-
Bulb	22	31	44	28	40	56	-	-	-
Skeg	12	17	24	46	65	92	1	-	0.002
FlatSkeg	6	8	12	46	65	92	-	-	-

MESH 3									
	Point			Station			str2/4	df2/4	dl2/4
Setting no.	**1**	**2**	**3**	**1**	**2**	**3**			
Hull	32	45	64	110	156	220	1	0.0015	-
Stern	30	42	60	46	65	92	-	-	-
Bulb	22	31	44	28	40	56	-	-	-
Skeg	12	17	24	46	65	92	1	-	0.002
FlatSkeg	6	8	12	46	65	92	-	-	-

MESH 4											
	Point				Station				str2/4	df2/4	dl2/4
Setting no.	**1**	**2**	**3**	**4**	**1**	**2**	**3**	4			
Hull	28	40	56	79	100	141	200	283	1	0.004	0.01
Stern	27	38	54	76	36	51	72	102	1	-	0.00525
Bulb	30	42	60	85	22	31	44	62	-	-	-
Skeg	10	14	20	28	36	51	72	102	1	-	0.0035
FlatSkeg	3	4	6	8	36	51	72	102	-	-	-

C. Extrapolated Model Test Results, MARIN Form Factor Method

Loaded Condition								
V_S [kn]	V_M [m/s]	C_{RES} $*10^{-5}$	C_{FS} $*10^{-5}$	C_{TS} $*10^{-5}$	F_D [N]	R_S [kN]	P_E [kW]	C_E
7.0	1.083	12	180	345	8.19	53.4	192	479
8.0	1.237	19	177	349	9.92	70.4	290	475
9.0	1.392	28	174	354	11.72	90.4	418	468
10.0	1.547	37	171	359	13.58	113	584	460
11.0	1.701	53	169	374	15.48	143	807	443
12.0	1.856	83	167	401	17.43	182	1125	413

Ballast Condition								
V_S [kn]	V_M [m/s]	C_{RES} $*10^{-5}$	C_{FS} $*10^{-5}$	C_{TS} $*10^{-5}$	F_D [N]	R_S [kN]	P_E [kW]	C_E
8.00	1.237	-9	178	325	3.85	46.5	191	335
9.00	1.392	4	175	334	4.32	60.5	280	325
10.01	1.547	17	173	344	4.74	77.0	396	316
11.00	1.701	32	171	356	5.11	96.4	546	305
12.01	1.856	51	169	373	5.41	120	742	291
13.00	2.010	74	167	395	5.65	149	998	275

D. Extrapolated Model Test Results, ITTC-78 Method

Loaded Condition						
V_S [kn]	V_M [m/s]	C_R $*10^{-5}$	C_{FS} $*10^{-5}$	C_{TS} $*10^{-5}$	R_S [kN]	P_E [kW]
7.00	1.083	12.0	180	387	59.9	216
8.00	1.237	19.5	177	390	78.9	325
9.00	1.392	27.9	174	395	101.1	468
10.00	1.547	37.0	171	401	126.6	651
11.00	1.701	53.8	169	415	158.6	897
12.00	1.856	83.9	167	443	201.3	1243

Ballast Condition						
V_S [kn]	V_M [m/s]	C_R $*10^{-5}$	C_{FS} $*10^{-5}$	C_{TS} $*10^{-5}$	R_S [kN]	P_E [kW]
8.00	1.237	-8.7	178	386	55.3	228
9.00	1.392	5.5	175	397	72.0	333
10.01	1.547	17.0	173	406	90.8	467
11.00	1.701	32.3	171	419	113.3	641
12.01	1.856	51.0	169	435	140.1	865
13.00	2.010	74.6	167	456	172.6	1154

E. FLOWTECH Recommended Free Surface Panelization

Ballast Condition						
	8 knots	**9 knots**	**10 knots**	**11 knots**	**12 knots**	**13 knots**
Point	68	65	63	61	60	58
df1	0.0106	0.0112	0.0119	0.0126	0.0133	0.0140
Stau	91	71	61	50	45	38
Dlu	0.0076	0.0097	0.0112	0.0137	0.0154	0.0182
Stam	132	104	90	74	66	56
Stad	67	56	52	45	43	39
Dfd	0.0076	0.0097	0.0112	0.0137	0.0154	0.0182
Xups	-1	-1	-1	-1	-1	-1
Xste	1	1	1	1	1	1
Xdow	1.6818	1.7301	1.7841	1.8437	1.9090	1.9801
y4side	-1.0811	-1.1121	-1.1468	-1.1852	-1.2272	-1.2728

F. Wave Resistance Coefficients, Ballast Condition

	Wave Resistance Coefficient, C_W [-]				
V_s [kn]	Series 1	Series 2	Series 3	Series 4	Series 5
8.00	4.34E-04	3.53E-04	3.48E-04	3.44E-04	3.37E-04
9.00	4.94E-04	3.98E-04	3.81E-04	3.97E-04	3.84E-04
10.00	7.95E-04	7.02E-04	7.02E-04	7.58E-04	7.38E-04
11.00	8.31E-04	7.11E-04	6.96E-04	8.07E-04	7.83E-04
12.00	-	-	9.01E-04	1.04E-03	1.02E-03

	Wave Resistance Coefficient Wave Cut, C_{WTWC} [-]				
V_s [kn]	Series 1	Series 2	Series 3	Series 4	Series 5
8.00	2.02E-04	2.00E-04	1.81E-04	1.87E-04	1.87E-04
9.00	3.04E-04	2.89E-04	2.95E-04	2.99E-04	2.99E-04
10.00	3.42E-04	3.26E-04	3.29E-04	3.48E-04	3.47E-04
11.00	4.42E-04	4.20E-04	4.19E-04	4.46E-04	4.46E-04
12.00	-	-	6.38E-04	6.69E-03	6.69E-03

G. Change of Level Due to Speed, Model Test

PROPULSION TEST No. : 9608106
SHIP MODEL No. : 8776
PROPELLER MODEL No. : 5578 R+L
PROPELLERS ROTATING OUTWARD OVER THE TOP

DRAUGHT FWD : 0.700 m
DRAUGHT AFT : 2.600 m

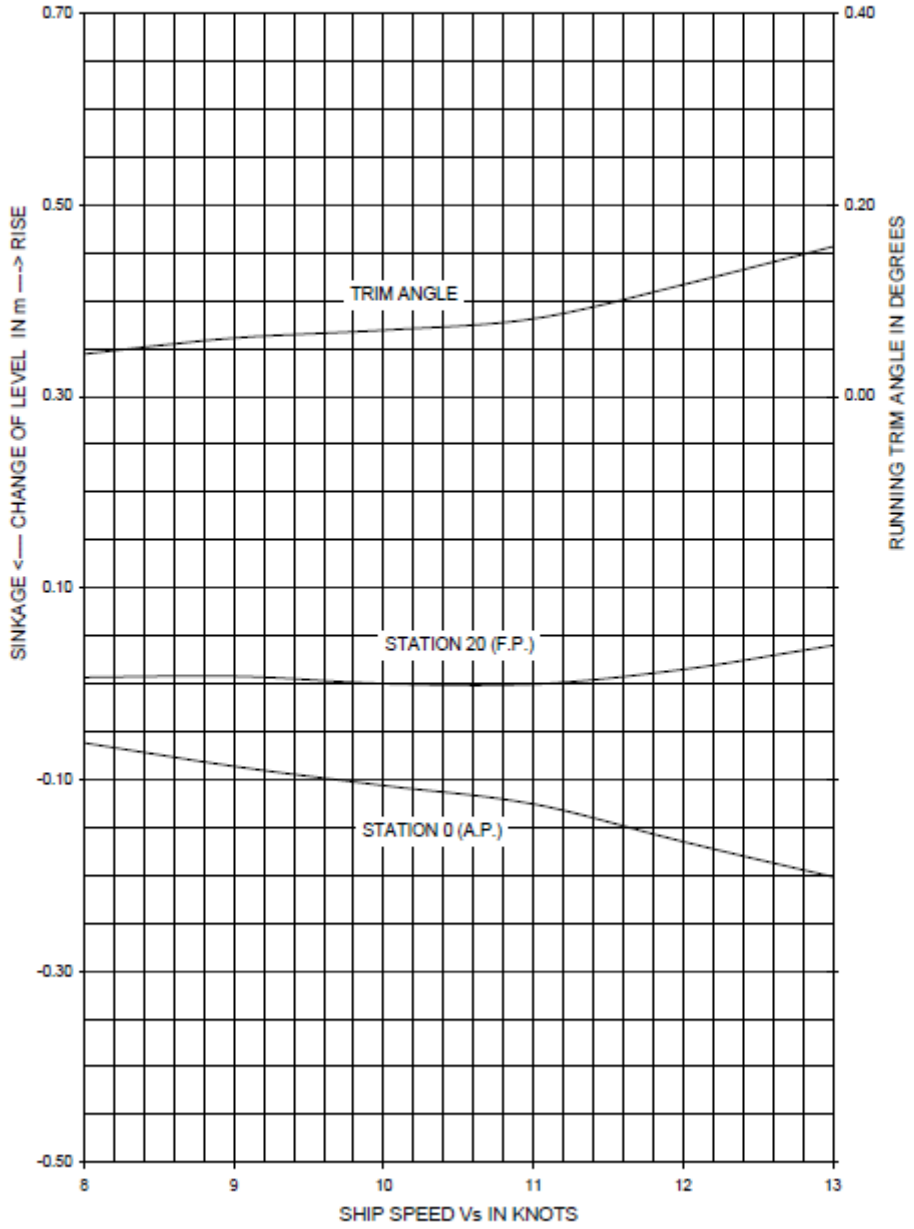

CHANGE OF LEVEL DUE TO SPEED

PROPULSION TEST No. : 9608105
SHIP MODEL No. : 8776
PROPELLER MODEL No. : 5578 R+L
PROPELLERS ROTATING OUTWARD OVER THE TOP

DRAUGHT FWD : 4.800 m
DRAUGHT AFT : 4.800 m

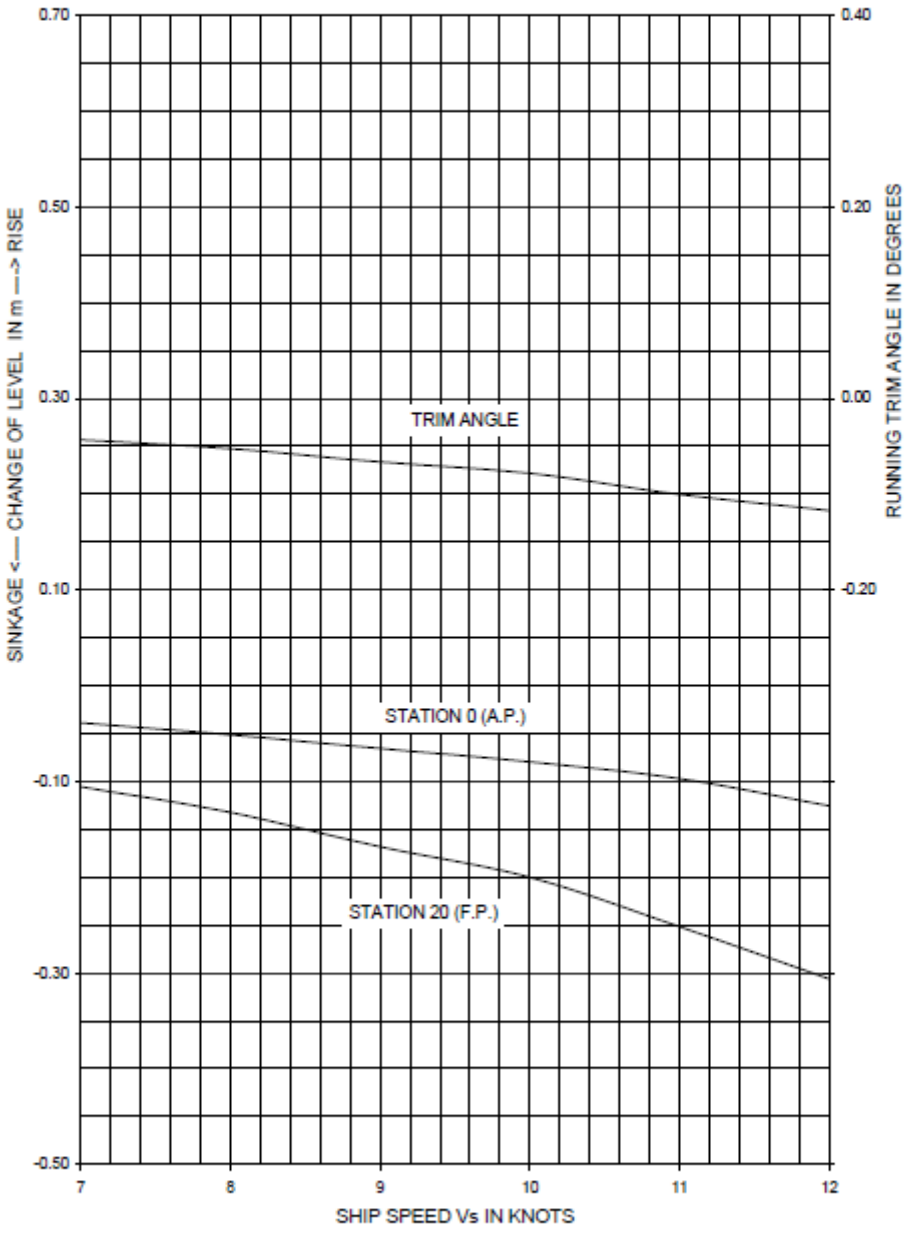

CHANGE OF LEVEL DUE TO SPEED

H. Dynamic Trim Angle and Dynamic Drafts, Ballast Condition

Model Test			
V_s [kn]	Trim angle, θ [°]	Draft AP, T_a [m]	Draft FP, T_f [m]
8.00	1.275	2.660	0.690
9.00	1.290	2.680	0.690
10.00	1.300	2.710	0.700
11.00	1.310	2.725	0.700
12.00	1.350	2.770	0.680
13.00	1.390	2.800	0.660

CFD Computations			
V_s [kn]	Trim angle, θ [°]	Draft AP, T_a [m]	Draft FP, T_f [m]
8.00	1.258	2.654	0.712
9.00	1.265	2.670	0.715
10.00	1.280	2.693	0.716
11.00	1.291	2.714	0.720
12.00	1.314	2.746	0.716

I. RANS-computations Results, Ballast Condition

	Resistance Coefficients			
V_s [kn]	C_F	C_{PV}	C_V	C_T
8.00	1.85E-03	3.64E-04	2.22E-03	2.56E-03
9.00	1.83E-03	3.62E-04	2.19E-03	2.59E-03
10.00	1.80E-03	3.65E-04	2.17E-03	2.93E-03
11.00	1.79E-03	3.66E-04	2.15E-03	2.96E-03
12.00	1.78E-03	3.68E-04	2.14E-03	3.18E-03

J. CFD Results for Modified Hull, Ballast Condition

Wave Resistance Coefficients					
V_s [kn]	8.00	9.00	10.00	11.00	12.00
C_W [-]	3.32E-04	7.54E-04	7.69E-04	-	-
C_{WTWC} [-]	2.23E-04	2.56E-04	4.28E-04		

RANS-computation				
V_s [kn]	C_F	C_{PV}	C_V	C_T
10.00	1.81E-03	3.91E-04	2.20E-03	2.97E-03

K. Block Coefficients, Ballast Condition

	Block Coefficient, C_B [-]		
V_s [kn]	SHIPFLOW (OUTPUT-file)	SHIPFLOW (dynamic T_m)	Model tests (dynamic T_m, prop)
8.00	0.524	0.791	0.812
9.00	0.525	0.792	0.807
10.00	0.524	0.791	0.798
11.00	0.524	0.791	0.794
12.00	0.523	0.801	0.789
13.00	-	-	0.786

L. Results from Uncertainty analysis

Computed forces						
Grid	**Fx_p**	**Fy_p**	**Fx_f**	**Fy_f**	**FX**	**FY**
G5	8.62E-05	-9.84E-04	6.04E-05	1.49E-06	1.47E-04	-9.83E-04
G4	8.46E-05	-9.95E-04	6.08E-05	1.55E-06	1.45E-04	-9.93E-04
G3	8.45E-05	-9.90E-04	6.01E-05	1.56E-06	1.45E-04	-9.88E-04
G2	7.51E-05	-9.96E-04	5.97E-05	1.63E-06	1.35E-04	-9.95E-04
G1	7.43E-05	-9.95E-04	5.87E-05	1.64E-06	1.33E-04	-9.93E-04

Iterative error						
Grid	**Fx_p**	**Fy_p**	**Fx_f**	**Fy_f**	**FX**	**FY**
G5	7.85E-07	2.58E-06	4.36E-09	1.30E-09	7.90E-07	2.58E-06
G4	3.11E-07	7.88E-07	2.50E-09	4.18E-10	3.13E-07	7.89E-07
G3	1.66E-07	4.23E-07	1.60E-09	4.88E-10	1.67E-07	4.23E-07
G2	5.27E-08	1.51E-07	9.08E-10	3.22E-10	5.36E-08	1.51E-07
G1	1.53E-08	4.07E-08	1.29E-09	2.48E-10	1.65E-08	4.10E-08

Discretization error, δ_{RE}						
Grid	**Fx_p**	**Fy_p**	**Fx_f**	**Fy_f**	**FX**	**FY**
G5	-5.39E-06	-3.38E-06	-6.16E-07	1.29E-07	-6.15E-06	-3.32E-06
G4	-7.25E-06	-4.55E-06	-8.29E-07	1.73E-07	-8.27E-06	-4.47E-06
G3	-9.93E-06	-6.23E-06	-1.14E-06	2.37E-07	-1.13E-05	-6.12E-06
G2	-1.35E-05	-8.48E-06	-1.55E-06	3.23E-07	-1.54E-05	-8.33E-06
G1	-1.84E-05	-1.15E-05	-2.10E-06	4.40E-07	-2.10E-05	-1.13E-05

Standard deviation of solution, U_s					
Fx_p	**Fy_p**	**Fx_f**	**Fy_f**	**FX**	**FY**
2.98E-06	5.27E-06	4.19E-07	1.09E-07	2.91E-06	5.25E-06

Computed uncertainty, U_ϕ						
Grid	**Fx_p**	**Fy_p**	**Fx_f**	**Fy_f**	**FX**	**FY**
G5	-6.73E-06	-4.22E-06	-7.70E-07	1.61E-07	-7.68E-06	-4.15E-06
G4	-9.07E-06	-5.69E-06	-1.04E-06	2.17E-07	-1.03E-05	-5.59E-06
G3	-1.24E-05	-7.79E-06	-1.42E-06	2.97E-07	-1.42E-05	-7.65E-06
G2	-1.69E-05	-1.06E-05	-1.93E-06	4.04E-07	-1.93E-05	-1.04E-05
G1	-2.30E-05	-1.44E-05	-2.63E-06	5.50E-07	-2.63E-05	-1.42E-05

M. Script for grid convergence uncertainty analysis

Main script file:

```
%% Input Data
% [ RefinementFactor, No. Cells, hi/h1,
% Fx_p, Fy_p, Fz_p, Fx_f, Fy_f, Fz_f, FX, FY ]
G5 = [ 1                 2932800     1
0.0000862356461538462   -0.000984169576923077   -0.00189867461538461
0.0000603912884615385   1.48845807692308E-06    1.69628230769231E-06
0.000146626934615385    -0.000982681118846154 ];
G4 = [ 1.18920711500272 1876970     1.16040174206451
0.0000845801192307692   -0.000994580192307692   -0.00187030576923077
0.0000607805269230769   1.54701153846154E-06    1.81367884615385E-06
0.000145360646153846    -0.000993033180769231 ];
G3 = [ 1.4142135623731  1171728     1.35774604533099    0.00008449405
-0.000990052846153846   -0.00186902846153846    0.0000601155769230769
1.55901192307692E-06    1.74994269230769E-06    0.000144609626923077
-0.000988493834230769 ];
G2 = [ 1.68179283050743 737673      1.58418605697054
0.0000751278461538461   -0.000996215807692308   -0.00189391346153846
0.0000597436153846154   1.62798153846154E-06    0.000001677465
0.000134871461538462    -0.000994587826153846 ];
G1 = [ 2                 464202      1.84866611156775
0.0000743277846153846   -0.000994600384615385   -0.00190608115384615
0.0000587386653846154   1.63652884615385E-06    1.64148384615385E-06
0.00013306645           -0.000992963855769231 ];

h = [ G5(3) G4(3) G3(3) G2(3) G1(3) ];             % Real Values
(Output)
Fx_p =  [ G5(4)  G4(4)  G3(4)  G2(4)  G1(4) ];
Fy_p =  [ G5(5)  G4(5)  G3(5)  G2(5)  G1(5) ];
Fx_f =  [ G5(7)  G4(7)  G3(7)  G2(7)  G1(7) ];
Fy_f =  [ G5(8)  G4(8)  G3(8)  G2(8)  G1(8) ];
FX =    [ G5(10) G4(10) G3(10) G2(10) G1(10) ];
FY =    [ G5(11) G4(11) G3(11) G2(11) G1(11) ];
Forces = [ Fx_p; Fy_p; Fx_f; Fy_f; FX; FY ];

%% Solve using LSR method
% Variable for unknowns, x
% x = [ x(1) x(2) x(3) ] = [ phi_0 alpha p ]
% Guesses for the different variables
X(1,:) = [ 0 0 2 ];        % Guess for Fx_p
X(2,:) = [ 0 0 2 ];        % Guess for Fy_p
X(3,:) = [ 0 0 2 ];        % Guess for Fx_f
X(4,:) = [ 0 0 2 ];        % Guess for Fy_f
X(5,:) = [ 0 0 2 ];        % Guess for FX
X(6,:) = [ 0 0 2 ];        % Guess for FY

% Solve all variables
for k = 1:6
    phi = Forces(k,:);      % Current variable to solve for
    x = X(k,:);

    format short e
    options = optimset('TolFun',1e-15,'TolX',1e-9,'MaxIter',
800,'MaxFunEvals', 1000);
    s = fsolve(@(x) S_LSR(x,phi,h),x, options );
    % Store for presentation
    S(k,:) = s;
```

```
    % Calculate uncertainty
    [Uphi(:,k), Us(k), dRE(:,k)] = U_phi(s, phi, h);
end

format short
'Percentual difference'
'Fx_p Fy_p Fx_f Fy_f FX FY'
Perc = (Uphi./Forces')

% Write and plot data for report presentation
dlmwrite('Output_phi.txt', Forces', 'delimiter', '\t','coffset', 1)
dlmwrite('Output_S.txt', S, 'delimiter', '\t','coffset', 1)
dlmwrite('Output_Us.txt', Us, 'delimiter', '\t','coffset', 1)
dlmwrite('Output_dRE.txt', dRE, 'delimiter', '\t','coffset', 1)
dlmwrite('Output_Uphi.txt', Uphi, 'delimiter', '\t','coffset', 1)
dlmwrite('Output_perc.txt', Perc, 'delimiter', '\t','coffset', 1)

%% Plot results
for i = 1:6
    subplot(2,3,i)
    plot(h(1), Forces(i,1),'bo'); hold on;
    plot(h(2), Forces(i,2),'bo'); hold on;
    plot(h(3), Forces(i,3),'bo'); hold on;
    plot(h(4), Forces(i,4),'bo'); hold on;
    plot(h(5), Forces(i,5),'bo'); hold on;

    H = linspace(0,3.5);
    y = S(i,1) + (S(i,2).*H.^S(i,3));
    plot(H,y,'k-')
    xlabel('h_i/h_1')
    ylabel('Force [kN]')
    if i == 1
        title('F_x_,_p')
    elseif i == 2
        title('F_y_,_p')
    elseif i == 3
        title('F_x_,_f')
    elseif i == 4
        title('F_y_,_f')
    elseif i == 5
        title('F_x Total')
    elseif i == 6
        title('F_y Total')
    end
end
```

Function files S_LSR.m and U_phi.m:

```
function [ S ] = S_LSR( x, phi, h )
% Equation to solve using Least Square Root method
% x = [ phi_0, alpha, p ]

p = phi;            % Parameter to solve
i = length(p);      % Number of grids
for j = 1:i
    s(j) = ( p(j) - x(1) - x(2)*(h(j))^(x(3)) )^2;
end
S = sqrt(sum(s));
end

function [ U_phi, Us, dRE  ] = U_phi( x, phi, h )
% U_PHI - The uncertainty of a solution

% Data for calculations
ng = length(phi);       % Number of grids
ph0 = x(1);             % From LSR solve
alph = x(2);            % - " -
p = x(3);               % - " -

% Calculate standard mean deviation of the fitting
for j = 1:ng
    s(j) = ( phi(j) - x(1) - x(2)*(h(j))^(x(3)) )^2;
end
Us = sqrt( sum(s) / (ng-3) );

% Calculate maximum difference between solutions, del_M
for i = 1:ng
    for j=1:ng
        D(i,j) = abs(phi(i)-phi(j));
    end
end
del_M = max(max(D));

% Calculate uncertainty, U_phi
for j = 1:ng
    H = h(j);       % h_i value for the current grid
    d_xRE = alph*H^2;
    d_RE = alph*H^p;
    dRE(j) = d_RE';

    if p >= 2.05
        U_phi(j) = max(1.25*d_xRE+Us, 1.25*del_M);
    elseif (p >= 0.95) && (p < 2.05)
        U_phi(j) = 1.25*d_RE;
    elseif (p > 0) && (p < 0.95)
        U_phi(j) = min(1.25*d_RE+Us, 1.25*del_M);
    elseif p < 0
        U_phi(j) = 3*del_M;
    elseif p == 0
        'Stop because p == 0'
        break
    end
end
end
```

N. Script for manipulating offset-files

Main script file:

```
clear all; clc; clf;

%% Manipulation of stern/skeg to change the inclination angle
% Input angle for new offset
dA = input('Angle difference from reference hull? (degrees): ');
'=== Calculating ==='

% Load reference hull offset
load Hull0705.mat

% Find first and Last X coord. in Stern/Skeg group
st_last = Stern(1,1);
st_first = Stern(length(Stern),1);
sk_first = Skeg(length(Skeg),1);
sk_last = Skeg(1,1);

%% From reference hull
EP = [ -3.60 0 3.60 ];      % x,y,z of lower transom end point (aft
point)
FP = [22.13 0 0 ];          % x,y,z of lower stern end point

% For calculation
r2d = 360/(2*pi);           % Radians to degrees
d2r = (2*pi)/360;           % Degrees to radians
k = 7/12;                   % Scaling from curvature

% Values for the reference hull
a = EP(3);                  % Z distance
B = FP(1)-EP(1);            % X distance
b = k*B;                    % Modified X, (to account for curvature)
ang = atan(a/b);            % Angle in radians
Ang = ang * r2d;            % Angle in degrees

% Values for new offset
NewAngle = (Ang + dA)       % New angle for stern
nang = NewAngle * d2r;
nB = (a/tan(nang))*(1/k);   % New X distance
ext = nB - B                % Stern extension/contraction from
reference

%% Calculate new offset
% Values to calculate new offset
dx = ext;                               % Difference in X distance
k = 1+(dx/(st_last+abs(st_first)));     % scaling factor
newFirst = k*st_first;                  % for calculating xMove
newLast = k*st_last;                    %       - " " -
% Move sections forward this value to keep same length
xMove = newFirst - st_first;

%% Update offsets
% X coords for Skeg:  Skeg(:,1)
% X coords for Stern: Stern(:,1)
Hull2 = Hull;
Stern2 = Stern;
Skeg2 = Skeg;
```

```
Stern2(:,1) = (Stern(:,1).*k) - xMove;
Skeg2(:,1) = (Skeg(:,1).*k) - xMove;

% Update Hull Section to match new length
nS = Stern2(1,1);               % New last station on Stern (x coord)
oH = Hull(length(Hull),1);      % Old first station on Hull (x coord)

while nS >= oH                  % If Hull section is to long..
    lH = length(Hull2);         % First x coord in Hull section
    Hull2(lH,:) = [];           % Remove row
    oH = Hull2(length(Hull2),1);% Update and redo
end

% Update Hull section with additional stations if stern is shorter
% than on the reference hull

%% Generate a Station from the hull
% Copies last station on Hull to stn
if ext < 0                      % Only do if its needed..
    j = length(Hull2);
    jj = 1;
    while Hull2(j-1,1) == Hull2(j,1)
         stn(jj,:) = Hull2(j,:);
         j = j - 1;
         jj = jj + 1;
     end
     stn(jj,:) = Hull2(j,:);    % Last point
     stn = flipud(stn);         % Flip rows
     stn(length(stn),4) = 0;    % not end of section
end

%% Add extra stations if needed
while ext < 0
    X = stn(1,1);        % x coord. where old hull ends
    x = X - 2;           % Spacing for new station is 2
    if x > nS
        stn(:,1) = x;
        Hull2 = [ Hull2; stn ];
    else
        break
    end
end

% Copy last station on "Stern" to first station on "Hull"
% First, add point on centerline
Spoint = length(Hull2)+1;
Hull2( Spoint,: ) = [ nS 0 0 1 ];

s = Stern2(1,1); t = 1;
while s == nS
    if Stern2(t,1) ~= nS
        break
    end
    Hull2( (length(Hull2)+1),: ) = Stern2(t,:);
    s = Stern2(t,1);
    t = t + 1;
end
% Set correct station starting point
Hull2( (Spoint+1),4 ) = 0;
```

```
% Set end station of group
for i = 1:length(Hull2)
    if Hull2(i,4) == 9;
        Hull2(i,4) == 0;
    end
end
AllHull = Hull2;
Hull2(length(Hull2),4) = 9;


%% Split Skeg for XPAN
[SkegSide, FlatSkeg ] = splitSkeg(Skeg2);

%% Additional group with Stern + Hull for RANS
AllHull = [ AllHull; Stern2 ];

%% Assemble and save new offsetfile
dlmwrite('h', Hull2, 'delimiter', '\t','coffset', 1)
dlmwrite('b', Bulb, 'delimiter', '\t','coffset', 1)
dlmwrite('st', Stern2, 'delimiter', '\t','coffset', 1)
dlmwrite('sk', Skeg2, 'delimiter', '\t','coffset', 1)
dlmwrite('sks', SkegSide, 'delimiter', '\t','coffset', 1)
dlmwrite('skf', FlatSkeg, 'delimiter', '\t','coffset', 1)
dlmwrite('ah', AllHull, 'delimiter', '\t','coffset', 1)

% 1 = Bulb, 2 = Hull, 3 = Stern, 4 = Skeg, 4b = FlatSkeg, 4c =
AllHull, 4d = FullSkeg

% !copy 1+b+2+h+3+st+4+sks+4b+skf+4d+sk+5 newoffsetfile.txt

Z = [ 0 0 0 ];
% Plot section
% Old Hull
subplot(2,1,1)
plotHull2( Bulb ); hold on
plotHull2( Skeg ); hold on
plotHull2( Stern ); hold on
plotHull2( Hull ); hold on
% New Hull
subplot(2,1,2)
plotHull2( Bulb ); hold on
plotHull2( Skeg2 ); hold on
plotHull2( Stern2 ); hold on
plotHull2( Hull2 ); hold on
axis([ -4 100 -20 20 -1 20])
axis equal

'=== Done! ==='
```

Function file splitSkeg.m:

```
function [Skeg, FlatSkeg ] = splitSkeg(OldSkeg)
%% Split skeg into 2 groups

OS = OldSkeg;       % Load old skeg
OS(:,4) = 0;        % Remove offset formatting

S1 = [] ;           % Vertical skeg offset
S2 = [] ;           % Planar skeg bottom offset
L = length(OS);     % Length of matrix
```

```
% 1 - Check Z-coord
% 2 - Move to respective vector
% 3 - Duplicate point for first in S1 and Last in S2
% 4 - Check station start point
% 5 - Set section end point

for i = 1:L
    Ns1 = (numel(S1)+4)/4;
    Ns2 = (numel(S2)+4)/4;
    if OS(i,3) == 0                     % Check if Z == 0
        S2(Ns2,:) = OS(i,:);            % ( Flat bottom of skeg )
        if OS(i,3) ~= OS(i+1,3)
            S1(Ns1,:) = OS(i,:);        % Duplicate edge points
        end

    elseif OS (i,3) > 0
        S1(Ns1,:) = OS(i,:);            % Else..
    else
        ANS = 'Something went wrong'
    end
end
% Fix last staion in S1 (aft line of skeg)
TMP = S1(length(S1),:);
S1(length(S1),:) = S2(length(S2),:);
S1(length(S1)+1,:) = TMP;

% Format S1
S1(1,4) = 1;            % Start of section
for i = 2:(length(S1)-1)
    x = S1(i,1);
    lx = S1(i-1,1);
    if x ~= lx
        S1(i,4) = 1;    % The point is a starting point
    else
    end
end
S1(length(S1),4) = 9;   % End of section

% Format S2 - Flat bottom of skeg
S2(1,4) = 1;            % Start of section
for i = 2:(length(S2)-1)
    x = S2(i,1);
    lx = S2(i-1,1);
    if x ~= lx
        S2(i,4) = 1;    % The point is a starting point
    else
    end
end
S2(length(S2),4) = 1;
S2(length(S2)+1,:) = [ S2(length(S2),1), 0, 0, 9 ];    % End of
section

Skeg = S1;
FlatSkeg = S2;
```

O. SHIPFLOW Free surface settings for loaded ship

Ship speed:	7 knots	8 knots	9 knots	10 knots	11 knots	12 knots
xups	-1	-1	-1	-1	-1	-1
xdown	1.75	1.8	1.85	1.9	1.95	2
y4side	1.049	1.074	1.104	1.136	1.173	1.212
stam	213	163	129	104	86	72
stau	149	114	90	73	60	51
stad	144	117	99	85	74	65
dlu	0.0047	0.0062	0.0078	0.0097	0.0117	0.0140
dfd	0.0047	0.0062	0.0078	0.0097	0.0117	0.0140
df1	0.0097	0.0104	0.0111	0.0117	0.0124	0.0131
point	70	70	70	70	70	70

P. Computational results for reference hull, loaded case

Computational results for reference hull						
Vs [kn]	**V [m/s]**	**Fn**	**Rn**	**CF**	**CPV**	**CV**
7	3.6	0.118	2.88E+08	1.82E-03	1.21E-03	3.03E-03
8	4.12	0.1349	3.29E+08	1.80E-03	1.22E-03	3.01E-03
9	4.63	0.1517	3.70E+08	1.77E-03	1.23E-03	2.99E-03
10	5.14	0.1686	4.11E+08	1.74E-03	1.23E-03	2.97E-03
11	5.66	0.1855	4.52E+08	1.73E-03	1.24E-03	2.97E-03
12	6.17	0.2023	4.93E+08	1.70E-03	1.24E-03	2.94E-03

Computational results for reference hull							
Vs [kn]	**CWTWC**	**CR**	**CT**	**RS [kN]**	**PE [kW]**	**K**	**S**
7	1.08E-05	1.22E-03	3.04E-03	47.07	169.47	0.69	0.3
8	2.49E-05	1.24E-03	3.04E-03	61.36	252.56	0.71	0.3
9	4.28E-05	1.27E-03	3.04E-03	77.56	359.04	0.72	0.3
10	1.36E-04	1.37E-03	3.11E-03	98.15	504.93	0.74	0.3
11	2.15E-04	1.46E-03	3.19E-03	121.83	689.56	0.76	0.3
12	3.03E-04	1.55E-03	3.24E-03	147.39	909.84	0.76	0.3

Q. Computational results for changed inclination angle

Computational results, inclination angle -4 degrees						
Vs [kn]	**V [m/s]**	**Fn**	**Rn**	**CF**	**CPV**	**CV**
7	3.6	0.118	2.88E+08	1.81E-03	1.39E-03	3.20E-03
8	4.12	0.1349	3.29E+08	1.79E-03	1.39E-03	3.18E-03
9	4.63	0.1517	3.70E+08	1.75E-03	1.40E-03	3.15E-03
10	5.14	0.1686	4.11E+08	1.73E-03	1.40E-03	3.13E-03
11	5.66	0.1855	4.52E+08	1.71E-03	1.40E-03	3.11E-03
12	6.17	0.2023	4.93E+08	1.68E-03	1.40E-03	3.08E-03

Computational results, inclination angle -4 degrees							
Vs [kn]	**CWTWC**	**CR**	**CT**	**RS [kN]**	**PE [kW]**	**K**	**S**
7	8.28E-06	1.40E-03	3.21E-03	49.59649	178.5761	0.78	0.294
8	1.40E-05	1.41E-03	3.19E-03	64.51118	265.5446	0.8	0.294
9	2.50E-05	1.42E-03	3.18E-03	81.17166	375.734	0.813	0.294
10	8.82E-05	1.49E-03	3.22E-03	101.5002	522.1735	0.824	0.294
11	1.41E-04	1.54E-03	3.25E-03	124.2438	703.2488	0.837	0.294
12	1.95E-04	1.59E-03	3.27E-03	148.6308	917.4772	0.837	0.294

Computational results, inclination angle -2 degrees						
Vs [kn]	**V [m/s]**	**Fn**	**Rn**	**CF**	**CPV**	**CV**
7	3.6	0.118	2.88E+08	1.82E-03	1.29E-03	3.11E-03
8	4.12	0.1349	3.29E+08	1.79E-03	1.29E-03	3.08E-03
9	4.63	0.1517	3.70E+08	1.76E-03	1.30E-03	3.06E-03
10	5.14	0.1686	4.11E+08	1.74E-03	1.31E-03	3.04E-03
11	5.66	0.1855	4.52E+08	1.72E-03	1.31E-03	3.04E-03
12	6.17	0.2023	4.93E+08	1.69E-03	1.31E-03	3.00E-03

Computational results, inclination angle -2 degrees							
Vs [kn]	**CWTWC**	**CR**	**CT**	**RS [kN]**	**PE [kW]**	**K**	**S**
7	9.23E-06	1.30E-03	3.12E-03	48.15813	173.3972	0.727	0.296
8	1.81E-05	1.31E-03	3.10E-03	62.67492	257.9861	0.746	0.296
9	3.23E-05	1.33E-03	3.10E-03	79.11049	366.1931	0.762	0.296
10	1.08E-04	1.41E-03	3.15E-03	99.41188	511.4302	0.774	0.296
11	1.69E-04	1.48E-03	3.20E-03	122.4171	692.9094	0.792	0.296
12	2.36E-04	1.55E-03	3.24E-03	147.1879	908.5701	0.794	0.296

Computational results, inclination angle +2 degrees						
Vs [kn]	**V [m/s]**	**Fn**	**Rn**	**CF**	**CPV**	**CV**
7	3.6	0.118	2.88E+08	1.83E-03	1.18E-03	3.01E-03
8	4.12	0.1349	3.29E+08	1.80E-03	1.19E-03	2.99E-03
9	4.63	0.1517	3.70E+08	1.77E-03	1.20E-03	2.97E-03
10	5.14	0.1686	4.11E+08	1.75E-03	1.21E-03	2.96E-03
11	5.66	0.1855	4.52E+08	1.74E-03	1.22E-03	2.96E-03
12	6.17	0.2023	4.93E+08	1.71E-03	1.22E-03	2.93E-03

Computational results, inclination angle +2 degrees							
Vs [kn]	**CWTWC**	**CR**	**CT**	**RS [kN]**	**PE [kW]**	**K**	**S**
7	1.39E-05	1.20E-03	3.03E-03	46.79246	168.48	0.676	0.299
8	3.42E-05	1.22E-03	3.02E-03	61.101	251.5074	0.694	0.299
9	5.62E-05	1.26E-03	3.03E-03	77.42176	358.3762	0.711	0.299
10	1.82E-04	1.39E-03	3.14E-03	99.01883	509.4081	0.724	0.299
11	2.80E-04	1.50E-03	3.24E-03	123.8395	700.9606	0.749	0.299
12	3.84E-04	1.61E-03	3.31E-03	150.4964	928.9928	0.749	0.299

Computational results, inclination angle +4 degrees						
Vs [kn]	**V [m/s]**	**Fn**	**Rn**	**CF**	**CPV**	**CV**
7	3.6	0.118	2.88E+08	1.83E-03	1.14E-03	2.98E-03
8	4.12	0.1349	3.29E+08	1.81E-03	1.15E-03	2.96E-03
9	4.63	0.1517	3.70E+08	1.78E-03	1.16E-03	2.94E-03
10	5.14	0.1686	4.11E+08	1.76E-03	1.17E-03	2.92E-03
11	5.66	0.1855	4.52E+08	1.75E-03	1.18E-03	2.93E-03
12	6.17	0.2023	4.93E+08	1.71E-03	1.18E-03	2.89E-03

Computational results, inclination angle +4 degrees							
Vs [kn]	**CWTWC**	**CR**	**CT**	**RS [kN]**	**PE [kW]**	**K**	**S**
7	1.93E-05	1.16E-03	2.99E-03	46.27271	166.6086	0.655	0.3
8	4.51E-05	1.19E-03	3.00E-03	60.65458	249.6698	0.674	0.3
9	7.31E-05	1.24E-03	3.02E-03	77.03472	356.5846	0.692	0.3
10	2.50E-04	1.42E-03	3.17E-03	100.1613	515.2857	0.706	0.3
11	3.66E-04	1.55E-03	3.29E-03	125.8428	712.2997	0.729	0.3
12	4.52E-04	1.63E-03	3.35E-03	152.0718	938.7176	0.729	0.3